

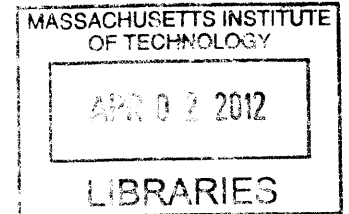
Thermoelectric Device Characterization and Solar Thermoelectric System Modeling

By

Andrew Muto

S.M., Mechanical Engineering (2008)
Massachusetts Institute of Technology

B.S., Mechanical Engineering (2005)
Northeastern University, Boston, MA



ARCHIVES

Submitted to the Department of Mechanical Engineering
in Partial Fulfillment of the Requirements for the Degree of
Doctor of Philosophy in Mechanical Engineering

at the
Massachusetts Institute of Technology
September 2011

© 2011 Massachusetts Institute of Technology, All rights reserved

Handwritten signature of Andrew Muto.

Signature of Author.....

Department of Mechanical Engineering
August 19, 2011

Handwritten signature of Gang Chen.

Certified by.....

.....
Gang Chen
Carl Richard Soderberg Professor of Power Engineering
Thesis Supervisor

Handwritten signature of Gang Chen.

Accepted by.....

.....
David E. Hardt
Chairman, Department Committee on Graduate Students

Handwritten signature of David E. Hardt.

Thermoelectric Device Characterization and Solar Thermoelectric System Modeling

by

Andrew Muto

Submitted to the Department of Mechanical Engineering on August 19, 2011
in Partial Fulfillment of the Requirements for the Degree of
Doctor of Philosophy in Mechanical Engineering

Abstract

Recent years have witnessed a trend of rising electricity costs and an emphasis on energy efficiency. Thermoelectric (TE) devices can be used either as heat pumps for localized environmental control or heat engines to convert heat into electricity. Thermoelectrics are appealing because they have no moving parts, are highly reliable, have high power densities, and are scalable in size. They can be used to improve the overall efficiency of many systems including vehicle waste heat, solar thermal, HVAC, industrial waste heat, and remote power for sensor applications. For thermoelectric generators to be successful, research progress at the device level must be made to validate materials and to guide system design. The focus of this thesis is thermoelectric device testing and system modeling. A novel device testing method is developed between room temperature range and 230°C. The experimental technique is capable of directly measuring an energy balance over a single leg, with a large temperature of 2-160°C. The technique measures all three TE properties of a single leg, in the same direction, with significantly less uncertainty than other methods. The measurements include the effects of temperature dependent properties, side wall radiation loss, and contact resistance. The power and efficiency were directly measured and are within 0.4 % and 2 % of the values calculated from the property measurements.

The device property measurement was extended to higher temperatures up to 600°C. The experimental system uses an inline uncouple orientation to minimize radiation losses and thermal stress. Two major experimental challenges were the construction of a high temperature calibrated heater and a thermocouple attachment technique. We investigated skutterudite materials which are of interest to many research groups due to their high thermoelectric figure-of-merit (ZT), and good thermomechanical properties. Unlike room temperature Bi₂Te₃ devices, skutterudite module construction techniques are not well established and were a major challenge in this work. Skutterudite device samples were fabricated by a direct bonding method in which a rigid electrode is sintered directly to the TE powder during press. Compatible electrode materials were identified and evaluated based on thermal stress, parasitic electrical/thermal resistance, chemical stability and ease of prototype fabrication. The final electrodes solutions were Co₂Si with the P-type and CoSi₂ with the N-type. The direct hot press process was modified into what we call a hybrid hot press to produce device samples with strong bonds and no cracks. Preliminary accelerated aging tests were conducted to evaluate the long term chemical stability of the TE-electrode contacts. We demonstrated $Z\bar{T}_{eff} = 0.74$ for the N-type between 52°C and 595°C corresponding to 11.7% conversion efficiency and $Z\bar{T}_{eff} = 0.51$ for the P-type between 77°C and 600°C corresponding to 8.5% efficiency. The maximum efficiency of the NP uncouple was measured to be 9.1% at ~550°C. The effective ZT and efficiency

measurement includes electrical contact resistance, and parasitic thermal/electrical resistance in the electrodes, and heat losses at the sides of the legs. Thus we have included all the parasitic loss effects that are present in a real unicouple. The efficiency values measured in this work are among the highest recorded for a skutterudite unicouple. The TE-electrode combinations meet all the criteria for device testing and offer a practical, manufacturable solution for module construction.

Solar thermal power generation is fast becoming cost competitive for utility scale electricity with 380 MW electric currently installed. Parabolic trough concentrators have proven economical and reliable but their efficiency is limited by the maximum temperature of the heated fluid. We explored the idea of a solar thermoelectric topping cycle (STET) in which a thermoelectric generator (TEG) is added at high temperature to increase the overall efficiency of the solar Rankine cycle. In this design the perimeter of the receiver tube is covered with thermoelectrics so that the absorber temperature is raised and the energy rejected from the TEG is used to heat the fluid at its originally specified temperature. A heat transfer analysis was carried out to determine the overall system efficiency. A parametric study was performed to identify design constraints and put bounds on the total system efficiency. The system performance was simulated for all conceivable concentrations and fluid temperatures of a solar thermal trough. As the absorber temperature increases more power is generated by the TEG but is offset by a rapidly decreasing absorber efficiency which results in only a marginal increase in net power. It was concluded that for the proposed STET to increase the system efficiency of a state of the art trough system by 10% requires a $Z\bar{T}_{eff}=3$ TEG, which is well beyond the state-of-the-art thermoelectric materials.

Thesis Supervisor: Gang Chen

Title: Carl Richard Soderberg Professor of Power Engineering

Acknowledgments

The last six years at MIT have been more rewarding to me than I can express in one page. Excellence of science and engineering at MIT is maintained by a unique culture that was a privilege to be a part of. My success in graduate school was facilitated by the guidance from, discussions with, and friendship of many talented people. I want to thank my advisor Prof. Gang Chen for his commitment as a scientist and mentor. He lead our group to the highest standard in quality. I've learned so much from both our successes and failures together. Prof. Zhifeng Ren, and his group at BC have always worked closely with our group at MIT in a successful long term collaboration. I have benefited greatly by his guidance and intuition through the years. I've worked closely with Prof. Evelyn Wang on several projects since her appointment as an MIT faculty member in 2007. I'm thankful for her valuable critiques and encouragement. I thank Prof. John Lienhard IV for his sharp critical eye, and talents as a lecturer in the thermal sciences.

Prof. Gang Chen has cultivated an atmosphere in the NanoEngineering group that promotes free thought and collaboration. It was an honor to slave beside the following talented researchers who have contributed directly to my thesis: Jian Yang, Qing Hao, Dan Kraemer, Ken McEnaney. I have had so many technical and metaphysical discussions with students/post-docs/visiting scholars that have shaped who I am and how I think. Truly the best way to learn is via discussion with peers. In addition to the names previously mentioned I want to thank the following people for their passion for science, inquisitive minds, and friendship: Xiaoyuan Chen, Vince Berube, Anurag Bajpayee, Austin Minnich, Jivtesh Garg, Greg Radtke, Tom Harris, Sheng Shen, Mike Kozlowski, Hohyun Lee, Asegun Henry, Lu Hu, Vincent Berube, Aaron Schmidt, Arvind Narayanaswamy, Erik Skow, Chris Dames, Matthew Branham, Kimberlee Collins, Daniel Kraemer, Sangyeop Lee, Maria Luckyanova, Pietro Lebdo Sambegoro, Jonathan Tong, James Wang, Yi Ma, Bo Yu, Andre Lenert, Shuo Chen, Tony Feng, Sang Eon Han, Stephan Kress, Tengfei Luo, Anastassios Mavrokefalos, Nitin Shukla, Bhaskaran Muralidharan, Jae Sik Jin, Christine Junior, Jinwei Gao, Matteo Chiesa, Shinichiro Nakamura, Daryoosh Vashae. Finally I thank my wife for her loving support and unending patience and encouragement as I pursued my dreams.

Table of Contents

Abstract	3
Acknowledgments	5
Table of Contents	7
List of Figures	11
List of Tables	20
Chapter 1. Introduction	21
1.1.1 Thermoelectric Phenomena.....	21
1.1.2 Seebeck Coefficient	22
1.1.3 Thermodynamics and Peltier Heat	23
1.2. <i>Governing Equation of Thermoelectricity</i>	25
1.3. <i>Power Conversion and ZT</i>	28
1.4. <i>Semiconductors as Thermoelectrics</i>	31
1.5. <i>State of the Art and Device Design</i>	32
1.6. <i>Nanocomposite Method</i>	37
1.7. <i>Individual Property Measurements</i>	39
1.8. <i>Device Measurements</i>	41
1.9. <i>Scope and Organization of this Thesis</i>	42
Chapter 2. Device Properties and Efficiency Measurement Method	44
2.1. <i>Introduction</i>	44
2.2. <i>Mathematical Formulation</i>	45
2.2.1 Governing Equation	45
2.2.2 Device Properties Measurement under Large ΔT	47
2.2.3 Efficiency	48
2.2.4 Effective ZT.....	50
2.3. <i>Experimental System</i>	50
2.4. <i>Property Data Analysis</i>	53

2.5. Property Results	54
2.6. Efficiency Results	55
2.7. Conclusions	57
Chapter 3. Skutterudite Unicouple Fabrication	58
3.1.1 Individual Property Measurement Results	58
3.1.2 Compatible Electrode Materials	60
3.2. Electrode Selection	62
3.2.1 Chemical Properties and Synthesis	63
3.2.2 Thermomechanical Properties	65
3.2.3 Transport Properties	68
3.3. Device Sample Fabrication	70
3.3.1 Original Pressing Conditions	70
3.3.2 DHP Device Samples	73
3.3.3 Direct Hot Press vs. Hybrid Hot Press	75
3.3.4 HHP Device Samples	84
3.3.5 Conclusions	89
Chapter 4. Skutterudite Unicouple Testing	90
4.1. Calibration	92
4.2. Heater Assembly Fabrication	94
4.3. Single Pair Fabrication	97
4.4. Data Analysis	99
4.5. Device Measurement Results	102
4.5.1 N-N results	104
4.5.2 P-P results	106
4.5.3 NP Efficiency	107
4.6. Accelerated Aging Tests	109
4.7. Conclusions	115
Chapter 5. Solar Thermoelectric System Modeling	117
5.1. Introduction	117
5.1.1 Solar Flux and Receiver Geometry	119

<i>5.2. 1-D Heat Transfer Model</i>	122
<i>5.3. Selective Absorbing Surface</i>	126
<i>5.4. Thermal Losses</i>	130
<i>5.5. Transition Wavelength and Solar Spectrum AM 1.5 direct</i>	132
<i>5.6. Results and Discussion</i>	134
<i>5.7. Conclusions</i>	136
Chapter 6. Summary and Recommendations for Future Work	138
Appendix	142
Bibliography	152

List of Figures

Figure 1-1 Thermoelectric effects in a material. a) Seebeck effect: a temperature difference induces a voltage through the material b) Peltier effect: a current flow induces heat flow through the material. 22

Figure 1-2: The Seebeck effect is when an electric field arises due to the diffusion of charge carriers under a temperature difference. 23

Figure 1-3: Peltier heat flow in a segmented material at uniform temperature. Heat transfer is localized at the interface where the Seebeck coefficient changes..... 25

Figure 1-4: Energy balance in a differential element of a thermoelectric material. From left to right: Peltier heat, Fourier heat conduction, electrical power 26

Figure 1-5: Thermoelectric energy balance, constant properties. 28

Figure 1-6: Thermoelectric properties S, σ, k (Seebeck coefficient, electrical conductivity, thermal conductivity) as a function of carrier concentration. Semiconductors make the best thermoelectric materials. 32

Figure 1-7 Schematic of thermoelectric devices, (left) power generator (right) and thermoelectric cooler..... 32

Figure 1-8: TE devices a) TE cooler in a car seat b) TE generator used in NASA space missions..... 34

Figure 1-9: (left)Second law efficiency (total efficiency divided by Carnot efficiency) vs. ZT for $T_H=500$ K and $T_C=300$ K. (right) Conversion efficiency of thermoelectric generator operating from room temperature on the cold side up to 1300K. Existing heat engine cycles achieve higher efficiency than state of the art thermoelectrics.¹² 35

Figure 1-10: Timeline of ZT over the past 60 years.¹The materials above $ZT=2$ are thin films, which are inherently difficult to measure and have been contested. 36

Figure 1-11: ZT vs. temperature for different material systems¹..... 36

Figure 1-12: Stainless steel jars and the Ball mill machine (Spex 8000M)..... 38

Figure 1-13: Pictures of hot press. (top left).Schematic drawing of the hot press (right). Homemade hot press system at Boston College (bottom left). 0.5 inch and 1 inch consolidated samples.¹⁷ 39

Figure 1-14: (left) Laser flash system to measure the thermal conductivity. (middle) ZEM-3 system to measure the electrical conductivity and Seebeck coefficient. (right) Sample mounting system of the ZEM-3.....	40
Figure 2-1: Illustration of a p-type thermoelectric leg under working conditions.....	46
Figure 2-2: A schematic diagram of the a) property and efficiency measurement system b) calibration procedure for the hot side heater and the cold side heat flux sensor.....	52
Figure 2-3: Photograph the experimental system with a TE leg under test.....	52
Figure 2-4: Cold side temperature vs. hot side temperature during the device properties measurement.....	53
Figure 2-5: The four intrinsic TE properties versus temperature and their respective effective properties versus hot side temperature: a) Seebeck coefficient, b) thermal conductivity, c) electrical resistivity, d) dimensionless thermoelectric figure of merit.....	55
Figure 2-6: Maximum efficiency versus temperature difference across the leg for a cold side temperature of 24.5 °C.....	56
Figure 2-7: Efficiency and power versus current, the points with error bars are the measured values, the lines are calculated from the measured properties using Eq.(2.9) and Eq.(2.10). a) Hot side temperature is 86–93 °C, cold side is 24–25 °C. b) Hot side temperature is 169–172 °C.....	57
Figure 3-1: N-type properties measured by Jian Yang using the individual properties method described in chapter 1 (N-melt 2).....	59
Figure 3-2: P-type properties measured by Jian Yang using the individual properties method described in chapter 1 (P-melt 12)	59
Figure 3-3: Traditional module design, electrodes are either soldered to the thermoelectric legs or bonded directly.	60
Figure 3-4: (left) N-type leg with Ni plating before test (right) N-type after wetting with Sn-Sb solder and left on a hot plate in air at 450°C of 10hrs. Catastrophic diffusion damage resulted.	61
Figure 3-5: Direction bond method (left) includes rigid electrodes with thermoelectric powder during sintering phase. The result (right) is a robust bond with superior mechanical, electrical, and thermal properties.	62
Figure 3-6: Co-Si phase diagram (source: ASM International 2009, Diagram No.101097)	64

Figure 3-7: Sb-Si phase diagram (source: ASM International 2009, Diagram No.902064)..... 64

Figure 3-8: Fe-Si phase diagram (source: ASM International 2009, Diagram No.2002013).... 64

Figure 3-9: Coefficient of thermal expansion for N and P ball-mill (BM) samples, and literature values of candidate electrode materials.⁶⁰ These results were the basis of our decision to try CoSi_2 and Co_2Si as electrodes. BM samples were measured by collaborators at Bosch..... 66

Figure 3-10: Coefficient of thermal expansion for N and P ball-mill (BM) samples compared to the N and P melt samples. The hysteresis of the melt samples is probably due to incomplete sintering and/or lack of annealing. BM samples were measured by collaborators at Bosch. Melt samples were measured by Netzsch testing service. 66

Figure 3-11: Coefficient of thermal expansion of our measured electrodes (measured by Netzsch) compared to literature values.⁶⁰ The disagreement between the measured and literature warrants further investigation..... 67

Figure 3-12: Measured Coefficient of thermal expansion of the final electrodes and skutterudites used in device testing. (measured by Netzsch) 68

Figure 3-13: Seebeck coefficient of annealed electrode materials. (left) CoSi_2 used with the N-type (right) Co_2Si used with the P-type. (measured by Jian Yang) 69

Figure 3-14: Electrical Resistivity of annealed electrode materials. (left) CoSi_2 used with the N-type (right) Co_2Si used with the P-type. (measured by Jian Yang) 69

Figure 3-15: Thermal conductivity of annealed electrode materials. (left) CoSi_2 used with the N-type (right) Co_2Si used with the P-type. (measured by Jian Yang) 70

Figure 3-16: Co-Sb phase diagram used to guide the synthesis of CoSb .¹⁷ 71

Figure 3-17: Pressure/temperature versus time for the original direct hot press (DHP) process for producing N and P skutterudites..... 72

Figure 3-18: N-type skutterudite individual properties measured by Jian Yang.¹⁷ (upper left) Power factor at three different press temperatures (upper right) thermal conductivity at three different press temperatures (lower left) ZT at three different press temperatures (lower right) ZT from a 1-step and 2-step method with or without annealing. Optimizing the press conditions can enhance ZT on the order of 15%..... 72

Figure 3-19: Evolution of the P-type device sample. The pressing conditions were changed to produce progressively fewer cracks in the sample. 74

Figure 3-20: Direct hot press (DHP) pressing conditions for the P-type device samples..... 74

Figure 3-21: (left) Plungers were insulated with boron nitride in order to eliminate joule heating within the sample during press (middle) resulting N-type with no visible cracks. (right) N-type broke along the mid-plane after subsequent polishing. 75

Figure 3-22: (left) direct hot press die (right) the new hybrid hot press die. 75

Figure 3-23: Geometry and mesh used in the finite element model. Note the position of the thermocouples measuring T_{die} and $T_{plunger}$ 76

Figure 3-24: Total power dissipation density (left) 2D field (right) 2D field projected in the Z direction. The majority of the Joule heating occurred at the narrow section of the plungers near the contacts. 78

Figure 3-25: Model verification test. Experimentally measured $T_{plunger}$, T_{die} versus time for a N-type, 2 mm thick sample. The maximum temperature difference between $T_{plunger}$ and T_{die} occurs at steady state..... 79

Figure 3-26: Calculated temperature along the plunger/sample axis (blue) and the plunger/sample perimeter (green) for the N-type, 2 mm thick verification sample. The TE sample extends from 0-2 mm on along the x-direction. Red point denotes $T_{plunger}$, blue point denotes T_{die} . The dip in the green curve is a results of heat conducting from the samples to the die..... 80

Figure 3-27: Temperature field of the direct hot press (DHP), device sample, with $h_{sample}=10\text{mm}$. (top left) 2D temperature field (top right) 2D temperature field projected in z-direction (bottom) temperature along the plunger/sample axis (blue) and the plunger/sample perimeter (green). Red point denotes $T_{plunger}$, blue point denotes T_{die} . Notice the large temperature gradients within the sample and the discontinuity at the plunger-die interface. 81

Figure 3-28: Temperature field of the hybrid hot press (HHP), device sample, with $h_{sample}=10\text{mm}$. (top left) 2D temperature field (top right) 2D temperature field projected in z-direction (bottom) temperature along the plunger/sample axis (blue) and the plunger/sample perimeter (green). Red point denotes $T_{plunger}$,

blue point denotes T_{die} . The sample temperature is very uniform and close to T_{die} .	83
Figure 3-29: Hybrid hot press (HHP) device sample pressing conditions. (top) N-type (bottom) P-type.	85
Figure 3-30: Resistance versus length of P-type device sample. The electrical contact resistance, contact region length, TE bulk resistivity and electrode bulk resistivity are given.	86
Figure 3-31: Resistance versus length of N-type device sample. The electrical contact resistance, contact region length, TE bulk resistivity and electrode bulk resistivity are given.	87
Figure 3-32 Device samples. (left) N-type after press (middle) P-type after press (right) P-type after final polish and cutting two produce four device samples.	87
Figure 3-33: Brazed electrodes. $CoSi_2$ brazed to Co_2Si using 56Ag22Cu17Zn5Sn. The contact resistance was measured to be very low.	88
Figure 4-1: (left) Bi_2Te_3 test assembly from chapter two, capable of temperatures up to 235°C (right) skutterudite test assembly capable of temperatures up to 650°C.	90
Figure 4-2: Schematic of the inline device measurement system.	91
Figure 4-3: Test assembly mounted on the cold finger of a cryostat. Created by Qing Hao, modified by Andy Muto.	91
Figure 4-4: (left) Schematic of the isothermal block used in the thermocouple calibration and Seebeck calibration experiments. (right) Thermocouple calibration comparison. The measured temperature difference is relative to the Pt RTD measuring absolute temperature. The results prove that the thermocouple attachment method is valid at high temperatures and for long duration.	93
Figure 4-5: Pt wire Seebeck calibration. The wires Pt1 and Pt2 were measured by two different thermocouple pairs. The measured Seebeck of Pt is in excellent agreement with literature. ^{66,67}	94
Figure 4-6 Calibrated heater using two RTDs backfilled with braze. (left) Before Cu cover plate was attached. (right) After cover plate was attached.	95
Figure 4-7: Heater calibration with measured and calculated values from Eq.(3.1).	96

Figure 4-8: (left) Calculated heater loss from the connecting wires. (right) Proportion of the calculated wire heat loss to the total power dissipated at the heater..... 97

Figure 4-9: Thermocouple attachment method. (left) Bare thermocouple wires were positioned on the electrode, ~0.35 mm from the interface (right) and attached with Ag epoxy and subsequently cured at 120°C for 8 hrs..... 98

Figure 4-10: Ni foil (12.5 μm) was inserted in between the electrodes and heater assembly to function as a diffusion barrier..... 98

Figure 4-11: N-N device sample loaded into testing assembly, prior to connecting thermocouple wires and heater electrodes..... 98

Figure 4-12: N-N device sample loaded and ready for test..... 99

Figure 4-13: Schematic of heater assembly and electrode losses used to solve for Q_{hot} entering the legs..... 100

Figure 4-14: Reflectance versus wavenumber of the skutterudite wall and electrodes. This is the raw data taken from an FTIR (Fourier transform infrared spectroscopy) which was used to calculate the emissivity of each surface..... 100

Figure 4-15: (left) Magnitude of the loss correction relative to the total dissipated power IV_{heater} (right) upper and lower uncertainty limits of the cumulative Q_{loss} corrections. Results are from the N-N test..... 101

Figure 4-16: Magnitude of the cumulative Q_{loss} correction relative to the total dissipated heat IV_{heater} . (left) N-N test (right) P-P test..... 102

Figure 4-17: Total upper and lower bound uncertainty in Q_{Hot} for (left) N-N and (right) P-P test, units are in W..... 102

Figure 4-18: Effective properties of N-type device samples. The "calc." values include the full thermoelectric properties (individual property measurements), surface emissivity and geometry of both the skutterudite and electrodes between the measured temperatures. The "ideal" values are calculated from the individually measured properties of the skutterudite only and measured temperatures assuming there are no electrodes and no sidewall radiation..... 105

Figure 4-19: ZT_{eff} and corresponding maximum efficiency of the N-type device samples.... 105

Figure 4-20: Effective properties P-type device samples. The "calc." values include the full thermoelectric properties (individual property measurements), surface emissivity and geometry of both the skutterudite and electrodes between the

measured temperatures. The "ideal" values are calculated from the individually measured properties of the skutterudite only and measured temperatures assuming there are no electrodes and no sidewall radiation..... 106

Figure 4-21: ZT_{eff} and corresponding maximum efficiency of the P-type device samples..... 107

Figure 4-22: Thermoelectric power versus current for N-P couple. (left) The hot side temperature of the N and P legs were at 302-306°C and 295-298°C, respectively, and the cold side was at 39-43°C and 48-54°C. (right) The hot side temperature of the N and P legs were at 558-559°C and 544-546°C, respectively, and the cold side was at 58-63°C and 76-83°C..... 108

Figure 4-23: Efficiency versus current for NP couple. (left) The hot side temperature of the N and P legs were at 302-306°C and 295-298°C, respectively, and the cold side was at 39-43°C and 48-54°C. (right) The hot side temperature of the N and P legs were at 558-559°C and 544-546°C, respectively, and the cold side was at 58-63°C and 76-83°C. The "meas." and "calc." values are the final values after the heater section has been excluded thermally and electrically. The green triangles are the measured result if the heater assembly is not excluded thermally which is 12.5% lower. The purple stars are for the case that the heater assembly is not excluded thermally or electrically..... 109

Figure 4-24: Results from accelerated aging studies in literature on a skutterudite-electrode system. ⁴⁶ (left) SEM micrographs of IMC layer growth (right) Modeled as a diffusion process by an Arrhenius equation..... 111

Figure 4-25: SEM micrograph of CoSb₃/Ti/Mo-Cu joint at 600°C for 4 days. This was done by Zhao.⁴⁶ 111

Figure 4-26: N-CoSi₂ before and after accelerated aging. (top left) High magnification as-pressed. (top right) Aged at 605°C for 190 hrs. (bottom left) Low magnification as-pressed. (bottom right) Low magnification aged at 605°C for 190 hrs. Dark spaces are void, light spaces are chip/particles at the surface..... 113

Figure 4-27: Co₂Si-P before and long duration high temperature exposure 114

Figure 4-28: P-type electrical resistance versus length (blue line) as-pressed (red line) after accelerated aging at 605°C for 5 days..... 114

Figure 4-29: Photograph of an N-type device sample held at 605°C for 2 days in partial vacuum (10^{-1} Torr). The surface of the skutterudite is discolored and flaking off, and the left contact has completely detached.	115
Figure 5-1: (left) Cartoon of a solar parabolic trough collector array. (middle) Photograph of a receiver tube. (right) Schematic, cross sectional view of the proposed receiver tube of the solar thermoelectric topping cycle. ⁶⁹	118
Figure 5-2: Solar spectrums. The AM 1.5 direct spectrum (red) should be used for any solar thermal system with tracking and was used for all calculations in this chapter..	120
Figure 5-3: Concentrated solar flux distribution along a state of the art receiver tube. (right) Experimental results showing non uniform flux distribution and reflections at the glass. ⁷⁴ (left) Calculated flux distribution from ray tracing using real geometry of the collector. ⁷⁴	121
Figure 5-4: (left) Glass transmittance. (right) Selective absorber properties. ⁷⁵	122
Figure 5-5: Schematic of a solar thermal power plant with operating temperature range of the fluid. ⁶⁹	122
Figure 5-6: (left) A schematic of the STET receiver with thermoelectric elements lining the bottom perimeter where the highest intensity concentrated radiation is located. (right) A one-dimensional steady state model of the work and heat transfers of the STET. All thermal resistances are lumped into $Z\bar{T}_{eff}$	124
Figure 5-7: Thermoelectric topping cycle performance of a $ZT_{eff}=1$ material, neglecting all thermal losses from the receiver. (left) Efficiency gain vs. fluid temperature, and absorber temperature. (right) Heat engine ratio vs. fluid temperature and absorber temperature. Contour increments are 0.05.	126
Figure 5-8: Solar spectrum at 40x concentration (blue). Schematic representation of the selective surface properties (red) and glass tube properties (grey).	128
Figure 5-9: Integrated solar intensity versus wavelength, $s_1(\lambda)$ in blue, $s_2(\lambda)$ in green.	130
Figure 5-10: 1-D Radiative heat transfer network of the receiver, used to calculate the thermal loss. The thermal emission spectra is split into two regimes. The resistance in yellow is a convection resistance.	131
Figure 5-11: Transition wavelength versus absorber temperature and concentration. (left) A broad view of solar thermal operating space with absorber temperatures	

ranging from 50-1000°C and concentrations from 1-1000. (right) The operating concentrations and temperatures of a conceivable line concentrator. For all practical solar thermal trough operating conditions the solution converges to two transition wavelengths: 1800nm and 2500nm. 133

Figure 5-12: (left) Receiver heat flux loss at optimal transition wavelength (right) Maximum absorber efficiency. 134

Figure 5-13: Glass temperature versus absorber temperature. 134

Figure 5-14: Simulation results plotted as a function of concentration and fluid temperature the black box represents the current state of the art solar troughs a) power ratio, $ZT_{eff} = 1$ b) power ratio, $ZT_{eff} = 3$ c) efficiency gain, $ZT_{eff} = 3$ d) optimal absorber temperature, $ZT_{eff} = 3$ 136

Figure 6-1: Roadmap from skutterudite material characterization to electrode selection device testing and module testing. The bullets highlights in yellow have been accomplished in this thesis while the others are future work that should be performed in the future. 140

List of Tables

Table 3-1: Mechanical properties of skutterudites, the last column is from ⁵⁸	68
Table 3-2: Geometric parameters and current setting of the direct hot press (DHP) and hybrid hot press (HHP) model.....	77
Table 3-3: Electrical (ρ) and thermal (κ) contact resistances. Subscripts represent a graphite-graphite or graphite-TE contact, in the radial or axial direction. L_{graphite} is the equivalent length of graphite using nominal values of $\rho = 10^{-5} \Omega\text{m}$, and $\kappa = 100 \text{ W/mK}$. Zhang is from [62] and Muto is from this work.....	77
Table 4: Geometry of device samples used in device testing. The uncertainty in A/L_{TE} is 6.2%.....	88
Table 5: Surface emissivity nominal values and upper and lower bounds. The N and P-type emissivity do not have upper and lower bounds because these values were only used in the model results.	101
Table 6: Maximum uncertainty in effective property measurements	103

Chapter 1. Introduction

The field of thermoelectricity studies the direct coupling of electricity and heat within a solid-state material. Thermoelectric (TE) devices operate as heat engines or heat pumps and are appealing because they have no moving parts, require no maintenance, are highly reliable, have high power densities, and are scalable in size.¹ However, their efficiency needs to be improved if they are to be broadly implemented beyond a few niche markets, and be competitive with other energy conversion technologies on a large scale.¹ It's been evident in recent years that nanostructured thermoelectric materials offer the greatest potential for increasing conversion efficiency.² Thermoelectric properties are dominated by the transport characteristics of electrons and phonons which have mean free paths ranging from nanometers to microns. Nanostructures on this length scale or smaller can strongly affect electron and phonon transport and enhance thermoelectric properties if designed properly.³

This chapter introduces the Seebeck effect and Peltier effect, and the fundamental equations of thermoelectricity, and provides an overview of the state-of-the-art in the field. We will explain thermoelectric nanocomposites and how they are synthesized. Traditionally the three thermoelectric properties are measured independently of each other as a function of temperature. Thermoelectric characterization techniques will be explained, from which the urgent need for device measurements will become apparent.

1.1.1 Thermoelectric Phenomena

When a material is subjected to a temperature difference, an electrical potential difference is produced (figure 1-1); conversely, when electrical current flows through a material, entropy and heat are also transported. These phenomena are called thermoelectric effects, the former is the *Seebeck effect* and the latter is the *Peltier effect*, named after the scientists who first observed these phenomena.⁴ Figure 1-1 shows the thermoelectric effects in a single material. The fundamental physical reason for thermoelectric phenomena is that charge carriers such as electrons and holes are also entropy and heat carriers. Heat transfer and current flow are thus coupled phenomena, and will be briefly explained in the following two sections.

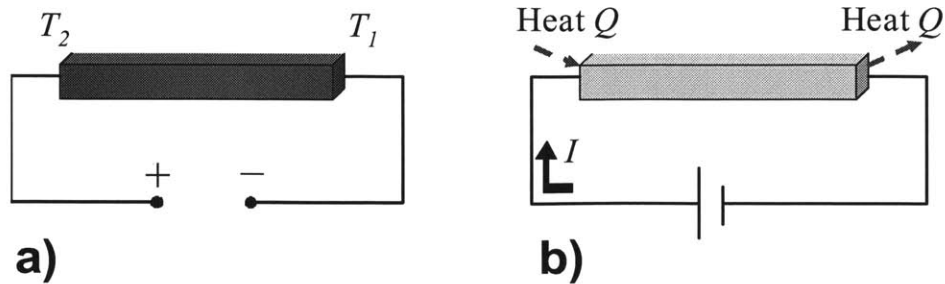


Figure 1-1 Thermoelectric effects in a material. a) Seebeck effect: a temperature difference induces a voltage through the material b) Peltier effect: a current flow induces heat flow through the material.

1.1.2 Seebeck Coefficient

The Seebeck effect has been used in thermocouples to measure temperature for a long time. Conventional thermocouples are made of metals or metal alloys. They generate small voltages that are proportional to an imposed temperature difference. This is the same Seebeck effect which is used in thermoelectric power conversion.

When the electrical current in a material is zero and a temperature gradient is present, an electrochemical potential difference ΔV , proportional to the temperature difference will develop. The proportionality constant between the temperature gradient and the generated electric potential is called the Seebeck coefficient,

$$S \equiv -\frac{dV}{dT}. \quad (1.1)$$

In principle the thermoelectric effect is present in every material but semiconductor materials are currently the best thermoelectrics. In simplest terms, the Seebeck arises from the diffusion of charge carriers from the hot side to the cold side (figure 1-2). Hot carriers have more kinetic energy, greater velocity, and thus diffuse faster than move faster than cold carriers. Thus when a temperature gradient is present, charge carriers accumulate on the cold side creating a Seebeck voltage.

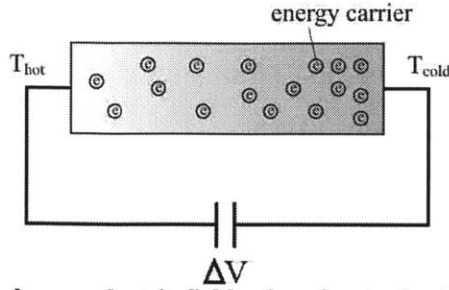


Figure 1-2: The Seebeck effect is when an electric field arises due to the diffusion of charge carriers under a temperature difference.

1.1.3 Thermodynamics and Peltier Heat

Thermodynamically, there is a direct coupling between heat transfer and electric current. The current density J , and heat flux q , are inherently coupled phenomena and are linearly proportional to two intrinsic property gradients: the electrochemical potential and temperature by⁵

$$\vec{J} = L_{11}(-\nabla V) + L_{12}(-\nabla T), \quad (1.2)$$

$$\vec{q} = L_{21}(-\nabla V) + L_{22}(-\nabla T). \quad (1.3)$$

The coefficients are calculated based on transport theories, such as the Boltzmann equation. The cross term coefficients L_{12} and L_{21} are related by Onsager's reciprocity theorem: $\frac{L_{21}}{L_{12}} = T$.⁶

Observe that when the temperature is uniform Eq.(1.2) becomes the familiar Ohm's law and we find that L_{11} is equal to the electrical conductivity σ . By setting the current density to zero it is found that the Seebeck coefficient is equal to the ratio of L_{12} to L_{11} ,

$$S = \frac{L_{12}}{L_{11}}. \quad (1.4)$$

We can now rearrange the charge transport equation to get a useful equation for the electrochemical potential in which the first term is generated by an Ohmic voltage drop and the second term is generated by the Seebeck effect,

$$dV = -\frac{J}{\sigma} dx - SdT \quad (1.5)$$

Eliminating ∇V from Eq.(1.2) and (1.3) we arrive at the constitutive relation for heat flux in its final form

$$\bar{q} = \frac{L_{21}}{L_{12}} S \bar{J} - \left(L_{22} - \frac{L_{21}L_{12}}{L_{11}} \right) \nabla T = \Pi \bar{J} - k \nabla T, \quad (1.6)$$

where $\Pi \equiv TS = \frac{L_{21}S}{L_{12}}$ is the Peltier coefficient and k is the thermal conductivity. The first term in Eq.(1.6) is the Peltier heat (below) which is reversible with the direction of the current. This is what allows for thermoelectric heat pumping because the heat is transferred in the direction of the current, independent of the temperature gradient.

$$\bar{q}_{Peltier} = \Pi \bar{J} \quad (1.7)$$

Heat is absorbed or released at the interface of two dissimilar materials by the Peltier Effect, figure 1-3. When current is conducted across two dissimilar materials, a heat transfer will take place at the boundary due to the different Peltier coefficients of each material.

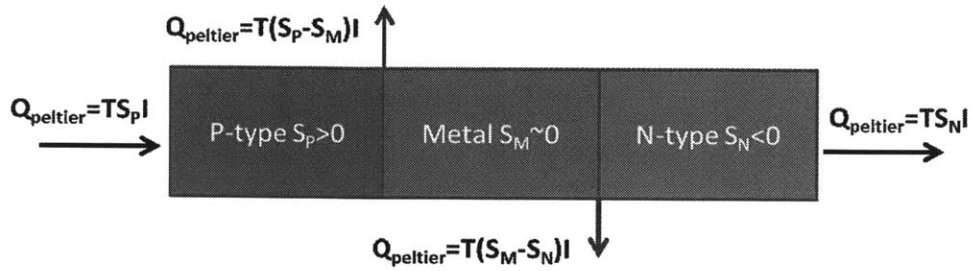


Figure 1-3: Peltier heat flow in a segmented material at uniform temperature. Heat transfer is localized at the interface where the Seebeck coefficient changes.

It is generally understood that heat flux is associated with entropy flux via $\vec{q} = T \vec{J}_s$. Dividing Eq.(1.6) by absolute temperature leads to

$$\vec{J}_s = S \vec{J} - \frac{k}{T} \nabla T \quad (1.8)$$

This equation reconfirms that the Seebeck coefficient is actually the entropy carried per particle.

Physically, charge carriers carry entropy proportional to the Seebeck coefficient. When an electron crosses an interface it enters a different material system with different available electron energy states. The entropy of the electron changes with the Seebeck coefficient and the electron undergoes a heat transfer with the lattice. In principle this is an isothermal heat transfer which occurs near the interface and is reversible with no entropy generation. Advanced transport theory from the Boltzmann equation reveals that the actual interface region has a thickness on the order of the mean free path of an electron and the temperature of the lattice may not be uniform.⁷

1.2. Governing Equation of Thermoelectricity

This section will derive the governing equation for thermoelectricity by using the constitutive relation for heat flux from the last section. This governing equation will be used later to solve for the heat and work transfers on the boundaries of a thermoelectric device. Consider an energy balance over an element of a thermoelectric material, figure 1-4. Energy is transferred in and out of the boundaries by three mechanisms: Peltier heat, Fourier heat conduction, and electrochemical potential.

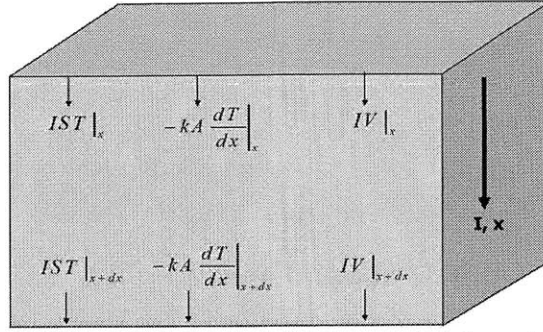


Figure 1-4: Energy balance in a differential element of a thermoelectric material. From left to right: Peltier heat, Fourier heat conduction, electrical power

An energy balance is applied to the volume element and a 1st order Taylor series expansion is performed on each term to give

$$-J \frac{dST}{dx} + \frac{d}{dx} \left(k \frac{dT}{dx} \right) - J \frac{dV}{dx} = 0 \quad (1.9)$$

The change in voltage can be rewritten from Eq.(1.5) to yield the following

$$\frac{\partial}{\partial T} \left(k \frac{dT}{dx} \right) \frac{dT}{dx} - JT \frac{\partial S}{\partial T} \frac{dT}{dx} + J^2 \rho = 0 \quad (1.10)$$

where ρ is the electrical resistivity, the second term is called the Thompson heat and $T d\alpha/dT$ is the Thompson coefficient. The Thompson heat is fundamentally similar to the Peltier heat except that the heat rejection/absorption takes place over some distance due to the temperature dependent Seebeck rather than at an interface of two dissimilar materials. The above equation is a 2nd order, non-linear, PDE, and two methods are often used in solving it. One method is to make use of a similarity variable to transform it into a 1st order, non-linear ODE.⁸ The second method which will be applied here is to make a simplistic assumption that all the properties are independent of temperature. This assumption is only valid over small temperature differences; chapter 2 will discuss the case when this assumption is not valid. Holding α, k, ρ constant we can rewrite Eq.(1.10) as the following,⁴

$$k \frac{d^2 T}{dx^2} + J^2 \rho = 0 . \quad (1.11)$$

The above equation is a standard heat conduction equation which can be solved with two boundary conditions $T|_{x=L} = T_C$ and $T|_{x=0} = T_H$ for the temperature distribution in the thermoelectric leg or element (L is the length of the element). The hot and cold side heat transfers Q_H and Q_C have contributions from the Peltier heat and Fourier heat conduction, figure 1-4. From the temperature distribution, the conducted heat can be calculated based on the Fourier law. The hot and cold side heat transfers are solved

$$Q_H = IST_H + \frac{kA\Delta T}{L} - \frac{I^2 \rho L}{2A} , \quad (1.12)$$

$$Q_C = IST_C + \frac{kA\Delta T}{L} + \frac{I^2 \rho L}{2A} , \quad (1.13)$$

The converted electrical power is solved by subtracting Q_H from Q_C ,

$$P_E = IS\Delta T - \frac{I^2 \rho L}{A} . \quad (1.14)$$

The solutions for heat transfer, Eq.(1.12) and Eq.(1.13), have contributions from three terms: the first term is the Peltier heat, the second term is the Fourier conduction heat, and the third term is from a dissipative Joule heating process. Ideally, the Peltier heat term would dominate in a good thermoelectric because the other terms generate entropy. The Fourier conduction terms represents heat that is conducted by electrons and phonons due to the temperature gradient rather than carried in the current. The Joule heating term is from electrical work dissipating in the element which leads to unwanted heating in heat pump mode, or electrical power loss in power generation mode.

Thermoelectric power generation and refrigeration manifest at the two interfaces. The bulk of the material is needed only as a conduit for charge carriers to travel between the two interfaces at high and low temperature. The other two properties k and ρ , represent intrinsic

losses in the conduit. The thermal conductivity represents a heat flow path parallel to the heat carried by the electric current. The electrical resistivity represents power dissipated by carrier transport.

1.3. Power Conversion and ZT

In this section the governing equation for thermoelectricity is applied to a real device to solve for the energy conversion efficiency. A new property called the figure of merit Z , will be defined which fully characterizes energy conversion efficiency. Consider a constant property, TE material operating as a heat engine with ends maintained at constant temperature and connected to an external load. The TE element is referred to as a TE *leg*, the current and heat transport is assumed to be one dimensional and furthermore, we assume no heat loss at the surface. The ends are connected to an electrical resistor by perfect conductors with a Seebeck coefficient equal to zero, so that thermoelectric effects in the leads are neglected. Heat flow through each boundary has three terms: the Peltier heat, the Fourier conduction heat, and the Joule heat. The electrical power term is now replaced by the load resistance, figure 1-5.

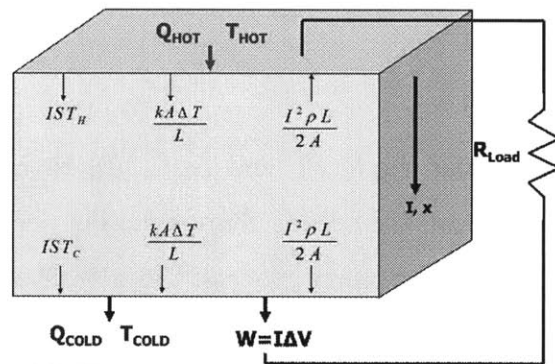


Figure 1-5: Thermoelectric energy balance, constant properties.

The conversion efficiency is equal to the electrical power dissipated in the load resistance over the hot side power input,

$$\eta = \frac{P_{\text{electrical}}}{Q_H} = \frac{S\Delta TI - I^2 \rho L / A}{IST + \frac{kA\Delta T}{L} - \frac{I^2 \rho L}{2A}} = \frac{I^2 R_L}{IST + \frac{kA\Delta T}{L} - \frac{I^2 R}{2}}. \quad (1.15)$$

We substitute in the resistance ratio $M = R_L/R$ where R is the internal resistance of the TE leg and R_L is the load resistance of the external circuit. The current is rewritten as

$$I = \frac{S\Delta T}{R(1+M)}. \quad (1.16)$$

The efficiency is now rewritten in terms of the Carnot efficiency times the second law efficiency

$$\eta = \eta_c \eta_{II} = \eta_c \frac{1}{\frac{(1+M)^2}{ZT_H M} + \left(1 + \frac{T_C}{T_H}\right) + 1}, \quad (1.17)$$

where $\eta_c = 1 - \frac{T_C}{T_H}$ is the Carnot efficiency and $Z = \frac{S^2}{\rho k}$ is a combination of material properties called the figure of merit. Equation (1.17) is a general equation for efficiency given the boundary temperatures, constant thermoelectric material properties and resistance ratio, M . However to find the maximum efficiency we must use the relation $\frac{d\eta}{dM} = 0$ to find the load matching condition corresponding to a maximum efficiency. Upon differentiating Eq.(1.17) with respect to M an optimal load matching condition and maximum efficiency are found below,

$$M = \sqrt{1 + Z\bar{T}}, \quad (1.18)$$

$$\eta = \eta_c \frac{M-1}{M + \frac{T_c}{T_h}} = \eta_c \frac{\sqrt{1+Z\bar{T}} - 1}{\sqrt{1+Z\bar{T}} + \frac{T_c}{T_h}}, \quad (1.19)$$

where $\bar{T} = (T_H + T_C)/2$ is the mean temperature and $Z\bar{T} = \frac{S^2\bar{T}}{\rho k}$ is called the dimensionless figure of merit. ZT is the most useful non-dimensional number the thermoelectric community employs because this property alone determines the heat to electrical conversion efficiency.^{4,9,10} The commercial standard TE modules use materials with $Z\bar{T} \leq 1$. A common assumption in device design is to assume $Z\bar{T}$ is constant over a limited temperature range. A similar treatment can be done for a TE heat pump and will yield similar results for the importance of the figure of merit.²

The three thermoelectric properties and ZT are generally temperature dependant, while electrical contact resistance and heat leakage at the sidewalls of the legs affect ZT . When the temperature difference is large it is often convenient to think of a TE material, module or an entire thermoelectric generator (TEG) in terms of its “effective properties”. We define an effective ZT , $Z\bar{T}_{eff}(T_C, T_H)$ which can be used in Eq.(1.19) to solve for efficiency and includes the effects of temperature dependent properties, contact resistance and parasitic electrical and thermal resistances. In this method (derived in chapter 2) we ignore the explicit temperature dependence of the properties and instead use the temperature averaged values as if they were constant with temperature. This technique can simplify calculations while maintaining high accuracy, allowing one to more intuitively analyze the problem on the device level. We define three classes of interrelated properties:

- “Intrinsic properties” $S(T)$, $\rho(T)$, $k(T)$ are the three thermoelectric properties introduced previously.
- “Device properties” are the directly measurable values, including the heat transfer rates Q_C, Q_H , open circuit Seebeck voltage V_S , and electrical resistance R .
- “Effective properties” $S_{eff}(T_H, T_C)$, $k_{eff}(T_H, T_C)$, $\rho_{eff}(T_H, T_C)$ are the equivalent constant property values, in general they are a function of T_H, T_C .

1.4. Semiconductors as Thermoelectrics

Good TE materials have a high figure of merit and therefore require a high Seebeck coefficient, a high electrical conductivity, and a low thermal conductivity. This is a very unusual combination of properties; for instance, usually good electrical conductors like metals also have high thermal conductivity. While most thermally insulating materials like plastics and ceramics are also electrically insulating. This section will explain why semiconductor materials hold the greatest potential as TEs. The three thermoelectric properties S, k, ρ are not independent, so it is hard to change only one property without changing the others. For example, increasing the number of electrical carriers not only increases electrical conductivity but also increases thermal conductivity, and decreases Seebeck coefficient. Both electrons and phonons (lattice vibrations) contribute to the thermal conductivity of a material; the electron contribution dominates in metals while phonons are dominant in most semiconductors and insulators. The Seebeck coefficient decreases as the carrier concentration increases.⁷ Figure 1-6 illustrates each of three properties as a function of carrier concentration. As the figure shows, metals have high electrical conductivities, but also high thermal conductivities and low Seebeck coefficients. Insulators have high Seebeck coefficients and potentially low thermal conductivities, but these properties are countered by low electrical conductivities. The best thermoelectric materials which produce the highest ZT s are semiconductors. Moreover, in semiconductors electrical conductivities and carrier type can be easily changed with minimal effect to other properties, simply by changing the doping type and doping concentration. With dopants, electrical conductivity of semiconductors can reach up to the order of 10^5 S/m. The contribution of electrons to thermal conductivity is not dominant for most semiconductors, so a change in doping concentration has a minor effect on thermal conductivity. Optimizing the doping concentration is an important aspect of developing thermoelectric materials.

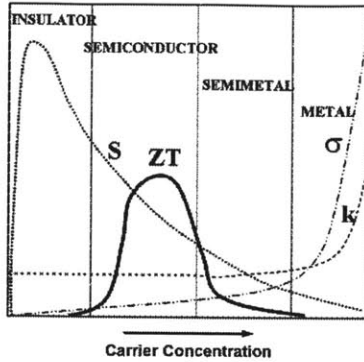


Figure 1-6: Thermoelectric properties S , σ , k (Seebeck coefficient, electrical conductivity, thermal conductivity) as a function of carrier concentration. Semiconductors make the best thermoelectric materials.

1.5. State of the Art and Device Design

Thermoelectric devices operate as heat engines or heat pumps and are primarily made from semiconductor materials. When the majority of electrical carriers are electrons, i.e., an n-type semiconductor, the Seebeck coefficient and the Peltier coefficient have negative values because direction of electron movement is opposite to that of the current. On the other hand, when the majority of electrical carriers are holes, i.e., a p-type semiconductor, the Seebeck coefficient and the Peltier coefficient have positive values. Thermoelectric devices are made with pairs of p-type and n-type TE elements or “legs”. A p-type leg is arranged electrically in series and thermally in parallel with an n-type leg to form a “thermocouple couple”. Figure 1-7 shows a schematic of a typical thermocouple running as a heat engine and as a heat pump.

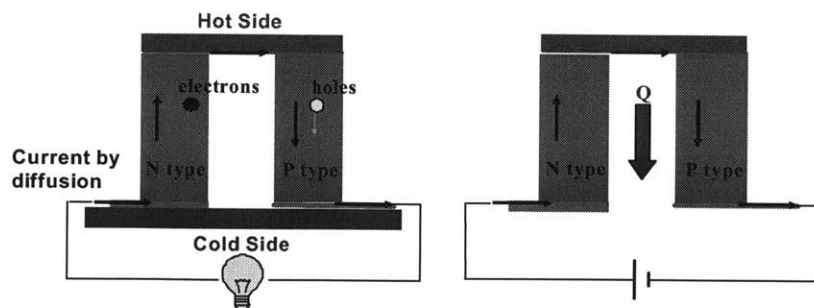


Figure 1-7 Schematic of thermoelectric devices, (left) power generator (right) and thermoelectric cooler.

Thermoelectric devices have been used in a several niche markets like small scale refrigeration, and radioisotope generators. The most successful long term implementation of TE devices has been in NASA’s deep-space spacecraft where thermoelectrics have been used to

generate power from a radioisotope (nuclear) fuel source, figure 1-8b. When a spacecraft travels to the outer solar system, solar radiation is too weak to be used as an energy source. In this case, the spacecraft's electrical power is generated by a thermoelectric heat engine operating between a hot nuclear fuel source and cold space. One such RTG weighs about 55 kg and produces about 240 Watts of electricity at about 7% conversion efficiency. The hot side is maintained at 1300 K by a graphite-encased plutonium heat source and the cold side radiates heat into space at 600 K. There is no 'off' switch: the radioisotope has a half-life of 87 years.¹¹ TE refrigerators have recently been used in high-end automobile seats to deliver temperature controlled air throughout the seats, figure 1-8a. Thermoelectric devices have several advantages in their design and operation:

- 1) No moving parts. They are solid state materials with no moving parts, no acoustic noise, and the material itself requires no maintenance. The entire system design is greatly simplified over conventional cycles because there is no working fluid and fewer components.
- 2) Reliability. TE materials are very stable when operated in the proper temperature range. NASA has used TEGs in missions lasting for decades and even in the harsh environment of space, these generators have accumulated more than a trillion device-hours without a single failure.¹¹
- 3) Scalability. TE devices can be implemented into anything from integrated circuits and MEMS to industrial sized waste heat recovery and can have high power densities. TE devices are easily scalable over a huge range but are out competed by other heat engine and refrigeration cycles at large scale.
- 4) Reversible. TE devices can be switched from power generation mode to refrigeration mode simply by reversing the current, allowing for superior temperature control.

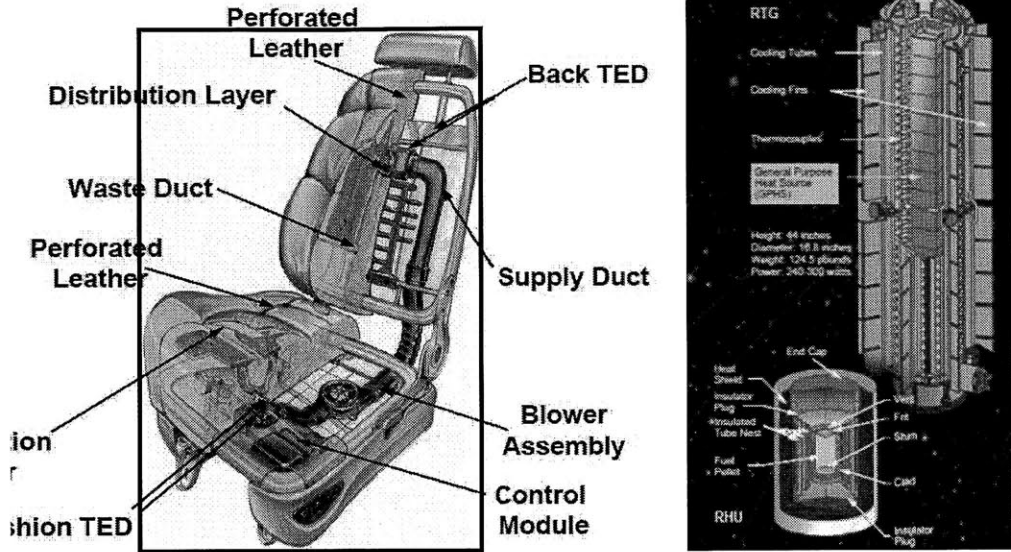


Figure 1-8: TE devices (left) TE cooler in a car seat (right) TE generator used in NASA space missions. ^{*†}

Figure 1-9 plots the second law efficiency from Eq.(1.19) versus ZT . It is believed that TEs could begin replacing large scale refrigeration cycles at ZT s around 3-4 corresponding to second law efficiencies of 38-45%.² Thermoelectric generator second law efficiencies may never be directly competitive with traditional large scale heat engines like steam and gas turbines that have second law efficiencies above 60%. However TEGs may play a large role in combined cycle applications where TEGs operate at the hot side of an existing heat engine such as in a steam boiler or the cold side—known as *waste heat recovery*--such has in the exhaust stream of an internal combustion engine.

* <http://amerigon.com/>

† <http://www.energyscience.ilstu.edu/areas/thermal.shtml>

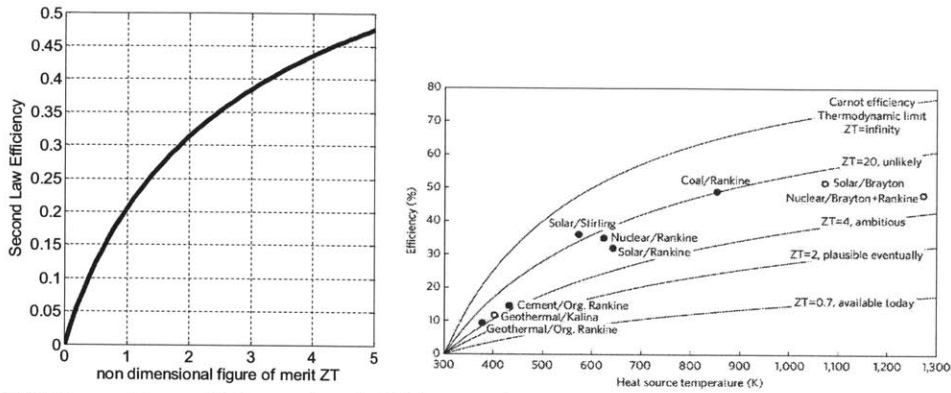


Figure 1-9: (left) Second law efficiency (total efficiency divided by Carnot efficiency) vs. ZT for $T_H=500$ K and $T_C=300$ K. (right) Conversion efficiency of thermoelectric generator operating from room temperature on the cold side up to 1300K. Existing heat engine cycles achieve higher efficiency than state of the art thermoelectrics.¹²

Over the last several decades the non-dimensional figure of merit has remained at a maximum value of about unity. However, recent developments in nanostructured thermoelectric materials have produced significantly higher figures of merit (figure 1-10). The following excerpt from Hendricks describes the state of the art.¹ “Research at NASA-JPL, MIT-Lincoln Labs, Michigan State University, and other organizations from about 1995 to the present has led to the discovery, characterization, and laboratory-demonstration of a new generation of TE materials: skutterudites, thin-film superlattice materials, quantum well materials, and PbAgSbTe (LAST) compounds and their derivatives¹ These materials have either demonstrated ZT of ~ 1.5 -2 or shown great promise for higher ZT approaching 3 or 4. Quantum well materials include 0-dimensional (0-D) dots, 1-dimensional (1-D) wires and 2-D thin-film materials. These materials make it possible to create TE systems that display higher ZT values than those obtained in bulk materials because quantum well effects tend to accomplish two important effects: 1) they tend to significantly increase density of states which increases the Seebeck coefficient in these materials; and 2) they tend to de-couple the electrical and thermal conductivity allowing quantum well materials to exhibit low thermal conductivities without a corresponding decrease in electrical conductivity. The LAST compounds have shown embedded nanostructures within the crystal matrix that may exhibit quantum well effects.”¹

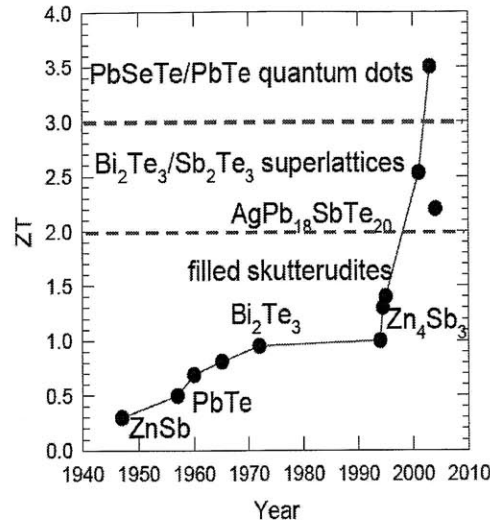


Figure 1-10: Timeline of ZT over the past 60 years.¹ The materials above ZT=2 are thin films, which are inherently difficult to measure and have been contested.

TE materials have temperature dependent properties and temperature dependent ZT values. Each material has a finite operating temperature range around the maximum ZT value which means if a device is to operate over a large temperature range then more than one material system must be employed. Figure 1-11 plots the temperature dependent ZT values for different material systems.

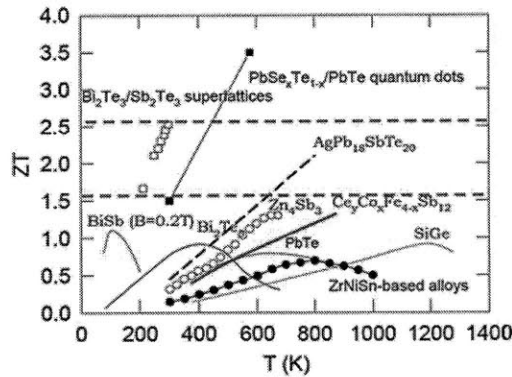


Figure 1-11: ZT vs. temperature for different material systems¹

Although there are many reports of nano-featured TE materials with high ZT s few of these materials can be fabricated economically or in sufficient quantities. Thin film thermoelectrics are inherently difficult to measure accurately, some results have been contested which hurts the credibility of the thermoelectrics community. It is wise to be skeptical of thin film results and critically consider the experimental techniques. Bi_2Te_3 is the best bulk

thermoelectric around room temperature and is the only commercially available TE. Bi_2Te_3 has been widely used in small scale refrigeration for decades and has recently been seriously considered for power generation. Researchers have taken a renewed interest in thermoelectric power generation in light of pressing issues of energy and environment the world faces in the 21st century. The challenge is to create a TE material that is economical and scalable to large systems in order to improve energy efficiency and energy conservation.

1.6. Nanocomposite Method

The groups at MIT and BC lead by Gang Chen and Zhifeng Ren have been successful at increasing ZT in several material systems using the nanocomposite method.¹³⁻¹⁶ Thermoelectric nanocomposites have small grains that preferentially scatter phonons and reduce the thermal conductivity while keeping the power factor similar to the bulk. It is an inexpensive method to introduce nanostructures into the material and can produce arbitrarily large samples sizes.

We employ two methods of skutterudite powder preparation. The *melt* method creates a bulk crystalline skutterudite from a stoichiometric mixture of elements which is vacuum sealed in a quartz tube and heated in a furnace. Then the mixture is quenched to produce a bulk crystalline skutterudite. The challenge is to create a homogeneous mixture and prevent the rare earth elements in the skutterudites from reacting with the quartz.¹⁷ Next the material is ground into a powder by the high energy ball-mill (figure 1-12). The bulk skutterudites are loaded in a steel jar with steel spheres and sealed under an Ar atmosphere in a glove box. The high energy ball-mill machine is run for on the order of 10 hrs until the desired grain size distribution is reached.

The *elemental ball-mill* (EBM) method combines the first and second steps of the last method. Pure elements are added to the BM at the desired stoichiometry and run for a long time period. The skutterudite compound forms by mechanical alloying. Mechanical alloying occurs through a repeated process of fracture and cold welding of powder particles trapped between grinding balls.² The average temperature inside BM jar is less than 100°C, while the local temperature can be raised to the alloy temperature through heat generated by collisions of the balls with the materials; this is the driving force for the inter-diffusion of the components.² The

EBM method is straightforward but produces inhomogeneous samples with many defects compared to the melt method.

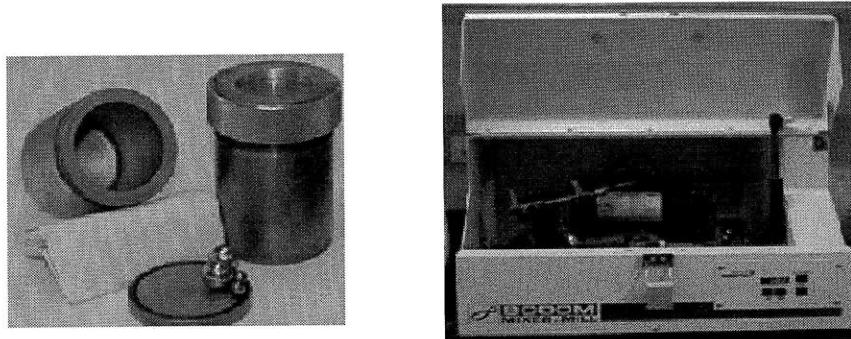


Figure 1-12: Stainless steel jars and the Ball mill machine (Spex 8000M)

The next step is to sinter the powder into a dense pellet by the direct hot press (DHP) process (figure 1-13). The powder is loaded in a graphite die (performed in a glove box in N_2 atmosphere), which is a hollow cylinder that is sealed with graphite plungers on either end. The loaded die is put on a *carver press* at a constant pressure of around 60-80 MPa. A current of 200-1600 A is supplied and heats the die via Joule heating. A thermocouple is located near the sample to monitor the temperature during press. When the temperature reaches $\sim 700^\circ C$, it will be maintained for several minutes by adjusting the current. The samples come out as pellets as shown in figure 1-13 and are cut into discs and bars, and polished for characterization of thermoelectric properties. The advantages over traditional hot press which heats the die in a furnace rather than using DC resistive heating are: (1) The heating speed is fast, samples can be heated up to $700^\circ C$ in less than 5 minutes. (2) The cooling can also be fast, reaching room temperature in less than 6 minutes. With short times at high temperature we hope to preserve the small grain size of the powder during sintering.

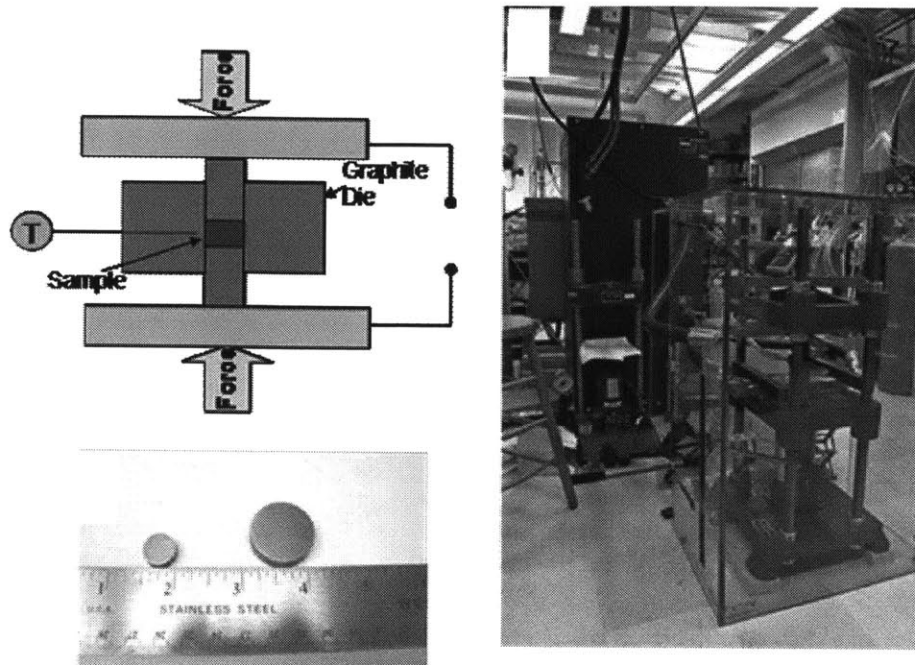


Figure 1-13: Pictures of hot press. (top left).Schematic drawing of the hot press (right). Homemade hot press system at Boston College (bottom left). 0.5 inch and 1 inch consolidated samples.¹⁷

1.7. Individual Property Measurements

The performance of a thermoelectric material is characterized most commonly by its so-called dimensionless figure of merit $Z\bar{T} = S^2\bar{T}/\rho k$. The three properties are highly temperature dependent, and to measure each represents a formidable task. The following will describe the methods and instrumentation used to measure each property as a function of temperature, they will be referred to collectively as the *individual property measurements*.

Typically the skutterudite samples were pressed into a 4 mm thick, 1/2" diameter disk. The disk was cut in half to produce two 2 mm thick discs, one would be used to measure thermal conductivity and the other would be cut again into 2 x 2 x 11 mm bars and used to measure Seebeck and electrical.

The thermal conductivity was measured by a commercially available laser flash system made by Netzsch Instruments (figure 1-14). The Laser flash method was developed by Parker in 1961.¹⁸ It is the most common method for measuring the thermal conductivity of bulk samples well above ambient temperature.^{19,20} The sample is first polished to a uniform thickness and then coated with graphite spray. A laser pulse creates a temperature rise on one side and the transient

thermal response is measured on the other side. From the response one can extract the thermal diffusivity and specific heat and solve for the thermal conductivity by $k = \alpha \rho c_p$, where ρ in this case is the density (measured directly). The specific heat is either found by literature values, or measured by the laser flash (largest uncertainty), or a different scanning calorimeter (DSC).¹⁷ The thermal conductivity is measured in the cross-plane direction and has a nominal uncertainty of 8%.

The Seebeck and electrical are measured simultaneously on the commercially available ZEM-3 instrument (figure 1-14). The instrument is commonly used by many thermoelectrics research groups. The sample is held between two jaws by pressure from the clamp springs. Inside the lower jaw is an electrical resistance heater, which creates the temperature gradient along the sample. Temperature and voltage are measured by the lower and upper thermocouples and pressed against the sample by a spring force. It is critical to establish good electrical and thermal contact at the thermocouples. The Seebeck is measured with a small temperature difference across the sample on the order of 5°C. The 4-wire electrical resistance is measured under isothermal conditions. The distance between thermocouple contacts is measured by a digital camera and software. Both the electrical and Seebeck are measured in the in-plane direction and have nominal uncertainty values of 8% and 5% respectively. The resulting nominal uncertainty in ZT for the individual properties measurement is 14%. The in-plane versus cross-plane measurements have important implications on material characterization and will be discussed in the next section.

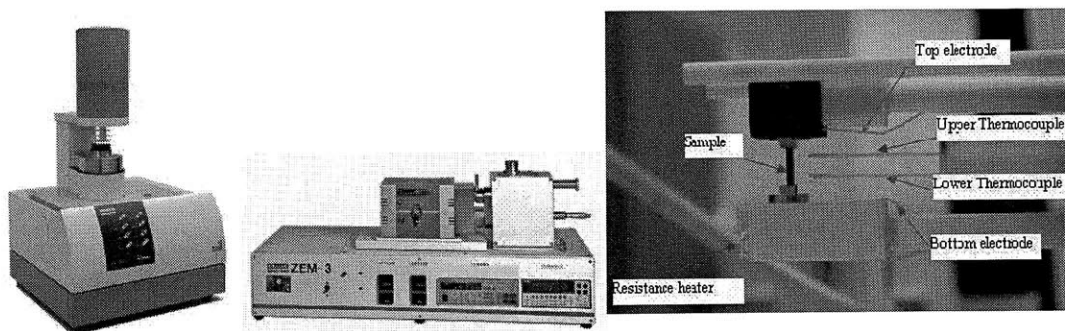


Figure 1-14: (left) Laser flash system to measure the thermal conductivity. (middle) ZEM-3 system to measure the electrical conductivity and Seebeck coefficient. (right) Sample mounting system of the ZEM-3.

1.8. Device Measurements

It is convenient to conceptually break up thermoelectrics research into three domains: materials research, device testing and applications. In the materials research stage we are trying to optimize ZT for a given material in a given temperature range. This stage ends with characterization by individual properties measurements and produces ZT versus temperature. Applications research is the furthest downstream and studies how TEGs can potentially be integrated into various systems.

The device testing stage is needed to link the high ZT materials to its applications. The goals of this stage is to first verify and demonstrate the high ZT with a device measurement and then to package the materials into a fully functional module. Key design considerations for a module are thermal stresses, chemical stability and parasitic electrical and thermal resistances. Whereas before there was a single material to optimize, now we must consider the performance of several materials working together. Therefore we must know not only the thermoelectric properties of all the materials but the thermomechanical properties as well.

The thermoelectrics community has suffered from many false claims of high ZT values and thus researchers are skeptical of each other's ZT reports. It is easy to understand how large experimental uncertainties accumulate for even the most careful experimentalist. The individual properties measurement previously described produce a nominal uncertainty of 15% in ZT if performed correctly on bulk, isotropic samples. However the total uncertainty can easily be much larger. Often times the properties are measured in different directions on different samples which are falsely assumed to be homogeneous and isotropic and assembled into a single ZT. Many thermoelectrics are not bulk samples and are measured by custom techniques on homebuilt systems. There is always the possibility of systematic error introduced on homebuilt instruments or miss used commercial instruments. There is variability in the synthesis of all thermoelectrics, and it is tempting to report the highest measured properties as "lucky samples" when they are in fact outliers due to experimental uncertainty.

The device testing domain of thermoelectric research is commonly considered as lagging behind the materials research. However, there is impressive and ground breaking work done by many research groups in the literature. The thermoelectric efficiency of radioisotope generators (RTG) employed on current US space missions is 8%, while the system efficiency is further reduced by 10-15% due to electrical and thermal losses.²¹ The generator uses SiGe legs and

operates between 1275K and 575K. Sublimation of thermoelectric materials near the hot junction is a problem for all high temperature TEGs. The RTG is designed such that the reduction in power due to sublimation is limited to 5-10% over ten years, and corresponds to a sublimation rate at the legs of $6-10 \times 10^{-7} \text{ g/cm}^2/\text{hr}$. The legs were coated with Si_3N_4 and wrapped in quartz yarn to reduce sublimation. Ravi *et al.* studied the thermomechanical stress of a theoretically proposed uncouple made from skutterudites bonded to SiGe.²² Kambe *et al.* built a novel SiGe-Bi₂Te₃ module encapsulated in a steel water jacket with mechanically compliant pads to promote good thermal contact while allowing for thermal expansion.²³ El-Genk *et al.* build a segmented uncouple with skutterudites and Bi₂Te₃, and conducted device tests for hundreds of hours. The calculated* efficiency was originally 13.8% but degraded to 6% after 3500 hrs; the actual measured peak efficiency before correction of thermal losses was 7.3%.^{24,25} A metallic coating was applied to the hot side of the legs to suppress Sb sublimation.²⁶ Salzgeber *et al.* reported progress of skutterudite material, heat exchanger design, module integration, and cost for automotive applications.²⁷ The authors found that the driving distance for return on investment is 100,000 km for skutterudites compared to 200,000 km for Bi₂Te₃, PbTe, and TAGS based TEGs. Rogl *et al.* claimed high ZT skutterudites including a P-type with $ZT > 1$.²⁸ They calculated the efficiency of the legs operating between 800K and 300K to be 12.6% and 13.8% for the P-type and N-type respectively, but have not demonstrated this performance with a device test. The highest measured efficient of a skutterudite uncouple was 10.35% at hot side and cold side temperature of 619°C and 43°C respectfully.²⁹ However this value assumes zero side heat losses and the authors do not give a good description of how the heater power was measured and corrected.

1.9. Scope and Organization of this Thesis

This thesis will focus on the device testing and applications research domains. Chapter 2 describes the development of a novel device testing method to be used in the room temperature range, up to 230°C. A mathematical method is derived to extract the intrinsic properties from

* Efficiency calculated based off measured power output and large heater losses.

the device properties. Chapter 4 is an extension of this method into the mid-temperature range up to 600°C. New instrumentation was designed to operate in this temperature range. Electrode materials were bonded to the skutterudites during press, and offer a promising solution for future module fabrication. Chapter 4 explores the possibility of a hypothetical solar thermoelectric topping in the mid-temperature range. A parametric study was performed to analyze the efficiency of the new proposed system.

Chapter 2. Device Properties and Efficiency Measurement Method

In this chapter we develop methods to characterize a single TE leg operating under a large temperature difference. We will extract the three intrinsic properties of a single leg from measured device properties and verify the results by comparing the predicted power conversion efficiency from the property measurements to the actual measured efficiency. Such testing conditions provide a more realistic examination of actual TE device performance and thus support the development and design of future TE power generators.

Contributions to the field include development of an experimental technique capable of directly measuring an energy balance over a single leg, with a large temperature difference ranging from 2 °C to 160 °C. The technique measures all three TE properties of a single leg, in the same direction, with significantly less uncertainty than other methods. The measurements include the effects of temperature dependent properties, side wall radiation, and contact resistance. The power and efficiency were directly measured and are within 0.4 % and 2 % of the values calculated based on the property measurements. Previous work on the efficiency measurement can be found in Muto's master thesis.⁸ In this work the experimental system has been redesigned and a method is developed to extract the intrinsic properties from the effective properties. The work in this section was published in *Review of Scientific Instruments*.³⁰

2.1. Introduction

The performance of a thermoelectric material is characterized most commonly by the dimensionless figure of merit $Z\bar{T} = S^2\bar{T}/\rho k$ or intrinsic ZT . The three temperature-dependent properties or “intrinsic properties” $S(T)$, $\rho(T)$, $k(T)$ are the Seebeck coefficient, electrical resistivity, and thermal conductivity respectively, and \bar{T} is the mean absolute temperature. The intrinsic properties are highly temperature dependent, and to measure each represents a formidable task.

Typically one of two methods is used to characterize a TE material over a small temperature difference: 1) the Harman method³¹ 2) the three intrinsic properties are measured

independently over small temperature differences.⁴ The original Harman is used to measure $\rho(T)$ and $Z\bar{T}(T)$ over small temperature differences.^{31,32} This technique has many variations and has been applied to bulk modules and thin films alike.^{33,34} The drawbacks are that it only works over small temperature differences and requires adiabatic boundary conditions that can be difficult to satisfy.³⁵ The second method uses different measurement systems for each individual property.^{4,36,37} Often, all three properties are not measured on the same sample or along the same direction. The second method is very time consuming, and both methods can result in large uncertainties in $Z\bar{T}(T)$, often greater than 10%.³⁸

Thermoelectric power generators usually operate under large temperature differences up to hundreds of degrees centigrade. If $Z\bar{T}$ is temperature independent, the maximum efficiency η_{\max} of a thermoelectric element can be expressed as^{4,9}

$$\eta_{\max} = \frac{T_H - T_C}{T_H} \frac{\sqrt{1 + Z\bar{T}} - 1}{\sqrt{1 + Z\bar{T}} + T_C/T_H}, \quad (2.1)$$

where T_H is the hot side temperature, and T_C is the cold side temperature. However, since the intrinsic properties vary strongly with temperature along the length of the element or “leg”, Eq.(2.1) is not applicable and often numerical solutions must be used to obtain the actual device efficiency.³⁹ Furthermore, in real TE applications additional effects must also be considered such as electrical contact resistance at the junctions of the TE legs and radiation losses from the leg side walls.^{40,41}

2.2. Mathematical Formulation

2.2.1 Governing Equation

Figure 2-1 is a general schematic of a p-type TE sample under test, where the hot side heat transfer rate Q_H enters from the top at T_H and the cold side heat transfer rate Q_C exits the bottom at T_C . The temperature is measured by thermocouples, and ΔT ranges from 2 °C to

160 °C. The electrical current I enters from the top and exits through the bottom of the sample, and V_{TE} is the TE voltage measured across the leg at the position of the thermocouples. We will directly measure the energy balance over the sample, which includes Q_H , Q_C , and the electric power $P_e = IV_{TE}$. We will show that since the temperature difference across the leg is large it is useful to characterize the TE leg in terms of its effective properties, resulting in an “effective ZT”, $Z\bar{T}_{eff}(T_H, T_C)$. We define three classes of interrelated properties:

- “Device properties” are the directly measurable values, including the heat transfer rates, Seebeck voltage, and electrical resistance.
- “Effective properties” $S_{eff}(T_H, T_C)$, $k_{eff}(T_H, T_C)$, $\rho_{eff}(T_H, T_C)$ are obtained directly from device properties measurement when the hot side is at T_H and cold side at T_C , or can be calculated by integrating the intrinsic properties over the temperature interval.
- “Intrinsic properties” $S(T)$, $\rho(T)$, $k(T)$ are properties of the materials at each temperature as previously defined, which will be extracted from the effective properties.

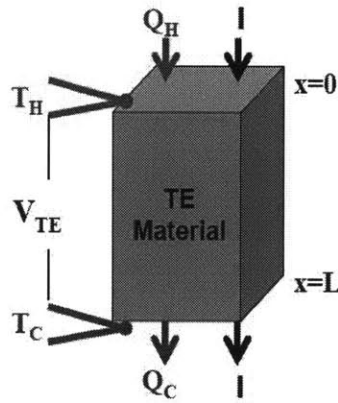


Figure 2-1:. Illustration of a p-type thermoelectric leg under working conditions.

The constitutive relations for one-dimensional heat flux q , and current density J , are given in Eq.(1.2) and Eq.(1.6) and but are reprinted here for convenience⁵

$$q = JTS - k \frac{dT}{dx}, \quad (2.2)$$

$$J = -\frac{1}{\rho} \frac{dV_{TE}}{dx} - \frac{S}{\rho} \frac{dT}{dx}. \quad (2.3)$$

An energy balance over a one-dimensional differential element of a TE leg yields

$$A \frac{d}{dx} \left(k \frac{dT}{dx} \right) - IT \frac{dS}{dx} + I^2 \frac{\rho}{A} - \varepsilon \sigma_{sb} P (T^4 - T_\infty^4) = 0, \quad (2.4)$$

with four terms on the left hand side representing the heat conduction, the Thomson heat, the Joule heat and the radiation loss. Here A is the cross sectional area, ε is the emissivity, σ_{sb} is the Stephan-Boltzmann constant, P is the perimeter, and T_∞ is the ambient temperature. The leg is kept under high vacuum (5×10^{-5} Torr) such that natural convection and air conduction can be neglected.

2.2.2 Device Properties Measurement under Large ΔT

The measured device properties are the open circuit Seebeck voltage V_S , the open circuit heat transfer rates $Q_{H,oc}$, $Q_{C,oc}$ and the electrical resistance of the leg R . Measuring these device properties directly as a function of temperature enables us to determine the effective properties, and finally solve for the intrinsic properties. In general V_{TE} is composed of a Seebeck voltage and an Ohmic voltage drop. During the properties measurement $I=0$, it follows from Eq.(2.3) that $V_{TE} = V_S$ and is related to $S_{eff}(T_H, T_C)$ and $S(T)$ by

$$V_S(T_H, T_C) = S_{eff}(T_H, T_C) \Delta T = \int_{T_C}^{T_H} S(T) dT. \quad (2.5)$$

Equation (2.4) is reduced to only the heat conduction and the radiation terms and can be solved to give expressions for $k_{eff}(T_H, T_C)$ and $k(T)$

$$Q_{H,oc}(T_H, T_C) = \frac{A}{L} k_{eff}(T_H, T_C) \Delta T = \frac{A}{L} \int_{T_C}^{T_H} k dT + Q_{rad}, \quad (2.6)$$

$$Q_{C,OC}(T_H, T_C) = Q_{H,OC} - Q_{rad,side} = \frac{A}{L} \int_{T_C}^{T_H} k dT + Q_{rad} - Q_{rad,side} \quad (2.7)$$

Here, Q_{rad} is the additional heat transfer rate on the hot side due to radiation from the side walls and $Q_{rad,side}$ is the total radiation loss from the side walls (see Appendix A: Radiation Correction). The geometry of the leg was chosen to minimize the effects of radiation, where $Q_{rad,side} < 2\%$ of $Q_{H,OC}$ and $Q_{rad} < Q_{rad,side}$. The heat transfer rates $Q_{H,OC}$ and $Q_{C,OC}$ are measured by a calibrated heater on the hot side and a heat flux sensor on the cold side which will be described in more detail in the Experimental System section.

The electrical resistance is measured by a 4-wire AC method when the leg is under a temperature gradient.⁴ The resistance measurement is applied in the limit that the current is small such that the Joule heat term can be neglected and the modulation frequency is high such that the Peltier heat alternates sign and cancels due to periodic heating and cooling at the junctions. The electrical resistance R , is related to $\rho_{eff}(T_H, T_C)$ and $\rho(T)$ by

$$R(T_H, T_C) = \frac{L}{A} \rho_{eff}(T_H, T_C) = \frac{1}{A} \int_{T_H}^{T_C} \frac{\rho dT}{dx} \approx \frac{L}{A} \frac{\int_{T_C}^{T_H} k \rho dT}{\int_{T_C}^{T_H} k dT}, \quad (2.8)$$

whereby we have neglected the radiation term to approximate the temperature gradient as

$$dT/dx \approx -Q/kA, \text{ where } Q = (A/L) \int_{T_C}^{T_H} k dT \text{ is the conducted heat, which is constant.}$$

2.2.3 Efficiency

Unlike the device properties measurement which is conducted under the open circuit condition, the efficiency η , must be measured when electrical current flows through the leg. The efficiency is defined as

$$\eta = \frac{P_e}{Q_H} = \frac{P_e}{Q_C + Q_{rad,side} + P_e}, \quad (2.9)$$

where the electrical power output P_e can be obtained from Eq.(3),

$$P_e = IV_s - I^2 R = IV_{TE} \quad (2.10)$$

Power is produced when the voltage has increased in the direction of the current flow. In this way we use a current source to control I and measure V_{TE} , another method would be to measure the power dissipated over an adjustable resistor.^{42,43} Both methods are equally valid, but experimentally the current source method has many advantages. We integrate Eq.(2.4) twice with respect to x and apply the boundary conditions illustrated in figure 1-1 to solve for the temperature gradient. The temperature gradient is then used to evaluate Q_H and Q_C from Eq.(2.2)

$$Q_C = IT_C S(T_C) + Q_{C,OC} + \frac{1}{2} I^2 R + \frac{1}{2} I \beta \quad (2.11)$$

$$Q_H = IT_H S(T_H) + Q_{H,OC} - \frac{1}{2} I^2 R - \frac{1}{2} I \beta \quad (2.12)$$

where the Thompson heat is written as

$$\beta(T_H, T_C) = \int_{T_C}^{T_H} T \frac{dS}{dT} dT \quad (2.13)$$

Equations (2.11) and (2.12) appear similar to the constant property heat transfer rate Eq.(1.12) and Eq.(1.13)^{4,9,44} but remember that in this case, R and β are the temperature integrated quantities described above and $Q_{H,OC}$, $Q_{C,OC}$ include the effects of sidewall radiation. The factors of $\frac{1}{2}$ in front of the Joule heat and Thompson heat terms are the result of an approximation that assumes both heating terms are distributed uniformly throughout the material such that half goes to the hot side and half goes to the cold side. If ρ , $T d\alpha/dT$ are independent

of temperature then the factors of $\frac{1}{2}$ are exact (see Appendix A: Radiation Correction). When solving for R during power generation we make a second approximation that the temperature gradient is defined by the intrinsic thermal conductivity alone as we have done in Eq.(2.8).

2.2.4 Effective ZT

If we approximate $S(T_H) \approx S(T_C) = S_{eff}$, then the Thompson heat term drops out and Eq.(2.9) can be written in terms of the effective properties. In the same way $Z\bar{T}(T)$ was derived for intrinsic properties^{4,9} we can define $Z\bar{T}_{eff}(T_H, T_C)$ based on the effective properties,

$$Z\bar{T}_{eff} = \frac{S_{eff}^2 \bar{T}}{\rho_{eff} k_{eff}} = \frac{V_S^2 \bar{T} / |\Delta T|}{RQ_H} \quad (2.14)$$

It can be used to solve for the maximum conversion efficiency (Eq.(2.1)) and maximum coefficient of performance of a real device by using the conventional ZT formulas. Thus $Z\bar{T}_{eff}$ is a useful concept for the design engineer because it is a measure of the TE material quality over a large ΔT .

2.3. Experimental System

Conceptually the experimental system is similar to that shown in figure 1-1 but with a few complications. One requirement for testing a TE sample is that the sample must be a device-ready leg with metallization on both ends. For Bi_2Te_3 -based TE elements, the metallization material most commonly used is Ni, and its purpose is to allow soldering with low electrical and thermal contact resistances while acting as a diffusion barrier.⁴⁰ In the following analysis, no distinction is made between the intrinsic properties of the bulk and the properties of the contact. If significant contact resistances are present, they will be automatically lumped into the effective properties. Most samples that were measured had electrical contact resistances estimated to be < 5 % of the total resistance. The sample was a Bi_2Te_3 p-type leg from Marlow Industries with dimensions of approximately $1.6 \times 1.6 \times 1.6 \text{ mm}^3$.

Figure 2-2a illustrates the system designed to measure the device properties and energy conversion efficiency of the TE leg. Figure 2-3 shows a photograph of the actual assembly. The system is composed of the following elements: the hot assembly, the TE leg, the cold assembly, and the surrounding vacuum chamber. The hot assembly is soldered to the top of the leg and consists of a calibrated electrical heater providing Q_H , a thermocouple measuring T_H , and an electrode conducting I . The cold assembly is soldered to the cold side of the leg and consists of a copper heat spreader, a thermocouple measuring T_C , an electrode, a calibrated thermopile type heat flux sensor measuring Q_C , and a heater used for calibration. The bottom side of the heat flux sensor is mounted to a TE cooler module which was used in the efficiency measurement to control T_C independent of T_∞ in order to reduce heat losses at the cold assembly. The electrodes supply current to the TE leg for the resistance and efficiency measurements and are controlled by an external power supply. The entire assembly is contained in a vacuum chamber at a pressure of 5×10^{-5} Torr and a uniform ambient temperature, T_∞ of 22 – 24 °C.

Prior to mounting the leg, the hot assembly was suspended (figure 2-2b) and calibrated for heat loss. In this case the Joule heating IV_{Heater} will be balanced by the radiation and conduction losses. The hot assembly electrodes are very thin to minimize heat conduction losses but this means it produces a relatively large unknown Joule heating term for $I \neq 0$ and thus Q_H cannot be accurately measured during the efficiency measurement. Radiation losses at the cold assembly are negligibly small. The primary heat loss is from conduction along the electrodes which are much thicker than the hot assembly electrode. In order to calibrate the flux sensor the cold assembly electrodes were disconnected from the outside circuit. The voltage response of the flux sensor was measured for different heat fluxes imposed by the calibration heater which is mounted to the side of the cold assembly. After the flux sensor calibration, the thermal conductance of the electrodes was measured by mounting another heater to the end of the electrodes and measuring the temperatures T_E and T_C (figure 2-2b), in which the radiation loss of the electrodes is negligible compared with the heat conduction along the electrode. The electrical resistance between the positions of T_E and T_C was measured which allows us to solve

for the Joule heating inside the electrode when $I \neq 0$. We correct for Joule heating in Q_C but not in Q_H , therefore we rely only on Q_C during the efficiency measurement.

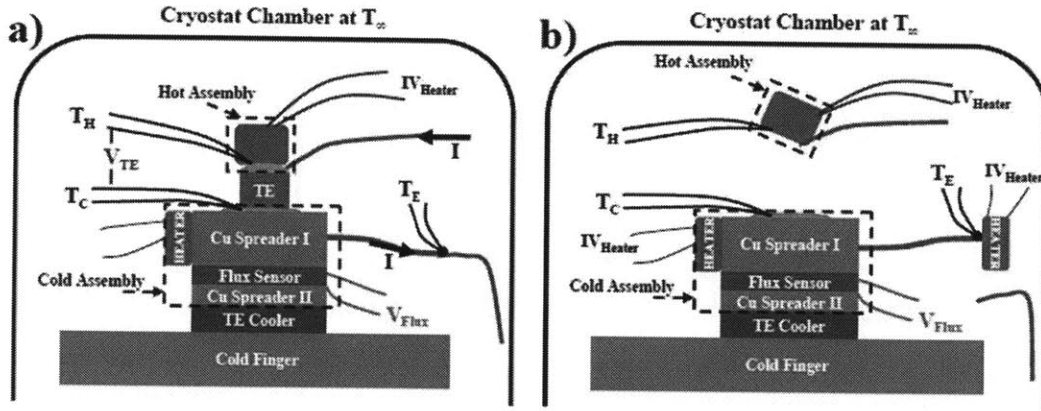


Figure 2-2: A schematic diagram of the a) property and efficiency measurement system b) calibration procedure for the hot side heater and the cold side heat flux sensor.

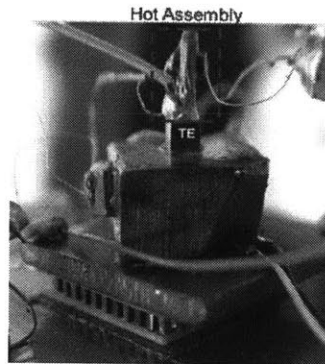


Figure 2-3: Photograph the experimental system with a TE leg under test.

In our calibration it was found that heat losses from the hot assembly constituted about 10 % of Q_H . At the cold assembly heat conduction loss was dominant to Joule heating gains in the electrodes, and the combined correction value constituted <3 % of Q_C . We performed an energy balance over the leg such that $Q_{rad,side} = Q_{H,OC} - Q_{C,OC}$ with $\Delta T = 75$ °C and solved for the emissivity. The obtained emissivity of $\varepsilon = 0.6$ agrees reasonably with Fourier Transform Infrared Spectroscopy measurements from similar samples and in addition is evidence that the heater and flux sensor have been accurately calibrated.

2.4. Property Data Analysis

The procedure for the properties measurement is to set a constant heater power, wait for the system to reach steady state, and then measure V_S , $Q_{H,OC}$ and R from section II-B. Then the heater power is reset and the properties are measured again for different values of T_H and T_C . Although it is possible to control the cooler module for each successive heater power setting to keep T_C constant, this increases steady state settling times considerably and adds unnecessary complexity. Due to temperature drifts in the system, $Q_{C,OC}$ had larger uncertainties than $Q_{H,OC}$ for small temperature differences where $Q_{C,OC} < 0.1 \text{ W}$. Therefore, during the properties measurement, in order to capture the entire temperature range from ΔT of 2 °C to 160 °C, we use $Q_{H,OC}$ instead of $Q_{C,OC}$ and allow T_C to rise with increasing T_H (figure 2-4).

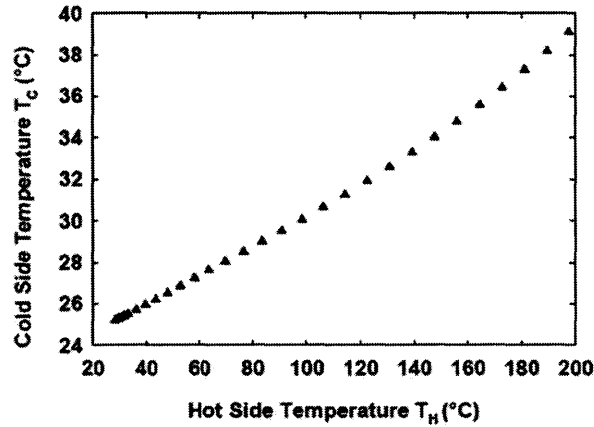


Figure 2-4: Cold side temperature vs. hot side temperature during the device properties measurement.

Based on the integral relationship between the intrinsic properties and the device properties, the intrinsic properties can be solved for by regression fitting or taking the numerical derivative of the device properties. We found that the latter method was more accurate. The process can be understood by considering an arbitrarily measured device property $Y(T_H, T_C)$ and an intrinsic property $y(T)$ related by

$$Y(T_H, T_C) = \int_{T_C}^{T_H} y(T) dT = f(T_H) - f(T_C), \quad (2.15)$$

where $\partial f(T)/\partial T = y(T)$. We take the derivative with respect to T_H ,

$$\frac{dY(T_H, T_C)}{dT_H} = \frac{df(T_H)}{dT_H} - \left. \frac{\partial f(T_C)}{\partial T_C} \right|_{T_H} \frac{dT_C}{dT_H} = y(T_H) - y(T_C) \frac{dT_C}{dT_H}, \quad (2.16)$$

and evaluate the derivatives numerically. Taking the centered difference, we solve for the arbitrary property as a function of temperature

$$y(\bar{T}_H) = \frac{\Delta Y}{\Delta T_H} + y(\bar{T}_C) \frac{\Delta T_C}{\Delta T_H}, \quad (2.17)$$

where $\bar{T}_H = (T_{H,2} + T_{H,1})/2$ is the mean temperature of two consecutive measurements. We observe from figure 2-4 that $\Delta T_C/\Delta T_H \approx 0.08$ so it is important to evaluate the properties accurately in the low temperature range because they will also affect the higher temperature range. A linear regression fit was applied to the first few measurement points in the lower temperature range.

2.5. Property Results

Each of the intrinsic properties was evaluated by taking the numerical derivative of the device properties following the procedures described in the Property Data Analysis section. Figure 2-5 (a-d) plot $S(T)$, $\rho(T)$, $k(T)$, and $Z\bar{T}(T)$ as well as their respective effective properties as a function of T_H . The measured effective properties are plotted as discrete points with error bars while the intrinsic properties have been plotted as linearly interpolated curves. The uncertainty was estimated individually for each effective property point. The maximum uncertainty values for S_{eff} , k_{eff} , ρ_{eff} are approximately 0.7 %, 0.9 %, and 0.4 %, respectively.

Figure 2-5(d) shows that $Z\bar{T}$ drops off with increasing temperature more rapidly than $Z\bar{T}_{eff}$ due to the integral relationship between the intrinsic and effective properties. This graph

can be used by the design engineer to quickly determine the performance of a TE generator made with this leg. For instance, given $T_H = 198\text{ }^\circ\text{C}$ and $T_C = 39\text{ }^\circ\text{C}$ (figure 2-4), the leg should operate as a $Z\bar{T}_{eff} = 0.64$ material. To verify that the intrinsic property curves have been differentiated correctly we used the intrinsic properties to solve for $Z\bar{T}_{eff}$ at the same measured temperature points as in figure 2-5(d) and found the relative difference to be 0.2 %.

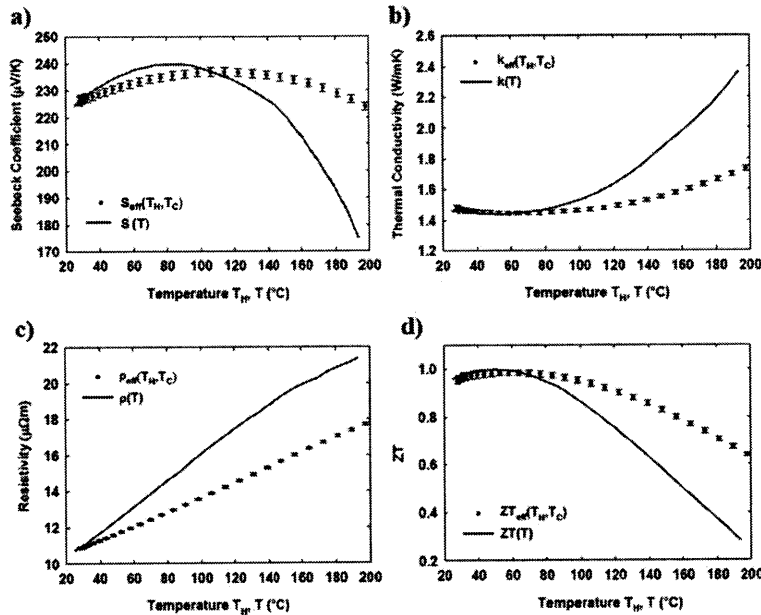


Figure 2-5: The four intrinsic TE properties versus temperature and their respective effective properties versus hot side temperature: a) Seebeck coefficient, b) thermal conductivity, c) electrical resistivity, d) dimensionless thermoelectric figure of merit.

2.6. Efficiency Results

The goal of the efficiency measurement is to firmly establish what performance can be expected from the particular leg and to compare these results to the calculated power and efficiency from the intrinsic properties measurement. The procedure was to apply a constant heater power and current, measure the steady state Q_C , P_e , and then repeat for another current setting. The efficiency was measured at two different temperature ranges; the estimated uncertainty was less than 0.6 %.

Figure 2-6 plots the maximum efficiency versus ΔT for $T_C = 24.5\text{ }^\circ\text{C}$. The solid curve is the calculated value from the intrinsic property data using Eq.(2.9), the dotted curve is using

Eq.(2.1) with the calculated $Z\bar{T}_{eff}$ from Eq.(2.14) and the discrete points are measured values. Equations (2.1) and (2.9) show excellent agreement for $\Delta T < 120$ °C, which confirms that it is appropriate to characterize a material by $Z\bar{T}_{eff}$. The small divergence at high ΔT reflects that $S(T)$ drops rapidly at high temperature and the assumption $S(T_H) \approx S(T_C) = S_{eff}$ (Eq.(2.14)), is not well satisfied.

Figure 2-7(a-b) plots the measured and calculated efficiency Eq.(2.9) versus current at two hot side temperature settings. The calculated and measured powers are in excellent agreement for both cases with a relative difference of < 0.4 % for all measured points. The relative difference of measured to calculated efficiency in figure 2-6(a) is 0.5–2.0 % while that for figure 2-7(b) is 0.1–0.3 %. The larger relative difference of efficiency in figure 2-7(a) is likely an indication of the larger uncertainty in Q_C at small heat transfers rates. Recall that $Q_{H,OC}$ and Q_C are independently measured quantities with independent calibrations. The property measurement uses $Q_{H,OC}$ and the efficiency measurement uses Q_C . Therefore, the fact that the measured power and efficiency are in excellent agreement with each other is convincing evidence that both have been measured accurately. This independent check feature is an important advantage of the described technique.

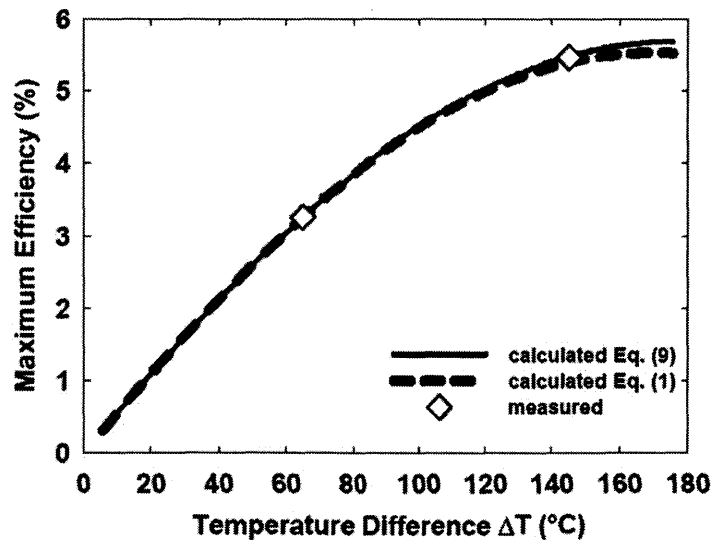


Figure 2-6: Maximum efficiency versus temperature difference across the leg for a cold side temperature of 24.5 °C.

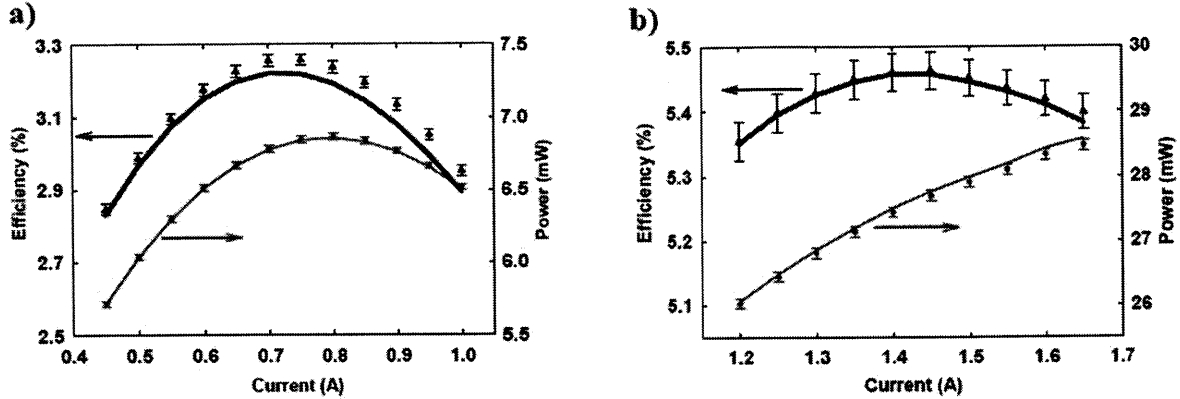


Figure 2-7: Efficiency and power versus current, the points with error bars are the measured values, the lines are calculated from the measured properties using Eq.(2.9) and Eq.(2.10). a) Hot side temperature is 86–93 °C, cold side is 24–25 °C. b) Hot side temperature is 169–172 °C.

2.7. Conclusions

In this work, we employed an effective property approach to model a single thermoelectric leg for power generation. We apply a one-dimensional model considering temperature-dependent material properties and side wall radiation loss. Using effective properties, we are able to write approximate solutions for the power and efficiency which are mathematically similar to the well-known constant property formulas. If the Seebeck coefficient varies strongly over the operating temperatures, the Thomson heat should be included in the efficiency calculation for most accurate results.

We developed an experimental technique capable of directly measuring an energy balance over a single leg, with a large temperature difference ranging from 2 °C to 160 °C. The technique measures all three TE properties of a single leg, in the same direction, with significantly less uncertainty than other methods. The measurements include the effects of temperature dependent properties, side wall radiation, and contact resistance. Side wall radiation loss constituted < 2 % of the hot side heat transfer rate, but it is still a significant part of the energy balance considering that the power conversion efficiency was 2.8-5.5 %. The power and efficiency were directly measured and are within 0.4 % and 2 % of the values calculated based on the property measurements.

Chapter 3. Skutterudite Unicouple Fabrication

This chapter will describe the fabrication of a high ZT skutterudite unicouple using novel electrode materials. Skutterudites are mid-temperature thermoelectric materials that can operate up to 500-600°C. They have relatively high ZTs and good thermomechanical properties. They are a well-studied class of thermoelectric material that is of interest to many research groups.^{24,26,45-51} Naturally, the motivation for this material is for power generation at higher temperatures such as vehicle waste heat recovery, solar thermal, and remote power applications.

The chapter begins by describing the motivation for device measurements and method for fabricating device samples by bonding electrode to the skutterudites. The next section will identify and evaluate electrode materials based on the following criteria: thermal stress, parasitic electrical/thermal resistance, chemical stability and ease of prototype fabrication. There were many challenges during press to produce device samples with good properties, without cracks. We describe the original direct hot press process and how it was necessary to redesign it into what we call a hybrid hot press. In chapter 4 we describe the experimental device testing system including the instrumentation and methodology to measure the effective properties and conversion efficiency with high accuracy.

3.1.1 Individual Property Measurement Results

Our collaborators in Dr. Ren's group at BC have been steadily improving the ZT and repeatability of our skutterudite materials over several years. The device testing phase began in early fall 2009 and continued through spring 2010, over which time the skutterudites continued to evolve in terms of composition and processing. At the beginning of device testing both N-type and P-type were prepared from the elemental ball mill (BM) method, however the final samples were prepared by the melt method (see chapter one). The N-type composition was fixed at $\text{Yb}_{0.35}\text{Co}_4\text{Sb}_{12}$ while different P-type compositions were explored throughout device testing. The composition of the P-type device samples measured in this chapter was $\text{NdFe}_{3.5}\text{Co}_{0.5}\text{Sb}_{12}$. For more information on the chemistry of skutterudite materials refer to Yang's doctoral thesis.¹⁷

The thermoelectric properties were measured by Jian Yang using the commercial instruments described in chapter one. The expected N-type peak ZT is 1.2 at 550°C and the P-type is 0.8 at 550°C (figure 3-1 and figure 3-2). There is 5% uncertainty in Seebeck and electrical and 8% uncertainty in thermal conductivity, which results in a 14% uncertainty in ZT. In general the device measurements may differ from the individual property measurements due to instrument uncertainty and processing conditions. There is inherent variability between batches due to differences in composition, ball-mill time, and press temperature/time/pressure.

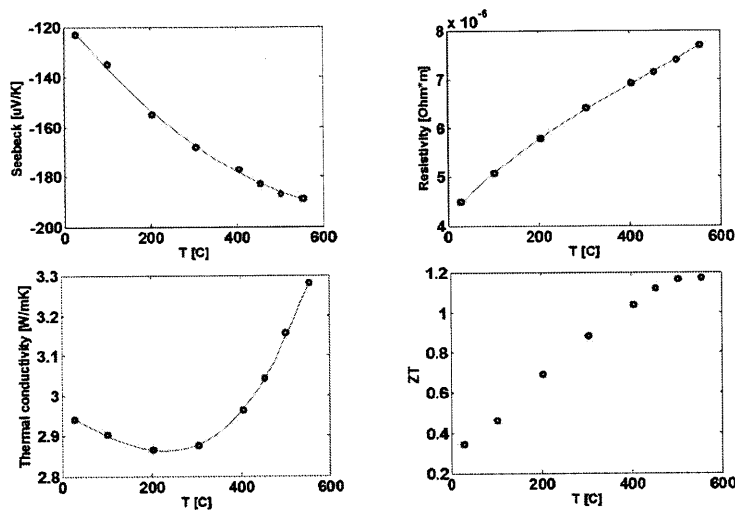


Figure 3-1: N-type properties measured by Jian Yang using the individual properties method described in chapter 1 (N-melt 2)

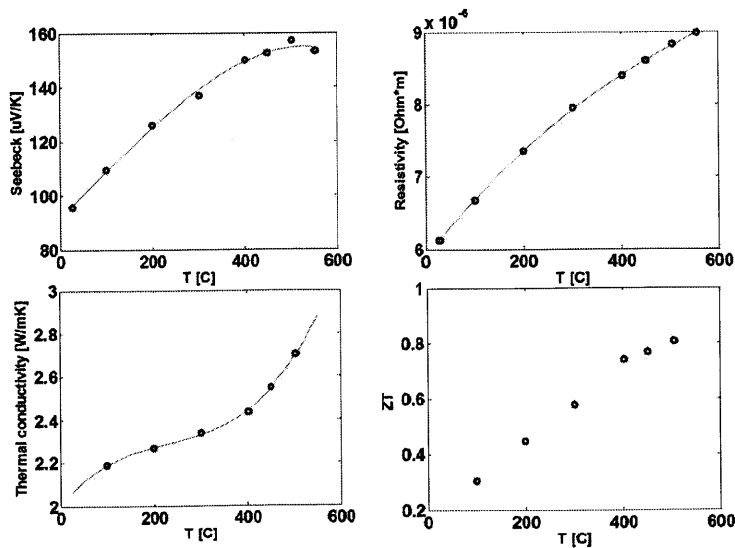


Figure 3-2: P-type properties measured by Jian Yang using the individual properties method described in chapter 1 (P-melt 12)

3.1.2 Compatible Electrode Materials

Module construction consists of alternating N-type and P-type legs connected electrically in series and thermally in parallel by electrodes (figure 3-3). In general there are two methods of connecting the electrodes 1) metallization and soldering/brazing 2) direct bonding during press.⁴⁵⁻⁴⁷

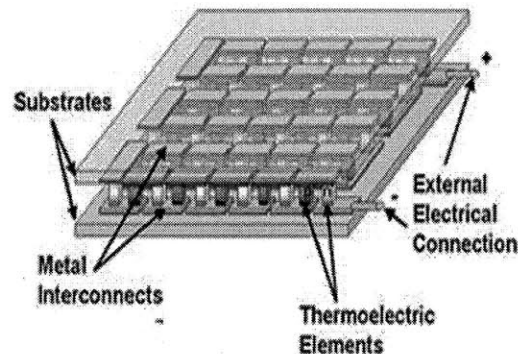


Figure 3-3: Traditional module design, electrodes are either soldered to the thermoelectric legs or bonded directly.*

The first method is used in commercial Bi_2Te_3 construction. The ends of the legs are plated with Ni and then copper electrodes are connected with a low melting point solder ($T_{\text{melt}} < 300^\circ\text{C}$). However, this method does not work well for skutterudites around 600°C for several reasons. There are few commonly used brazes available at this temperature range and it is likely that compromises would have to be made on the melting temperature and other properties. Another constraint is that the coefficient of thermal expansion (CTE) of the brazing materials must be well matched to the material. The metallization layer must be dense and thick enough to be an effective diffusion barrier with low electrical and thermal contact resistances. It was found early in the device testing phase that the Ni diffusion barrier would be a problem. On the left of figure 3-4 is an N-type leg with a sputtered Ni layer, on the right a leg from the same batch which has been wetted with solder and held at 450°C on a hot plate in air for 10 hours. Clearly the solder diffused into the leg and destroyed the material. Ni is known to substitute Co in the lattice, the Ni layer was probably too thin and unstable to prevent solder diffusion. Several

<http://www.medi-fridge.com/science.aspx>

metallization techniques were tried such as sputtering, e-beam deposition and electroplating; all produced a Ni layer $<1\mu\text{m}$ thick. For these reasons we concluded that Ni metallization showed little promise as an effective solution for device testing, let alone module fabrication in a real device and therefore this method was abandoned.

The second method, direct bonding, is the chosen solution for the rest of this work. Rigid electrodes are placed inside a graphite press along with the TE powder and pressed all in one step (figure 3-5). The TE powder sinters to itself and the electrodes, producing a bond with superior mechanical, electrical, and thermal contact. For instance the direct bonding method would never fail the “scotch tape test”^{*} which is used to evaluate the mechanical adhesive of the Ni plating. It will be shown that the direct bond method was successful during device testing and offers a practical solution for unicouple construction.

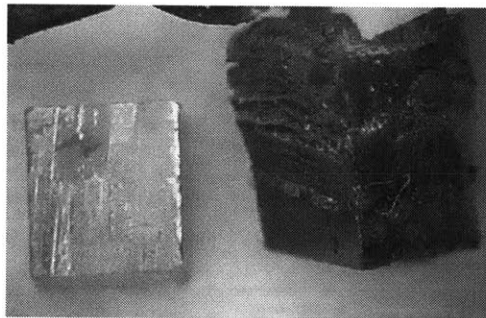


Figure 3-4: (left) N-type leg with Ni plating before test (right) N-type after wetting with Sn-Sb solder and left on a hot plate in air at 450°C of 10hrs. Catastrophic diffusion damage resulted.

^{*} Common test in which the adhesion of a metal film is evaluated by adhering scotch tape to the metallized surface and subsequently peeled off.

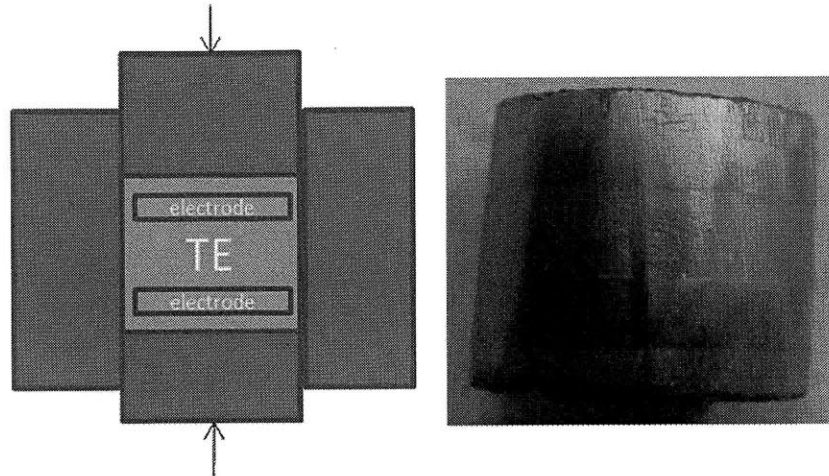


Figure 3-5: Direction bond method (left) includes rigid electrodes with thermoelectric powder during sintering phase. The result (right) is a robust bond with superior mechanical, electrical, and thermal properties.

3.2. Electrode Selection

Candidate electrode materials were identified and evaluated based on the following criteria:

- 1) Thermal expansion: the CTE (coefficient of thermal expansion) should be well matched between the electrode and skutterudite.
- 2) Transport properties: the electrode should have a high thermal/electrical conductivity relative to the skutterudite
- 3) Synthesis: we need to be able to synthesize the electrode by the methods and resources available.
- 4) Contact resistance: the bond should exhibit low electrical and thermal contact resistances.
- 5) Chemical stability: the bond should be chemically stable over the lifetime of a proposed device, on the order of 10 years.

The search for candidate electrodes began by comparing skutterudite CTE and transport properties to literature values of candidate electrode materials. We had an intuition to investigate silicides because the BC group had experience synthesizing these compounds in the past. The Co-Si family was good candidates based on what we knew of criteria 1,2,3,5 and CoSi_2 is widely used as a contact material in the integrated circuits industry and is well studied. After making a few device samples we found that criteria number four was satisfied and the total contact resistance was low. Our final electrode selections are CoSi_2 with the N-type and Co_2Si with the

P-type. These are unique electrode solutions as compared to Zhao *et al.* who used a Mo-Cu alloy with a Ti bonding layer.⁵²

3.2.1 Chemical Properties and Synthesis

Skutterudites are a Co based compound therefore from a simple chemical argument we expect Co-Si compounds to potentially bond well with skutterudites. The Co-Si phase diagram in figure 3-6 shows that CoSi_2 , CoSi , Co_2Si are eutectic alloys with melting temperatures above 1300°C . Therefore they are expected to be stable phases at the operating temperatures of the skutterudite device. The three phases are miscible so it should be possible to make a graded electrode that transitions from CoSi_2 to Co_2Si along the length, or a composite electrode to optimize a property such as CTE. The crystal structure of CoSi_2 is cubic and Co_2Si is orthorhombic. In general there will be mass diffusion at the electrode-TE interface and unwanted phases are likely to form. Therefore the electrode materials should not form low melting point compounds with elements of the skutterudites. The Sb-Si and Fe-Si systems form no compounds with melting points below the skutterudite operating temperature range (figure 3-7 and figure 3-8), thus we expect the interface to be chemically stable.

The electrode materials were made in-house with the DHP (direct hot press) method. CoSi_2 powder was procured from Alpha Aesar and pressed at 1200°C for 3 min at 84MPa (.35ton force). The measured density was 4.9 g/cm^3 compared to 4.9-4.95 from literature^{53,54} and it is clear by inspection with an optical microscope that there are macroscopic of voids spaces within the material. It has been suggested that adding trace amounts of Ni or B to the powder may help achieve full density*. The Co_2Si electrode was made by the melt method, ball-milled into a powder and pressed at 1100°C for 3 min at 70 MPa. The measured density of 7.1 g/cm^3 is in good agreement with the literature value of 7.1 ⁵¹ and has no macroscopic or microscopic voids. Both CoSi_2 and Co_2Si samples were then annealed at 1000°C for 10 hrs before being cut and polished into disks.

* Suggestions by Zhifeng Ren and Bo Yu

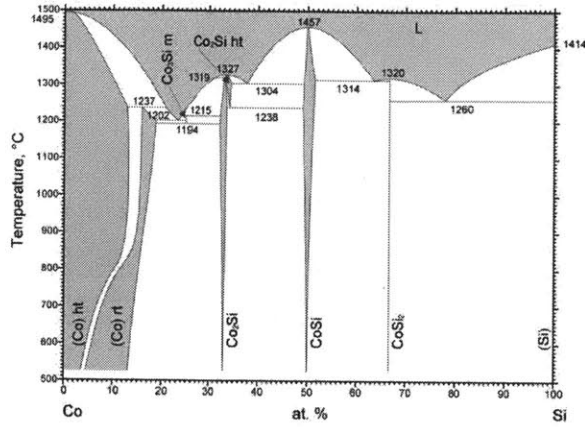


Figure 3-6: Co-Si phase diagram (source: ASM International 2009, Diagram No.101097)

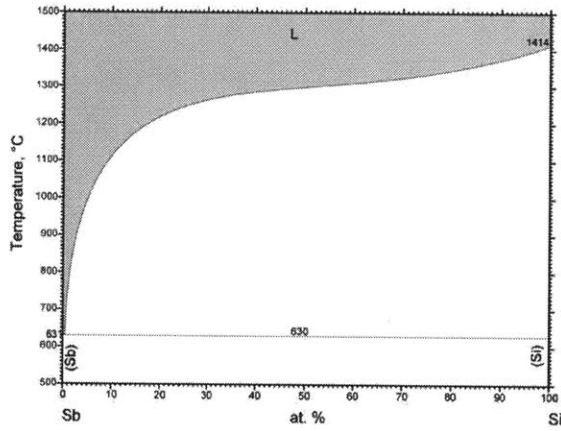


Figure 3-7: Sb-Si phase diagram (source: ASM International 2009, Diagram No.902064)

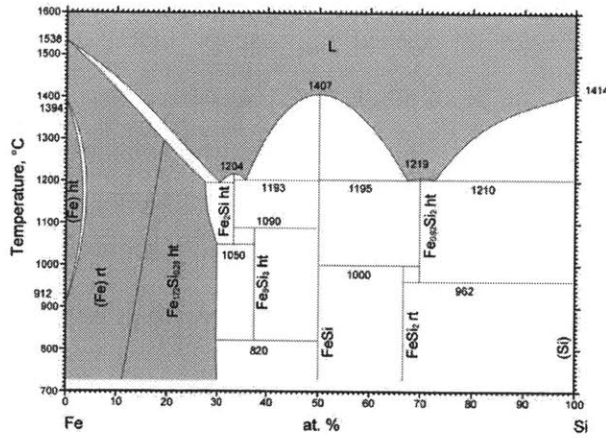


Figure 3-8: Fe-Si phase diagram (source: ASM International 2009, Diagram No.2002013)

3.2.2 Thermomechanical Properties

The most important constraint in selecting a compatible bonded electrode material is that the coefficient of thermal expansion (CTE) must be well matched to reduce thermal stress at the interface. The minimum stress state will be at the sintering temperature (T_{press}) when the bond is initially formed. As the sample cools the dissimilar materials will contract at different rates creating a shear stress at the interface. If the CTE is not close over the entire temperature range then the TE and electrode bond will fail and separate entirely. Thermoelectric devices must endure many thermal cycles throughout their lifetime. Another mode of failure is via fatigue stress which propagates cracks at the interface and can gradually increase electrical contact resistance over time, decreasing the effective ZT of the device.

Figure 3-9 plots the CTE versus temperature of the elemental BM (ball-milled) skutterudites. Each sample was measured twice in succession. Ball-milled samples were measured by collaborators at Bosch, and are within the expected literature values.^{22,49,55-59} In early 2010 we used this data as a basis for our decision of candidate electrode materials. Usually CTE values are given in table form as a constant value for a single material; however the actual CTE is often highly temperature dependent. Thermoelectric materials are characteristically brittle and weak and thus require a closely matched CTE over the entire temperature range. We first used CINDAS Thermophysical database⁶⁰ to identify candidate electrode materials based on CTE. It soon became evident that it is uncommon for materials to be well matched over a large temperature range and that just like thermoelectric properties CTE values are sensitive to material synthesis, microstructure, doping etc. Selecting electrode materials was an iterative process between searching the CINDAS database and other sources for CTE, comparing transport properties from literature and determining whether we could synthesize them. It was determined in early 2010 that the Co-Si system met all the criteria. Figure 3-9 shows that all materials exhibit a similar temperature dependence and CoSi_2 is nearly a perfect match for the N-type. By the end of 2010 our skutterudite materials were prepared by the melt method rather than the BM method. Melt method achieves denser samples, better homogeneity, less defects and overall better mechanical properties. The CTE of the melt samples were measured by

Netzsch testing services* and the results are compared to the BM samples in figure 3-10. The melt samples clearly show hysteresis between runs above 450°C which is evidence of annealing behavior. The phenomena needs more study but it is likely evidence of incomplete sintering.

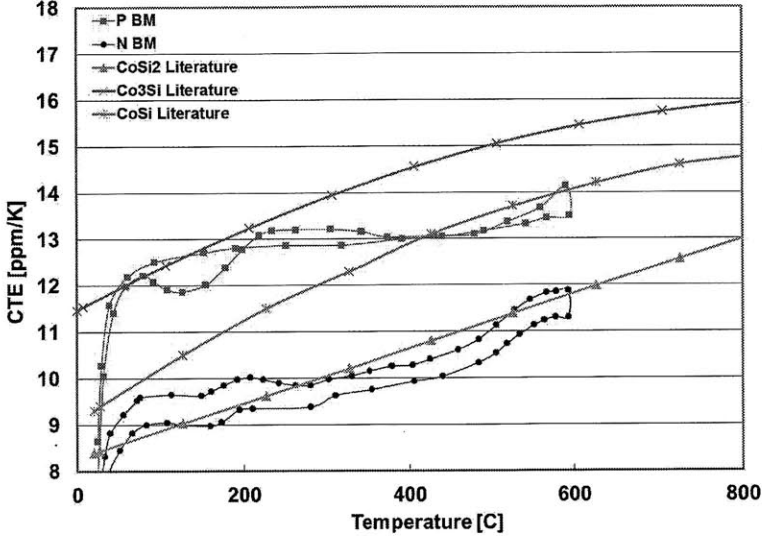


Figure 3-9: Coefficient of thermal expansion for N and P ball-mill (BM) samples, and literature values of candidate electrode materials.⁶⁰ These results were the basis of our decision to try CoSi₂ and Co₂Si as electrodes. BM samples were measured by collaborators at Bosch.

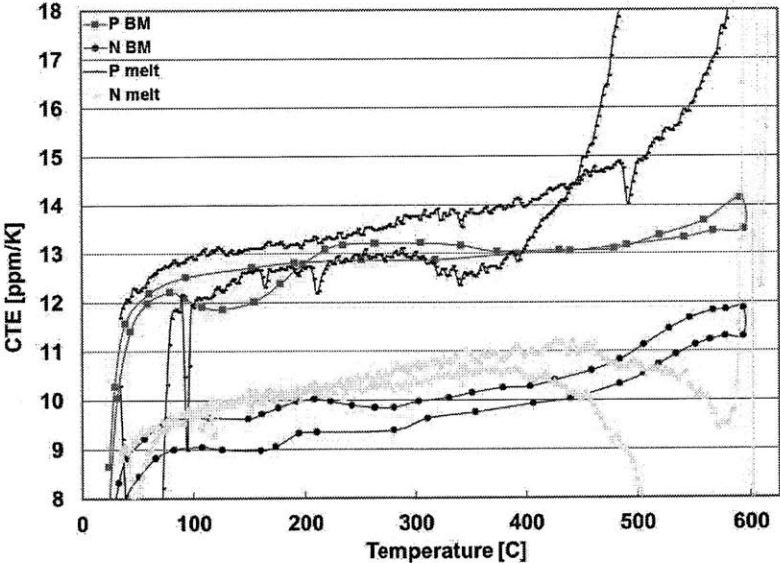


Figure 3-10: Coefficient of thermal expansion for N and P ball-mill (BM) samples compared to the N and P melt samples. The hysteresis of the melt samples is probably due to incomplete sintering and/or lack of

* Netzsch CTE measurements were performed on a dilatometer

annealing. BM samples were measured by collaborators at Bosch. Melt samples were measured by Netzsch testing service.

Both CoSi_2 and Co_2Si electrode materials were synthesized by the DHP (direct hot press) and annealed at 1000°C for 10 hrs before being cut up and polished into disks. Annealing was performed to minimize residual stress and to reduce uncertainty in the actual CTE value. Figure 3-11 plots the CTE values of the annealed and unannealed electrodes as well as the literature values.⁶⁰ In each case the electrodes exhibit a higher CTE after annealing. It is unknown how much of this difference is physical versus experimental error. The uncertainty in the CTE measurements is 2-4% at high temperatures but it is much larger near room temperature.* There is a relatively large difference between the measured CTE of CoSi_2 and the literature value, the divergence may be related to its low density and is an issue that deserves further study. Although we don't have a literature prediction of Co_2Si CTE one might expect it to lie between Co_3Si and CoSi but again the measured value is much higher than this prediction. Figure 3-12 plots the CTE data of all the materials used in the device samples, these are our actual properties to the best of our knowledge.

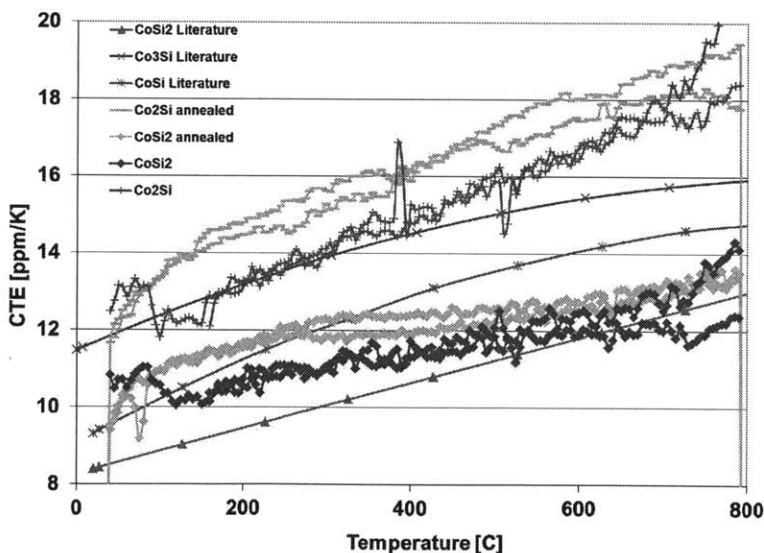


Figure 3-11: Coefficient of thermal expansion of our measured electrodes (measured by Netzsch) compared to literature values.⁶⁰ The disagreement between the measured and literature warrants further investigation.

* High uncertainty of CTE near room temperature is due to unsteady heating which is a characteristic of the dilatometer used by Netzsch testing services.

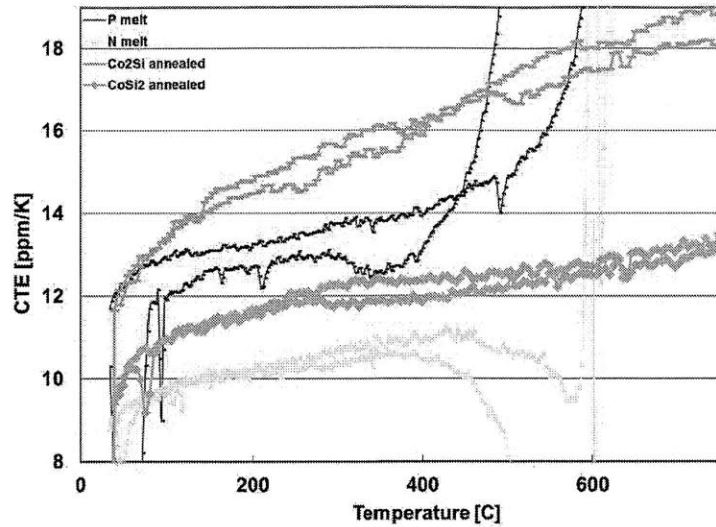


Figure 3-12: Measured Coefficient of thermal expansion of the final electrodes and skutterudites used in device testing. (measured by Netzsch)

The ultimate tensile strength (Weibull Strength) and modulus of elasticity (E) of the BM samples were measured at room temperature by our collaborators at Bosch (Table 3-1). The N-type has a much lower modulus and tensile strength than reported in literature⁵⁸, which is probably due to the large number of defects and inhomogeneity of the BM samples. The mechanical properties of the melt samples have not yet been tested, but they are expected to be superior to the BM samples and be closer to literature. In general it is possible to improve the mechanical properties of skutterudites by composition and processing changes, just like any other property.

Table 3-1: Mechanical properties of skutterudites, the last column is from⁵⁸.

		n-type	p-type	n-type [ref]
Weibull Strength	[MPa]	61	112	123
E-modulus	[GPa]	108	154	135
G-modulus	[GPa]	44	63	
ν	[-]	0.23	0.23	
density	[g/cm ³]	7.38	7.57	

3.2.3 Transport Properties

Ideally the electrodes should have a high electrical and thermal conductivity relative to the skutterudite such that parasitic electrical and thermal resistances can be neglected. The annealed electrodes transport properties were measured by Jian Yang at BC by the same methods

as used for the skutterudites. The Seebeck of CoSi_2 is close to zero while the Co_2Si is near $-10 \mu\text{V}/\text{K}$ (figure 3-13). The electrical resistivity and thermal conductivity is given in figure 3-14 and figure 3-15. CoSi_2 is a very good electrode with an average thermal conductivity about 14x higher and an average electrical resistivity about 14x lower than the N-type. The Co_2Si electrode is fair, with an average thermal conductivity about 5x higher and an average electrical resistivity about 5x lower than the P-type. The final device samples had a TE length of about 4 mm and the thermocouples were positioned about 0.3 mm from each interface (Table 4). Therefore the bulk parasitic electrode thermal/ electrical resistances were about 1% for the N-type and 3% for the P-type. The parasitic resistances may be able to be further decreased in a real module by optimizing the geometry and bulk properties of the electrodes.

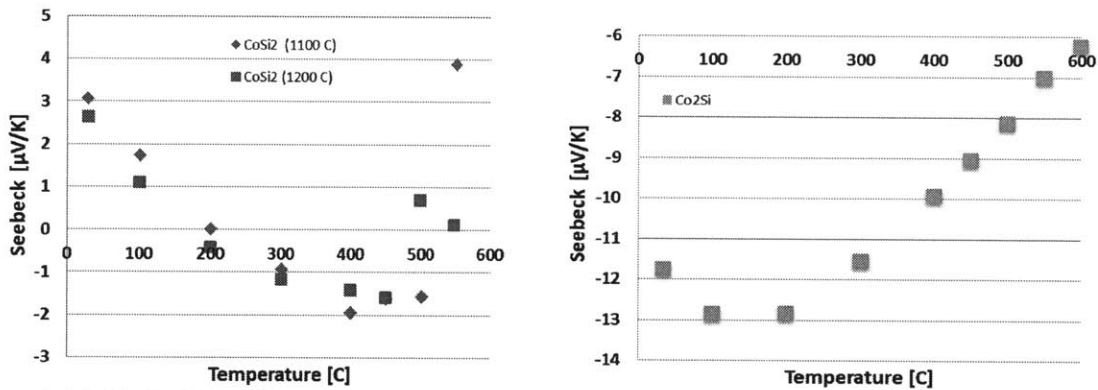


Figure 3-13: Seebeck coefficient of annealed electrode materials. (left) CoSi_2 used with the N-type (right) Co_2Si used with the P-type. (measured by Jian Yang)

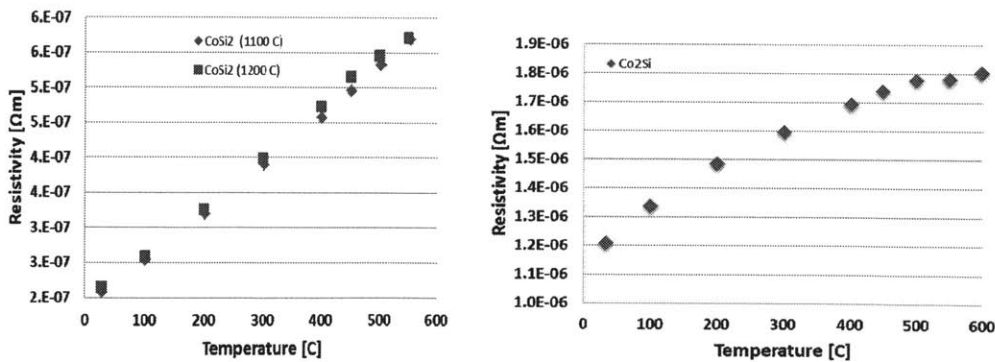


Figure 3-14: Electrical Resistivity of annealed electrode materials. (left) CoSi_2 used with the N-type (right) Co_2Si used with the P-type. (measured by Jian Yang)

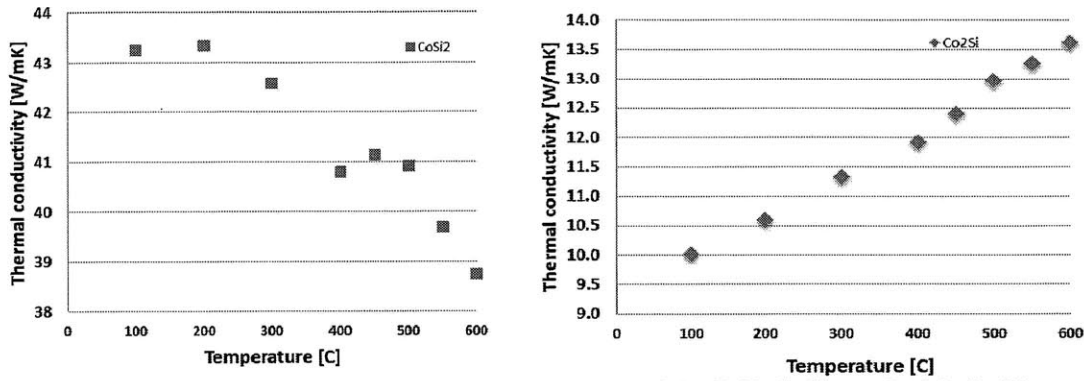


Figure 3-15: Thermal conductivity of annealed electrode materials. (left) CoSi₂ used with the N-type (right) Co₂Si used with the P-type. (measured by Jian Yang)

3.3. Device Sample Fabrication

This section will explain the optimized pressing conditions of the device samples i.e. electrodes bonded to skutterudites. The pressing conditions of the device samples were based off the original press conditions of the skutterudite developed by our collaborators at BC. The DHP (direct hot press) method is a rapid, scalable fabrication technology for thermoelectric nanocomposites. However there are some subtle and important details of its operation that needed to be understood to successfully fabricate device samples. A major challenge was to optimize the press conditions to produce device samples with good electrical properties that were free of cracks. The final solution was to modify the direct hot press and transform it into a hybrid hot press (HHP) in order to achieve a more uniform sinter temperature and repeatable process.

3.3.1 Original Pressing Conditions

The skutterudite phase diagram is shown in figure 3-16.⁶¹ There are three stable compounds formed in the higher pnictogen range: CoSb(γ phase), which is a metal, and two other semiconductors CoSb₂(δ phase) and CoSb₃(ϵ phase). There are two important reactions involving CoSb₃ which put upper limits to the maximum pressing temperature and operating temperature. The reaction, $\delta - phase + Liq \rightarrow \epsilon - phase$ occurs at $T_{press} = 873^{\circ}C$ and should be avoided during press so that the sample doesn't melt. The reaction, $\epsilon - phase + Liq \rightarrow \epsilon - phase + Sb$ occurs at $T_{press} = 621^{\circ}C$ and is an upper limit to the operating

temperature of the material because this will lead to high rates of Sb loss via sublimation at the surface.

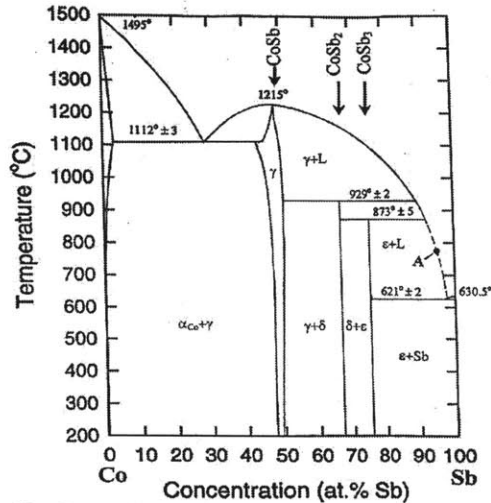


Figure 3-16: Co-Sb phase diagram used to guide the synthesis of CoSb.¹⁷

Figure 3-17 is a schematic of the original pressing conditions of the skutterudite materials. The important parameters during press for a given powder preparation are temperature, pressure and time. Increasing the pressure results in a denser sample and higher power factor. However, at some point the power factor versus pressure relationship plateaus. Nearly all samples are pressed at a standard pressure of 67 MPa (Force=1ton, dia.=1/2”) which produces a high power factor with a low risk of breaking the graphite dye during press. The samples must be cooled slowly and uniformly to prevent thermal stress induced cracks. After the completion of sintering, the graphite die is immediately removed from the press at high temperature and placed on a brick with insulation covering all surfaces to cool slowly in air.

A lower T_{press} should result in smaller grains and lower thermal conductivity, while a higher T_{press} results in more complete sintering, higher density and a higher power factor. Yang studied the N-type properties at T_{press} equal to 650,700,750°C for 5 min (figure 3-18).¹⁷ The 750°C sample has the highest ZT, however the results are within about 15%. Yang studied the effects of a two-step process where the samples were first held at 600°C for 3 min and then at 700°C for 5 min and also investigated the effects of a post anneal step at 650°C for 2 hrs. Figure 3-18 shows a slight difference between the one-step and two-step process but they converge to the same value after annealing. The conclusion from Yang’s work is that the combination of optimizing press temperature and anneal time can increase ZT by 15%.

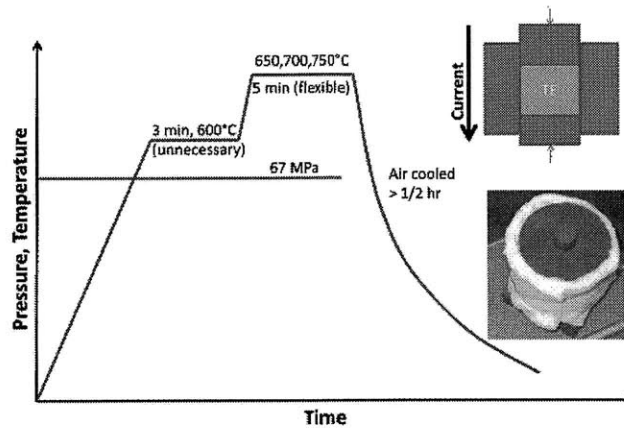


Figure 3-17: Pressure/temperature versus time for the original direct hot press (DHP) process for producing N and P skutterudites.

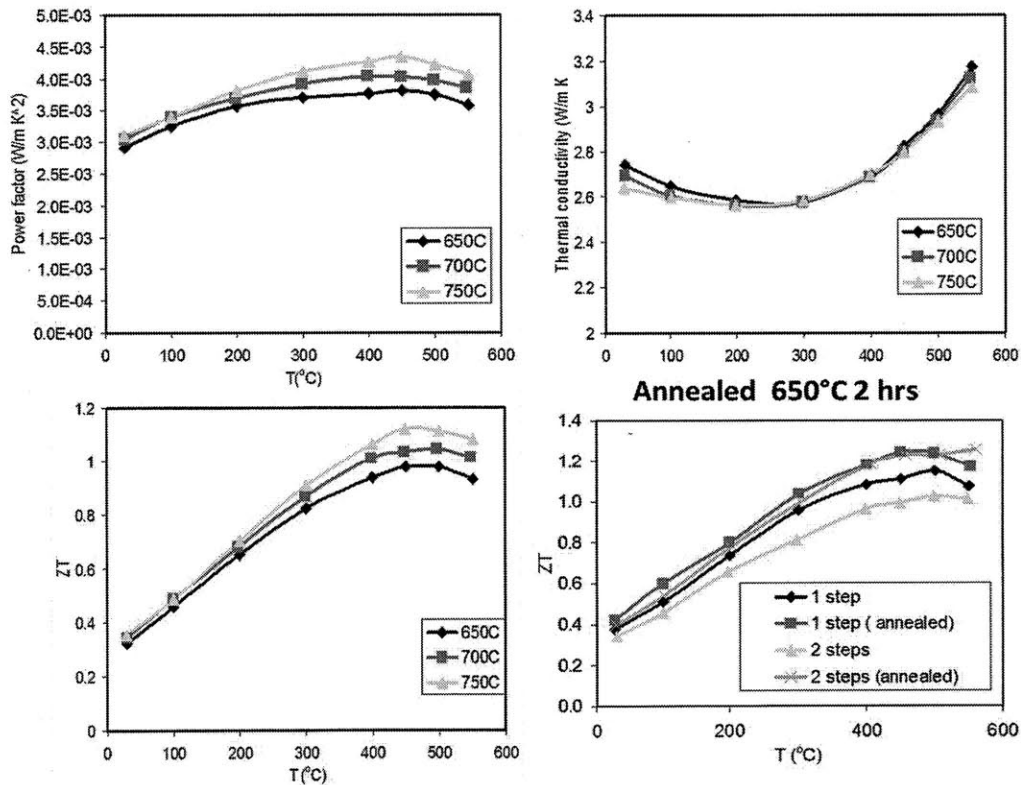


Figure 3-18: N-type skutterudite individual properties measured by Jian Yang.¹⁷ (upper left) Power factor at three different press temperatures (upper right) thermal conductivity at three different press temperatures (lower left) ZT at three different press temperatures (lower right) ZT from a 1-step and 2-step method with or without annealing. Optimizing the press conditions can enhance ZT on the order of 15%.

3.3.2 DHP Device Samples

The major difference between the device samples and the original skutterudite samples are the presence of a rigid electrodes. Early efforts produced many cracks in the samples with an occasional sample surviving the cutting stage to enable device testing. Cracks resulted in nearly every sample such as the July 2010 sample in figure 3-19 and it was unclear whether this was an inherent thermal mismatch problem or a pressing condition that could be changed. It was observed that the crack never occurred at the TE-electrode interface which suggested that the CTE is matched well enough and this problem could be solved without abandoning the bonded electrode technique. Based on the fracture patterns it was evident that the electrode was failing by bending stress and then these fractures would propagate into the electrode along the plane of maximum thermomechanical stress. The electrodes are loaded in compression by the graphite plunger on one side and the TE powder on the other. The plunger-electrode interface is not perfectly parallel and caused point loads while on the other side the TE powder does not distribute the load evenly at low temperatures. The uneven load distribution on both sides leads to large bending stress that would fracture the electrodes. Eventually we developed a few techniques to prevent electrode fracture:

- 1) Electrodes were annealed prior to device press to minimize residual stress.
- 2) TE powder was used in between the electrode and plunger contact to distribute load.
- 3) Diameter of electrode was reduced by a grinding method to ensure it was not being loaded radially by the graphite die.
- 4) Thicker electrodes were used which could be polished down later.
- 5) High pressure was not applied until greater than 500°C when the powder becomes soft, and compliant, and therefore capable of evenly distributing the compressive load.

The new pressing conditions are given in figure 3-20, the two-step process was used for the P-type while a one-step process was used for the N-type. Figure 3-19 shows how the P-type progressed from having many visible cracks to no visible cracks. Upon cutting the Feb. 2011 P-type it broke along the mid-plane of the skutterudite similar to the fracture pattern of the Jan. 2011 sample in figure 3-21. This fracture pattern was puzzling because CTE mismatch thermal stress is maximum at the interface and minimum at the mid-plane. Thermal stress along this plane could have only resulted from large temperature gradients in the sample during press.

Under the hypothesis that Joule heating was causing the large temperature gradient an N-type device sample was pressed in which the plungers were electrically insulated with Boron Nitride spray such that the current would by-pass the sample (figure 3-21). However, the sample still cracked along the mid-plane during polishing. At this point it was clear that the pressing method needed to be dramatically altered and we would first need to better understand the DHP process. The next section will explain how the DHP was modified to solve this problem. Lastly it should be noted that although many cracks were common, this method did produce a few usable samples for device testing and cracked samples were still used for interface studies (see Accelerated Aging Tests).

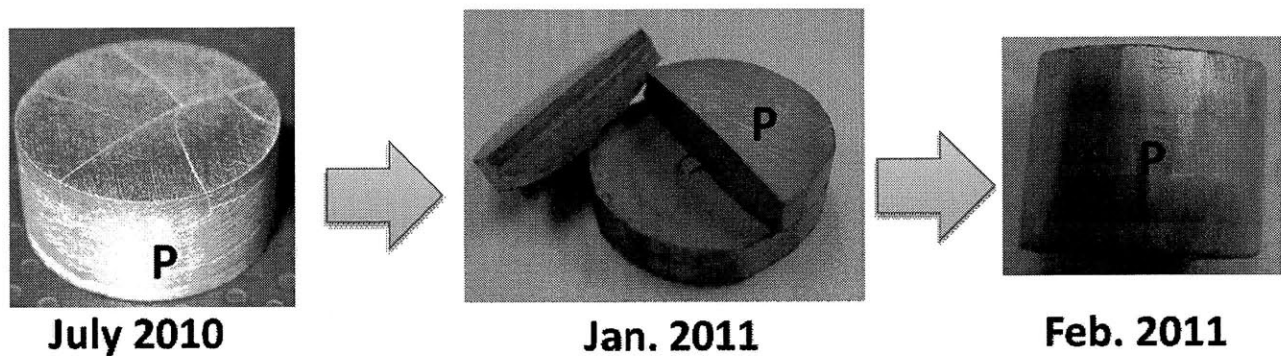


Figure 3-19: Evolution of the P-type device sample. The pressing conditions were changed to produce progressively fewer cracks in the sample.

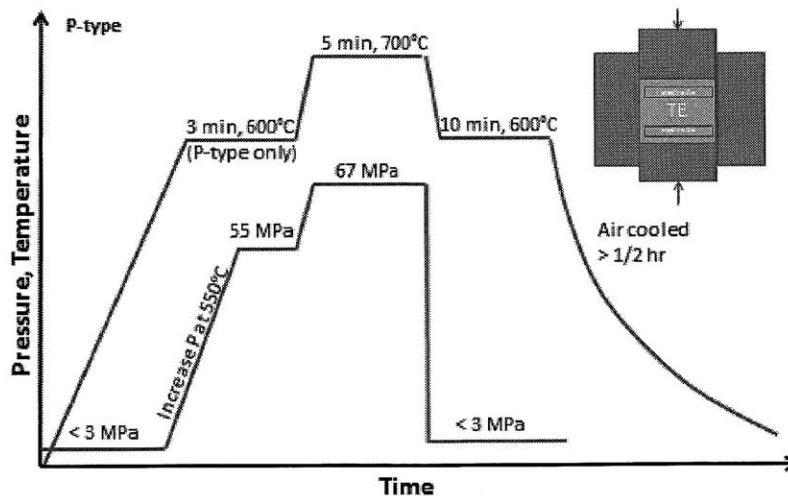


Figure 3-20: Direct hot press (DHP) pressing conditions for the P-type device samples.

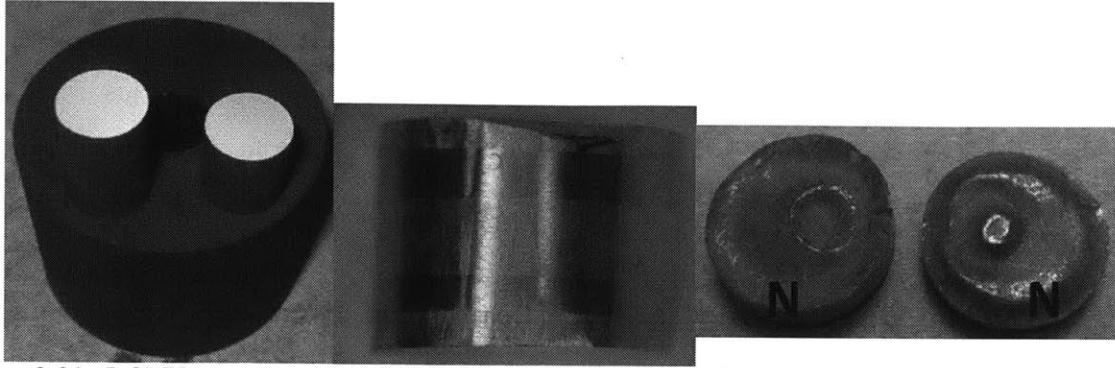


Figure 3-21: (left) Plungers were insulated with boron nitride in order to eliminate joule heating within the sample during press (middle) resulting N-type with no visible cracks. (right) N-type broke along the mid-plane after subsequent polishing.

3.3.3 Direct Hot Press vs. Hybrid Hot Press

This section explains how the original DHP process was modified and converted into a custom system that we name the hybrid hot press (HHP). The objective was to produce device samples without cracks along the mid-plane. The diameter of the sample and plunger was reduced from 1/2" to 1/4" and has electrically and thermally insulating plugs on the top and bottom of the sample so that current no longer flows through the sample (figure 3-22). The purpose of the insulator plugs are to create a more uniform temperature within the sample and to provide greater repeatability. A finite element (FE) model was developed in COMSOL Multiphysics to better understand the DHP process and guide the design of the HHP.

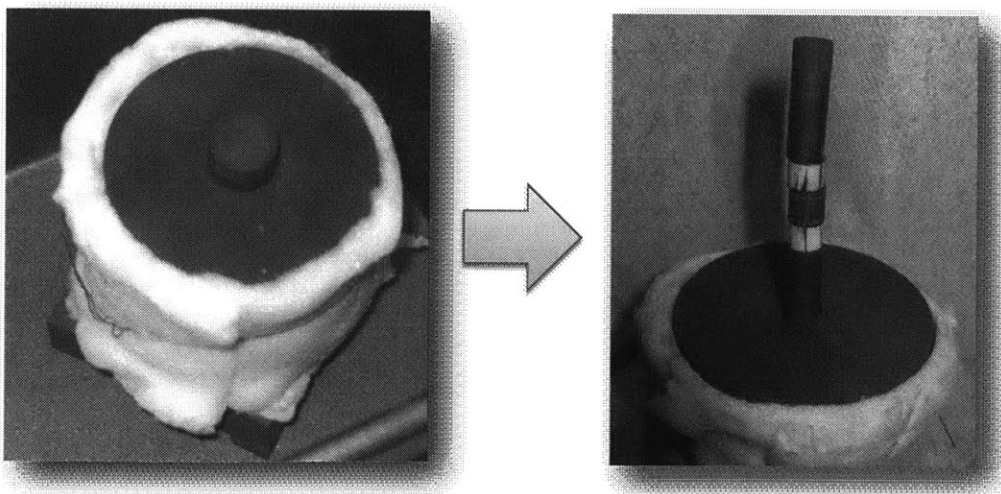


Figure 3-22: (left) direct hot press die (right) the new hybrid hot press die.

3.3.3.1 Direct Hot Press Model

The DHP process was studied using a FE model in COMSOL Multiphysics. The model included 2D steady state heat transfer and joule heating in solids with thermal radiation and electrical/thermal contact resistance. Temperature dependent graphite properties were used while constant properties were used for the TE, fiberglass insulation and insulator plug. This section will describe the DHP model, results, and model validation experiments. Figure 3-23 shows that the geometry and mesh is symmetric along the vertical axis of the die. There are current/heat spreaders on the top and bottom of the die, which in the real system are cooled by water blocks. The top and bottom most horizontal boundaries are held at a constant 50°C and current is injected uniformly. The die is wrapped in fiber glass insulation, all exposed vertical faces were modeled with black body radiation to the environment and air convection at 30 W/m²K. In the DHP model the graphite plunger extends from the spreader to the sample while in the HHP model there is an insulator material in between. Temperature is always monitored from the T_{die} thermocouple, during the verification experiments a second T_{plunger} thermocouple was installed. Specific geometries and current conditions for the DHP are given in Table 3-2.

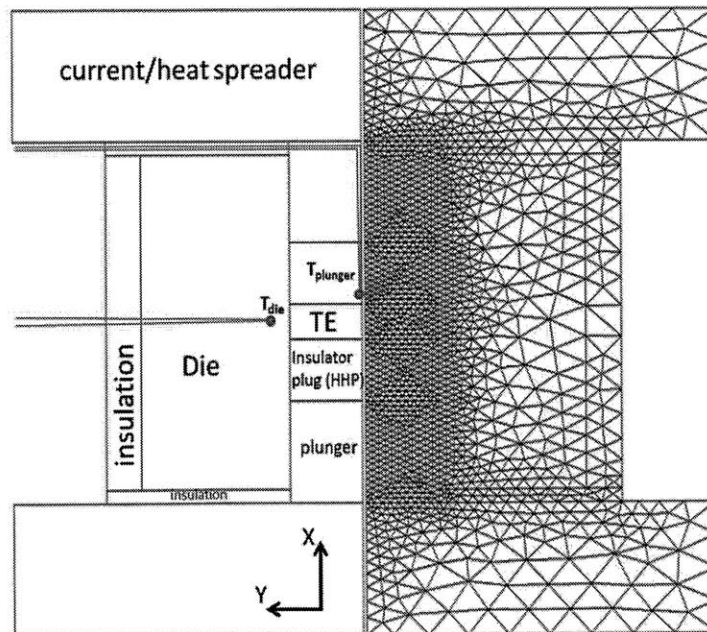


Figure 3-23: Geometry and mesh used in the finite element model. Note the position of the thermocouples measuring T_{die} and T_{plunger}.

Table 3-2: Geometric parameters and current setting of the direct hot press (DHP) and hybrid hot press (HHP) model.

	DHP	HHP
I [A]	540	310
R sample [mm]	6.35	3.175
H sample [mm]	9	10
H insulator [mm]	NA	7
H die [mm]	38	50.8
R die [mm]	30	30
t fiberglass [mm]	3	3
t gap [mm]	1.5	1.5

Electrical and thermal contact resistances are critical parameters which affect the temperature field in the die. Zhang measured the electrical and thermal contact resistances for a similar SPS (spark plasma sintering) process with graphite dies.⁶² Zhang's values were changed by a factor of <2 as needed to fit the validation experiments. The electrical and thermal resistance values are given in Table 3-3.

Table 3-3: Electrical (ρ) and thermal (h) contact resistances. Subscripts represent a graphite-graphite or graphite-TE contact, in the radial or axial direction. L_{graphite} is the equivalent length of graphite using nominal values of $\rho = 10\text{-}5\Omega\text{m}$, and $k=100\text{ W/mK}$. Zhang is from [62] and Muto is from this work.

	Zhang[7]	Muto	L_{graphite} [mm]
$\rho_{g,\text{axial}}$ [Ωm^2]	1.33×10^{-7}	1.33×10^{-7}	13.6
$\rho_{g,\text{radial}}$ [Ωm^2]	1.33×10^{-7}	1.33×10^{-7}	13.6
$h_{g,\text{axial}}$ [$\text{W/m}^2\text{K}$]	2.2×10^3	1.3×10^3	75.8
$h_{g,\text{radial}}$ [$\text{W/m}^2\text{K}$]	1.32×10^3	1.1×10^3	91
$h_{\text{TE},\text{radial}}$ [$\text{W/m}^2\text{K}$]		2.6×10^3	38

After running the model under a variety of configurations a few conclusions can be made about its general operation. Figure 3-24 shows that nearly all Joule heating occurs at the narrow constriction of the plunger, between the spreader and die. This calculated result is consistent with visual observations that this section always glows brighter—indicating higher temperature—than other sections. The heat generated in the plunger conducts along the axial direction and radially into the die. The thermal resistance between the plunger and die is important because this will determine the temperature difference between the two sections. The

graphite-graphite electrical contact resistance in the radial direction $\rho_{g,\text{radial}}$, is important because this determines how much current is going through the thermoelectric powder. Due to the low thermal conductivity of the TE powder, relatively small current densities can create large temperature gradients in the TE powder. The major source of heat loss occurs via conduction where the plunger meets the spreader plates ($20400 \text{ W/m}_{\text{thickness}}$) rather than via radiation at the surface of the insulation ($2750 \text{ W/ m}_{\text{thickness}}$). Thus the thermal/electrical resistance between the plunger and spreader $h_{g,\text{axial}}$, $\rho_{g,\text{axial}}$, are critically important properties for the overall energy balance of the DHP process.

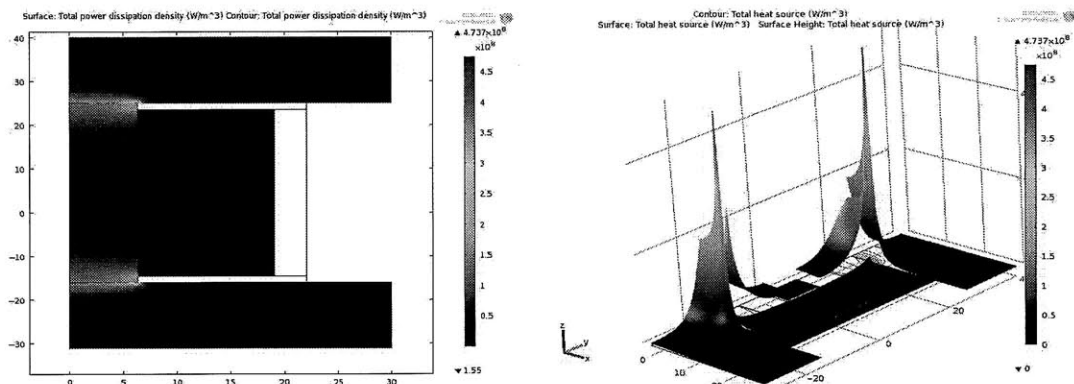


Figure 3-24: Total power dissipation density (left) 2D field (right) 2D field projected in the Z direction. The majority of the Joule heating occurred at the narrow section of the plungers near the contacts.

3.3.3.2 DHP Model Validation

It was important to validate the FE model in the DHP configuration so that it could be used to accurately predict new configurations in the HHP. The model was validated by thermocouple data, current data, and thermal radiation observations. Usually the temperature is monitored by a single thermocouple T_{die} , located in a hole with the die close to the sample. For the following test a hole and slot was drilled in the top plunger and a second thermocouple T_{plunger} , was positioned in the center a few mm from the top edge of the sample (figure 3-23). A 2 mm thick N-type sample was pressed under normal conditions (5 min at $T_{\text{die}}=700^\circ\text{C}$, $P=67\text{MPa}$) and the two temperatures were recorded. The largest temperature difference between the two thermocouples of 44°C occurs at the steady state maximum temperature (figure 3-25). The modeled produced a similar temperature difference of 37°C (figure 3-26). The good

agreement between model and experiment proves that the FE model material properties, contact resistances and boundary conditions are reasonable. The current needed to reach the calculated $T_{die}=710^{\circ}\text{C}$ is within 15% of the actual current and would probably be closer if a full 3D model was used. A steady state model was appropriate for the sintering process because the sample comes to steady state quickly (figure 3-25). A transient model would surely give more information was not necessary to guide the design of the new HHP process. During press the thermal radiation was monitored by eye to check how intensely sections were glowing and thus give a rough estimate of temperature. Though not as quantitative as thermocouple data it is essential to monitor the plunger so that it does not overheat and fail under compression.

The FE model and verification experiments show a large difference between the T_{die} at the perimeter of the sample and $T_{plunger}$ at the axis of the sample. Therefore when pressing conditions have been optimized for T_{die} temperature it is far different from the sample temperature on the order of 40-50°C. Furthermore this temperature difference is not constant because as a die and plunger age the thickness of the gap between them increases and thus the electrical/thermal contact increases. This ambiguity in actual sample press temperature is a major source of variability in the process which leads to a larger uncertainty in ZT.

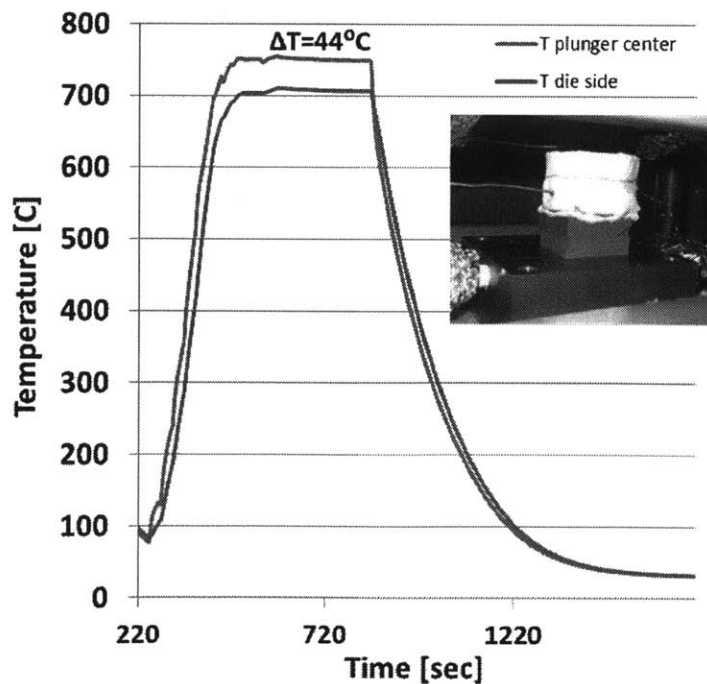


Figure 3-25: Model verification test. Experimentally measured $T_{plunger}$, T_{die} versus time for a N-type, 2 mm thick sample. The maximum temperature difference between $T_{plunger}$ and T_{die} occurs at steady state.

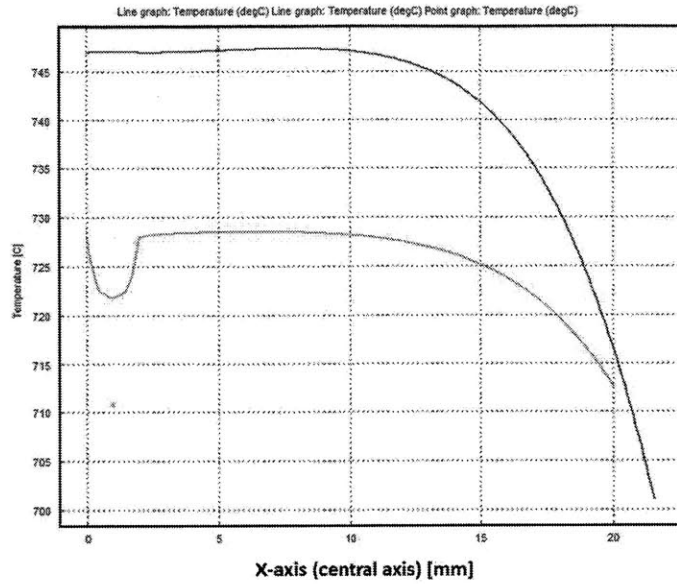


Figure 3-26: Calculated temperature along the plunger/sample axis (blue) and the plunger/sample perimeter (green) for the N-type, 2 mm thick verification sample. The TE sample extends from 0-2 mm on along the x-direction. Red point denotes T_{plunger} , blue point denotes T_{die} . The dip in the green curve is a results of heat conducting from the samples to the die.

Figure 3-27 plots the temperature field in the die and device sample during high temperature sintering at 700°C. The temperature of the graphite die, is very uniform, however there is a large temperature difference between die-plunger and die-sample due to radial thermal contact resistances $h_{\text{TE,radial}}$, $h_{\text{g,radial}}$.

The temperature field within the sample varies by 39°C and has two implications 1) it leads to non-uniform properties which have been observed in different TE material systems 2) it creates thermal stress within the sintered samples. Figure 3-27 shows that large temperature gradients are generated near the mid-plane ($x=5$ mm) of the sample during sintering at high temperature. This is the best explanation to why we observed fractures at the mid-plane in otherwise flawless device samples.

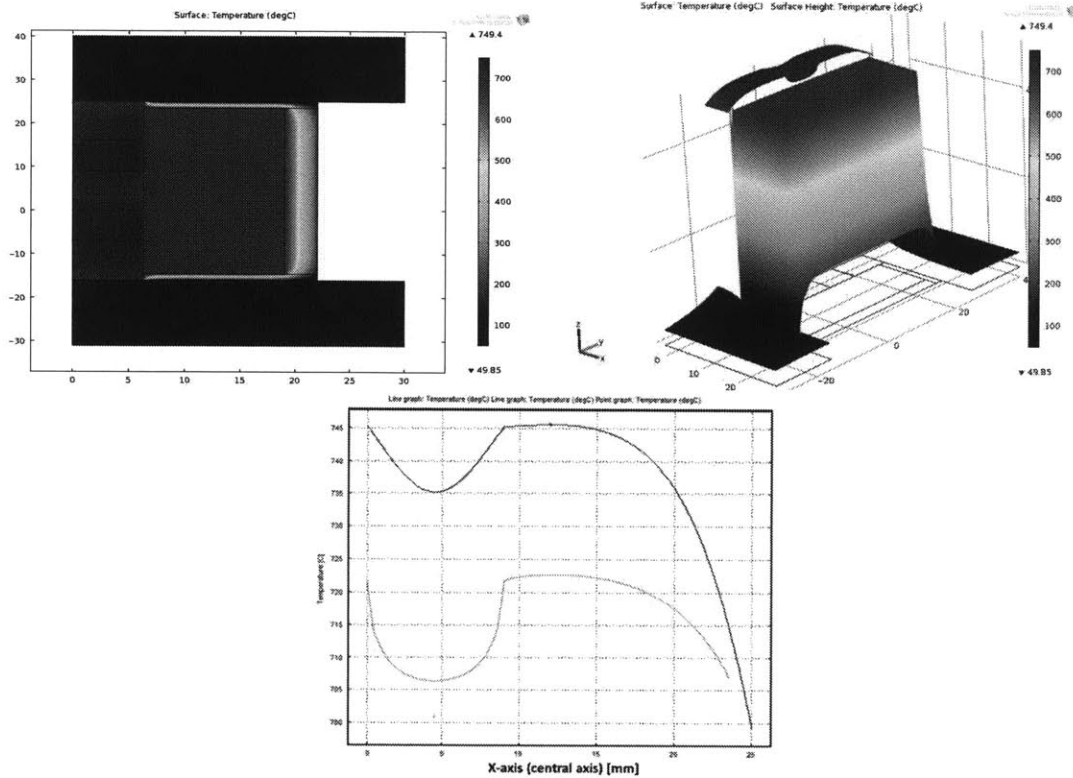


Figure 3-27: Temperature field of the direct hot press (DHP), device sample, with $h_{\text{sample}}=10\text{mm}$. (top left) 2D temperature field (top right) 2D temperature field projected in z-direction (bottom) temperature along the plunger/sample axis (blue) and the plunger/sample perimeter (green). Red point denotes T_{plunger} , blue point denotes T_{die} . Notice the large temperature gradients within the sample and the discontinuity at the plunger-die interface.

3.3.3.3 Hybrid Hot Press

The biggest problem with the DHP is that the temperature is non-uniform within the sample leading to cracks at the mid-plane. There is a large difference between the measured T_{die} and the actual temperature of the sample which is sensitive to contact resistance and leads to poor repeatability. The new configuration fixes both of these problems by creating a uniform sample temperature which is very close to the measured T_{die} .

The new configuration in figure 3-22 uses a smaller diameter and electrical/thermal insulating plugs on the top and bottom of the sample. Changing from a $\frac{1}{2}$ " to $\frac{1}{4}$ " diameter had several practical advantages to producing device samples.

- 1) The device sample is $\frac{1}{4}$ the original volume. Therefore by a 0th order argument there is $\frac{1}{4}$ the chance of a defect that will initiate a fracture which will propagate through the sample.
- 2) The cross sectional area is small enough to allow ZT_{eff} measurements without having to dice the sample into smaller legs. This can avoid fractures initiated at cutting, however it is still preferable to use smaller legs during device measurements.
- 3) One fourth the powder is used thus increasing throughput by reducing powder preparation time involved with ball-milling, melting, and cutting electrodes.
- 4) Less bending stress on the electrode during press and so that they are less likely to fracture (see E: Mechanical Loading on Electrode During Press).
- 5) Higher pressures can be reached during press without breaking the die.
- 6) The thermal time constant is smaller such that a more uniform sample temperature is expected throughout the entire process.*

The insulting plugs have a height of 7 mm and are made from a machinable glass (Macor) with a low thermal conductivity of 1.5 W/mK compared to graphite at 100 W/mK.[†] The hypothesis was that the sample temperature equilibrates close to T_{die} because it is thermally insulated from the hot plunger and there is no joule heating in the sample. We call it a hybrid hot press (HHP) because the system heats rapidly via joule heating and cools rapidly by conduction to the spreaders like the DHP but it achieves an excellent temperature uniformity of a hot press (HP). The calculated temperature field of the HHP configuration is given in figure 3-28. The temperature inside the sample is uniform and differs from the die temperature by only 0.4-5°C.

* By an order of magnitude estimation the thermal time constant between the center and edge of a dense sample with $\alpha \approx 10^{-6} \text{ m}^2/\text{s}$ for the DHP sample with a radius of 6 mm is 36 sec compared to 9 sec for the 3 mm radius sample of the HHP.

[†] Macor machine able glass, $46\text{SiO}_2+17\text{MgO}+16\text{Al}_2\text{O}_3+10\text{K}_2\text{O}+7\text{B}_2\text{O}_3+4\text{F}+\text{trace elements}$

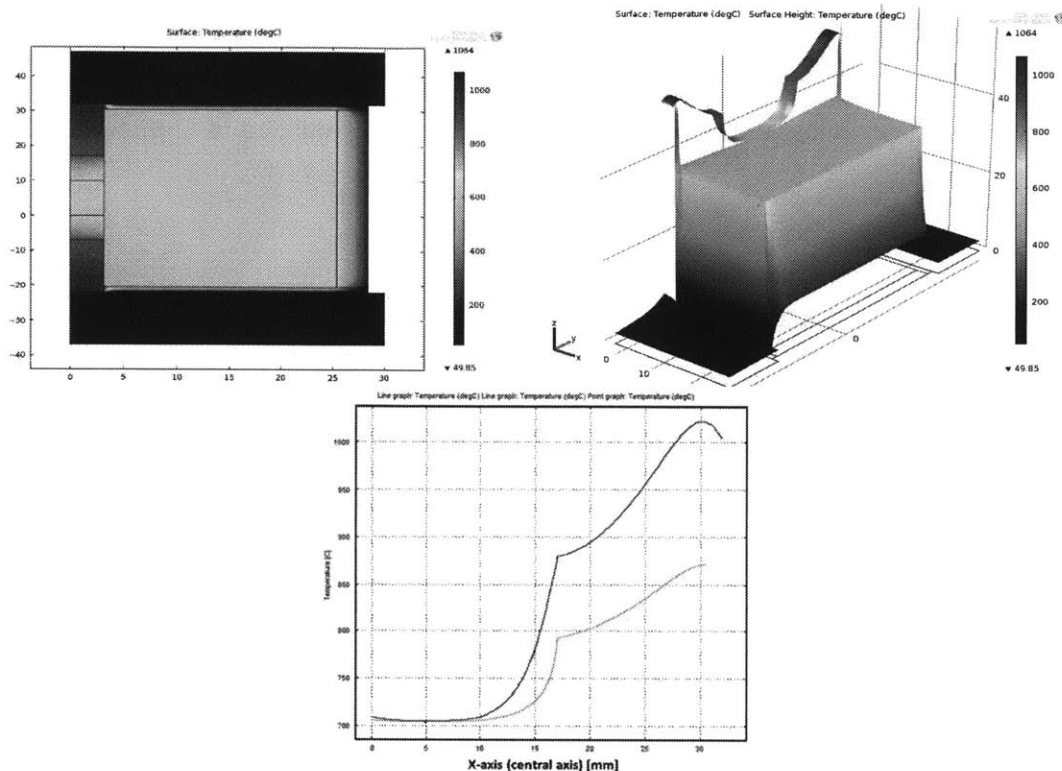


Figure 3-28: Temperature field of the hybrid hot press (HHP), device sample, with $h_{\text{sample}}=10\text{mm}$. (top left) 2D temperature field (top right) 2D temperature field projected in z-direction (bottom) temperature along the plunger/sample axis (blue) and the plunger/sample perimeter (green). Red point denotes T_{plunger} , blue point denotes T_{die} . The sample temperature is very uniform and close to T_{die} .

One concern about the HHP process is that sintering and densification may be negatively impacted by the absence of current. Based on literature results it is unlikely that DC current has a significant effect on sintering in the DHP. Electroplastic effects occur at a threshold current density of $10^3\text{-}10^4\text{ A/cm}^2$ which is two orders of magnitude higher than our current densities.⁶³ Spark plasma sintering (SPS) or FAST (Field-assisted sintering technique) uses high current in pulse widths on the order of milliseconds to enhance sintering. Langer *et al.* studied an alumina system and showed that although the SPS system achieved full density in shorter time than the hot press method, both processes finally produced equivalent grain sizes.⁶⁴ Tokita describes the mechanism of SPS and how a spark initiates the formation of a necking region between grains.⁶⁵ Based on the literature it is our understanding that SPS should be effective in initiating sintering at lower temperatures—especially at the electrode interface—but that final densities and grain sizes will be comparable to a HP process. Furthermore the sintering mechanisms of the DHP method which use relatively low DC current densities are more similar to the HP method than the SPS method. We have found experimentally that the contact resistance of samples made by

the DHP method are indistinguishable from samples made by the HHP method. We conclude by both literature studies and experimental evidence that the presence of current in the DHP has a negligible effect on sintering and the relevant variables can be reduced to temperature, pressure, and time.

3.3.4 HHP Device Samples

The final pressing conditions of the N-type and P-type device samples are illustrated in figure 3-29. There are a few important differences between the HHP and DHP press conditions. Powder was originally added to the top and bottom of the sample to distribute the compressive load and prevent fractured electrodes. We later discovered that the powder layers could be replaced by 4 layers of graphite foil. At one point the N-type powder was contaminated with oxygen due to a faulty glove box and resulted in high electrical resistance at the contact and in the bulk. From then on we used uncontaminated powder and took precautions to reduce oxygen contamination during press. Powder was used on the top and bottom of the sample not to distribute the load, but as a getter material to absorb oxygen diffusing through the plunger-die gap during press.* A pressure of 42 MPa was applied at room temperature, enough to compress the powder by 1-2 mm and reduce oxygen gas permeability but low enough to avoid fracturing the electrodes.† At the beginning of press the exposed section of the plunger is relatively long and if too much current is provided it will overheat and fail. A constant current was set so that the plunger glowed red but not too brightly. Onset of sintering occurred at 400°C and from then on the current was slowly increased as the sample compressed. The heating rate of the HHP was less than that of the DHP due to the smaller plunger diameter. The N-type was sintered at a relatively high temperature/pressure/time of 750°C/6min/84MPa to achieve a higher density and low contact resistance. The P-type samples was pressed at a lower temperature and time of (675°C/3min/98MPa) to limit mass diffusion at the interface and produce a smaller contact resistance. The P-type was more prone to cracking than the N-type so we controlled the cooling rate at ~20 K/min while simultaneously reducing the pressure until it reached 600°C where the

* The extent of oxidation can be evaluated visually on the boundaries of the sample.

† A displacement gauge was added to the press to monitor densification in situ.

sample was subsequently removed from the press and air cooled. The press conditions were successfully optimized to produce un-fractured samples with low contact resistance; however these conditions can be changed to further optimize ZT of a specific batch of powder.

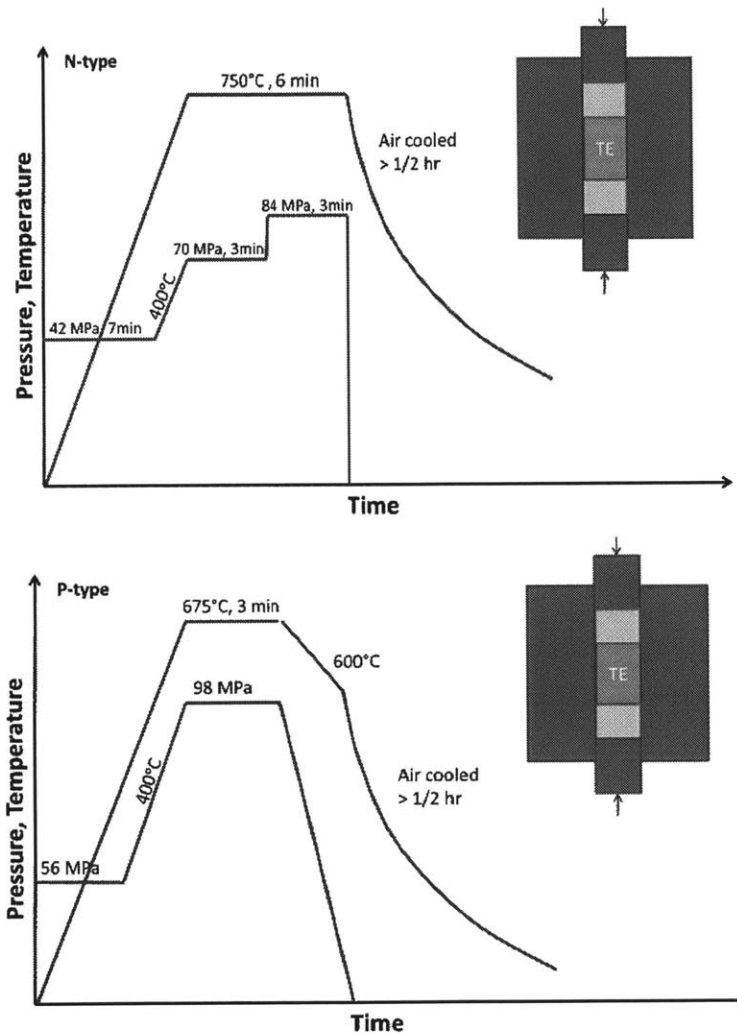


Figure 3-29: Hybrid hot press (HHP) device sample pressing conditions. (top) N-type (bottom) P-type.

After press the device samples were subsequently polished, inspected for cracks and the electrical resistance was measured as a function of length at room temperature. The bulk resistivity of the TE/electrodes and contact resistance are given in figure 3-30 and figure 3-31. The bulk resistivity values were within the expected range and the samples showed no sign of cracks at the mid-plane. The electrical contact resistance was measured at room temperature by the method described in Appendix D: Contact Resistance. The values are an upper limit estimate.

The P-type had an electrical resistivity of $1.2\text{-}2.3\text{e-}10 \Omega\text{m}^2$ and is 1.5-2.9% of the total resistance of the leg. The N-type had an electrical resistivity of $0.7\text{-}2.0\text{e-}10 \Omega\text{m}^2$ and is 0.8-2.2% of the total resistance of the leg. The device samples were successfully cut and polished into 4 pieces each, and two of each type were tested (figure 3-32). The geometry is given in table 4-4, the total uncertainty in A/L is 6.2%.

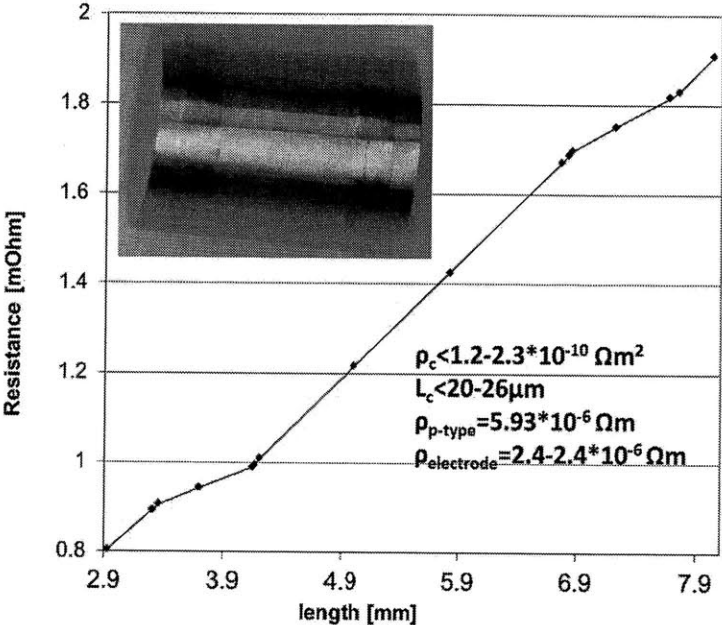


Figure 3-30: Resistance versus length of P-type device sample. The electrical contact resistance, contact region length, TE bulk resistivity and electrode bulk resistivity are given.

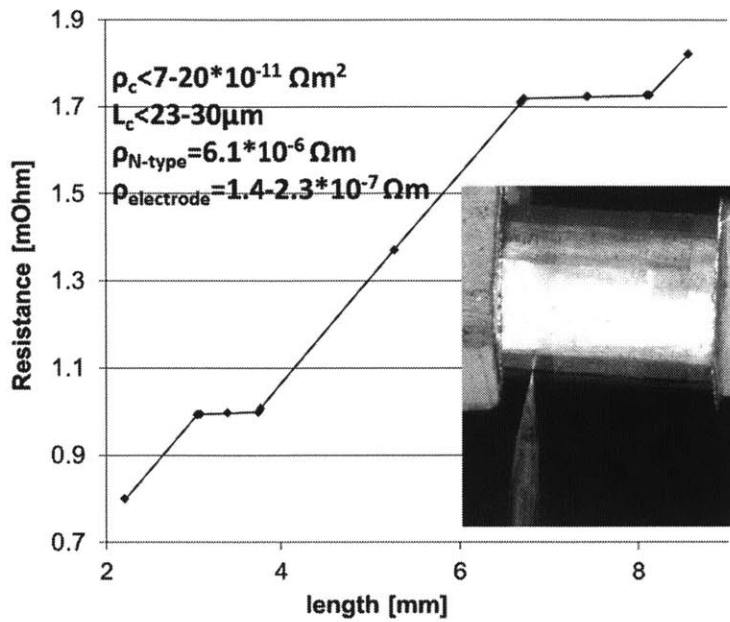


Figure 3-31: Resistance versus length of N-type device sample. The electrical contact resistance, contact region length, TE bulk resistivity and electrode bulk resistivity are given.

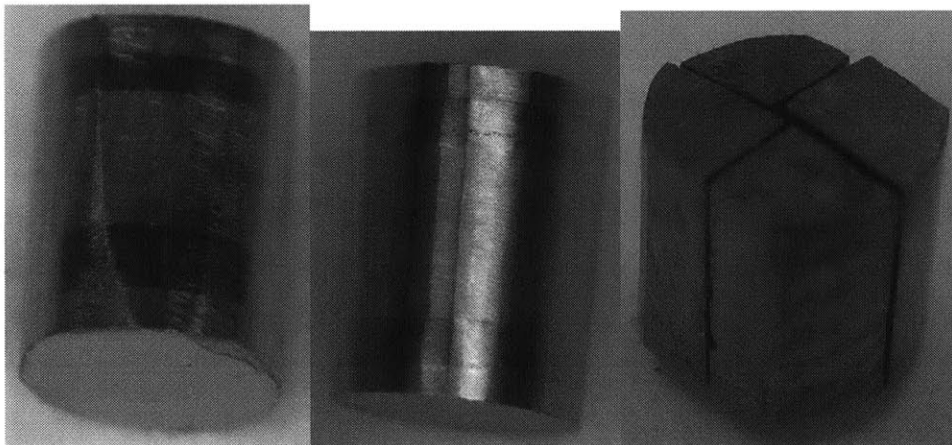


Figure 3-32 Device samples. (left) N-type after press (middle) P-type after press (right) P-type after final polish and cutting two produce four device samples.

Table 4: Geometry of device samples used in device testing. The uncertainty in A/L_{TE} is 6.2%.

	N leg1	N leg2	P leg1	P leg2
A [mm ²]	3.99	4.07	3.8	3.46
L_{TE} [mm]	3	3	2.696	2.696
$L_{\text{electrode}}$ [mm]	0.85	0.85	0.85	0.85
$L_{TC\text{-interface}}$ [mm]	0.35	0.35	0.35	0.35

The device legs can potentially be assembled into a module and joined with braze or solder. Fragments of CoSi_2 and Co_2Si were polished and brazed together with 56Ag22Cu17Zn5Sn braze, and a standard braze flux (figure 3-33). The melting point of the braze was between 618-652°C. The resulting contact resistance of the CoSi_2 -Braze- Co_2Si layer was very low at about $4 \times 10^{-11} \Omega\text{m}^2$. We also found that $\text{Sn}_{63}\text{Pb}_{37}$ solder ($T_{\text{melt}}=183^\circ\text{C}$) wetted the electrode surface if an aggressive aluminum flux was used.* The results are especially encouraging because the braze or solder has not been optimized of the electrodes. The method offers a potential solution for joining the device legs and fabricating a module. When the braze solidifies the density change may create stress at the TE-electrode interface. The biggest challenge will be to determine the best temperature to braze the high temperature contacts, and how to evenly heat the electrodes to reduce thermal stress during brazing.

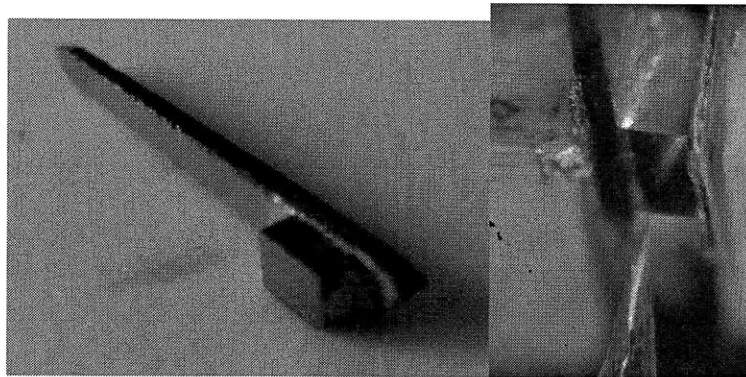


Figure 3-33: Brazed electrodes. CoSi_2 brazed to Co_2Si using 56Ag22Cu17Zn5Sn. The contact resistance was measured to be very low.

* Aluminum solder flux is a chemical solder which allows for soldering directly to aluminum.

3.3.5 Conclusions

Skutterudite device samples were fabricated by a direct bonding method in which a rigid electrode is sintered directly to the TE powder during press. Compatible electrode materials were identified and evaluated based on thermal stress, parasitic electrical/thermal resistance, chemical stability and ease of prototype fabrication. The final electrodes solutions were Co_2Si with the P-type and CoSi_2 with the N-type. The direct hot press process (DHP) was modified into what we call a hybrid hot press (HHP) to produce device samples with strong bonds and no cracks. The TE-electrode combinations meet all the criteria for device testing and offer a practical, manufacturable solution for module construction.

Chapter 4. Skutterudite Unicouple Testing

The experimental method described in this section is an extension of the method described in chapter two. Figure 4-1 shows the evolution from the test assembly in chapter two to the new assembly at higher temperature. At temperatures up to 600°C, radiation losses become more important and instrumentation such as heater construction and thermocouple placement are more challenging. In this chapter we describe the experimental device testing system including the instrumentation and methodology to measure the effective properties and conversion efficiency with high accuracy. Calibration and validation results are given. In the results section we compare the measured $Z\bar{T}_{eff}$ to the calculated results from the individual property measurements. The conversion efficiency of an NP couples is measured at 9.1% at a hot side temperature of ~550°C. The last section describes the accelerated aging experiments and mechanisms to the long term break down of the bonded electrode interface.

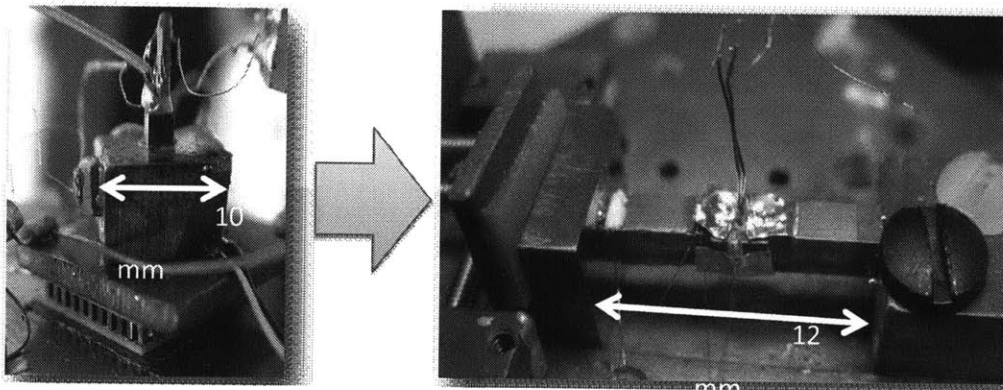


Figure 4-1: (left) Bi_2Te_3 test assembly from chapter two, capable of temperatures up to 235°C (right) skutterudite test assembly capable of temperatures up to 650°C.

We chose an inline configuration in which the legs are on the same axis instead of the more conventional parallel axis design (figure 4-2 and figure 4-2). An axial force is applied to hold the legs in compression (figure 4-3). Current and heat pass horizontally through the legs and is approximated as 1-D transport. Heat is generated in the middle at the heater assembly to raise its temperature up to 600°C while the ends are maintained near room temperature. The test is conducted on a cryostat in vacuum to eliminate air convection, however, we must still correct

for radiation losses at the heater and sides of the legs. Cold water is passed through the cryostat cold finger to maintain the cold side temperature. This configuration has the advantage of reduced shear stress at the hot side due to thermal expansion and reduced thermal losses due to a smaller heater assembly compared to the parallel axis configuration. The overall length of the device in figure 4-2 is 13 mm. There are two thermocouples on each leg measuring T_{cold} and T_{hot} and a thermocouple at the heater measuring T_{heater} . We measure the thermovoltage between each thermocouple junction as well. The ZT_{eff} measurement was performed by setting a heater voltage, allowing the system to come to steady state and then measuring the three device properties: Q_{hot} entering the legs, open circuit Seebeck voltage of each leg, and the electrical resistance of each leg. The ZT_{eff} measurement is taken between the thermocouples and includes heat losses at the sides of the legs, electrical contact resistance, and parasitic thermal/electrical resistances in the electrodes between the interface and thermocouples across a distance $L_{\text{TC-interface}}=0.35$ mm.

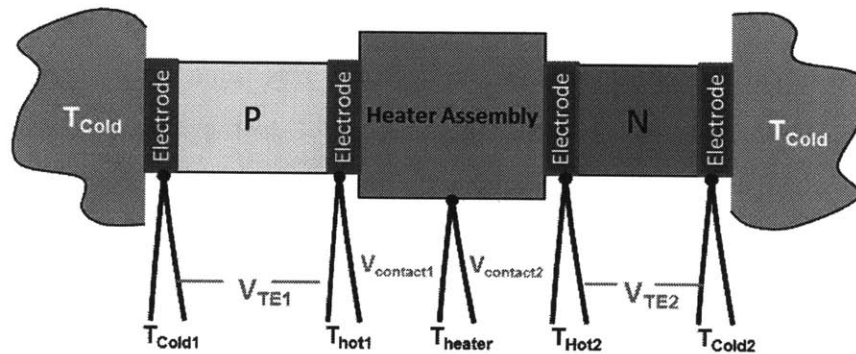


Figure 4-2: Schematic of the inline device measurement system.

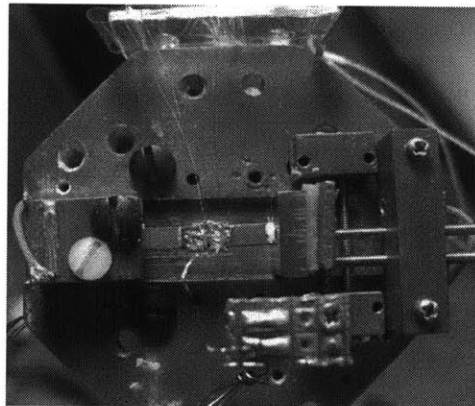


Figure 4-3: Test assembly mounted on the cold finger of a cryostat. Created by Qing Hao, modified by Andy Muto.

4.1. Calibration

It is not straightforward to calibrate thermoelectric measurement systems because our community does not yet have a standard NIST certified thermoelectric sample. Three calibration experiments were performed on this system: thermocouple calibration, Seebeck calibration and heater calibration.

The thermocouples were type K with a diameter of 2 mils. They were attached to the electrodes with silver epoxy. Upon raising the hot side to 260°C the organics would bake off leaving the thermocouple bead embedded in a sintered Ag matrix. There were three concerns with this method of attachment that would be tested.

- 1) Back of the envelope calculations suggested there could be a very large temperature difference between the substrate and bead across the silver epoxy on the order of 100°C (see Appendix C: Thermocouple Wire Heat Loss).
- 2) Type K thermocouple is known to have poor chemical stability at elevated temperatures in vacuum environments due to Ni sublimation, this trend gets worse with decreasing diameter. The question was whether the Seebeck of the thermocouple wire would change on a time scale shorter than that of the skutterudite in which case long duration testing would be not be reliable.
- 3) The uncertainty associated with the as-bought thermocouple wire, and the conditioning box measuring the voltages and temperatures.

A two part experiment was devised to validate all three concerns. Two Pt RTDs were embedded in a copper block, one would be used as a high temperature heater and the other as a thermometer to measure absolute temperature, T_{RTD} . The block was suspended by its connecting wires in vacuum and heated to create an isothermal block. A schematic is shown in figure 4-4. Two thermocouples T_{h1} , T_{h2} were attached with silver epoxy around the bead and then covered with alumina paste to improve thermal communication with the block. A third thermocouple, T_{hot} , was connected to the copper block with Ag epoxy only. The block was held at different temperatures while comparing T_{RTD} , T_{h1} , T_{h2} , and T_{hot} . Figure 4-4 shows no distinguishable

difference between thermocouples and only a small error between the three thermocouples and T_{RTD} . Therefore sintered silver epoxy is enough to achieve good thermal contact between the bead and substrate (alumina paste is not needed). Concern one has been resolved. To resolve concern two, the system was held at 600°C for 108 hrs and the test was repeated. There was no appreciable difference in thermocouple readings, therefore the thermocouples can be expected to measure accurate temperatures and voltages during a long duration device test.

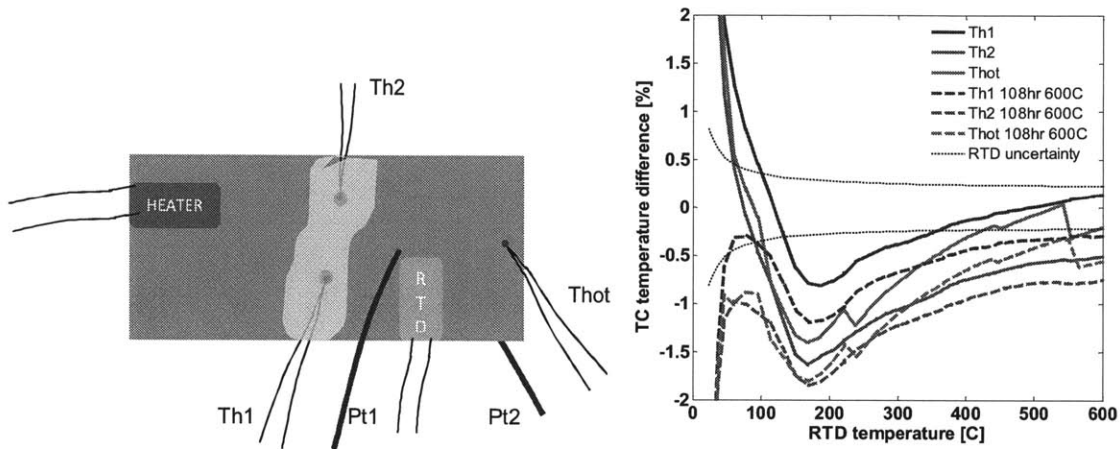


Figure 4-4: (left) Schematic of the isothermal block used in the thermocouple calibration and Seebeck calibration experiments. (right) Thermocouple calibration comparison. The measured temperature difference is relative to the Pt RTD measuring absolute temperature. The results prove that the thermocouple attachment method is valid at high temperatures and for long duration.

A Seebeck calibration was performed to resolve the third concern. Platinum was deemed the best material to measure the Seebeck coefficient because it is extremely stable with repeatable transport properties. For instance, there would be no surface oxides with varying Seebeck coefficients. Also the magnitude of the Seebeck is very small ($\sim 10\mu\text{V/K}$) so that any deviation from the literature value due to small errors in the system would become obvious. Two platinum wire leads were connected to the hot copper block and thermocouples near room temperature on the cold side. The open circuit Seebeck voltage was measured between each thermocouple pair and the Seebeck coefficient was solved for by the methods described in Chapter 2. The measured Seebeck of Pt shows excellent agreement with literature values even after a long duration test (figure 4-5). The calibration curve simultaneously resolves concerns 1-3, and proves that the thermovoltage across the alumel wires was compensated correctly. These results give a high degree of confidence in the device measurements.

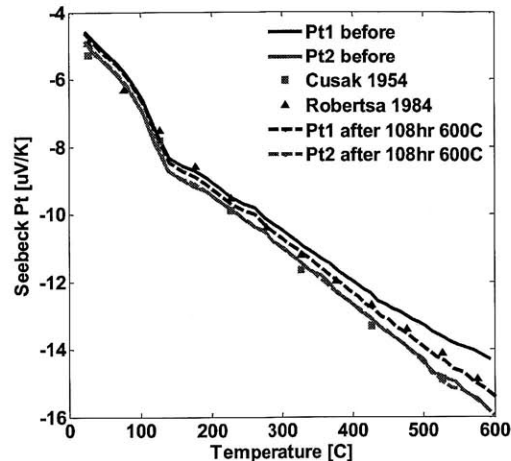


Figure 4-5: Pt wire Seebeck calibration. The wires Pt1 and Pt2 were measured by two different thermocouple pairs. The measured Seebeck of Pt is in excellent agreement with literature.^{66,67}

4.2. Heater Assembly Fabrication

The requirements of the heater were to provide 6 W at 600°C for hundreds of hours without failure with small thermal losses. It is important that the heater assembly be as small as possible with small electrical leads to reduce radiation and conduction losses at high temperature. All commercially available heaters such as miniature cartridge heaters are too large, therefore it was necessary to make one from scratch by repurposing an existing product.

After many iterations in heater design the final solution was to imbed 2 platinum RTDs in a Cu block. Two slots were milled in a 3x3x3mm Cu block and the side walls were polished to minimize the emissivity. A platinum RTD* was inserted into each slot and filled with braze (45Ag27Cu25Zn3Sn braze, $T_{\text{melt}}=641\text{-}682\text{C}$). Figure 4-6 shows the heater with an attached cover plate to minimize the emissivity. The current was supplied by 2 mil Pt wire, 25mm in length, which were brazed to the electrical leads. A type K, 2 mil, thermocouple was attached to measure T_{heater} .

*RTD procured from Omega Engineering <http://www.omega.com/ppt/pptsc.asp?ref=F1500 F2000 F4000>

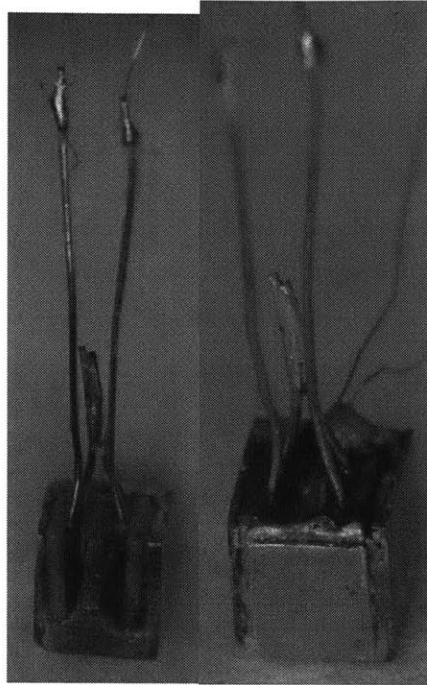


Figure 4-6 Calibrated heater using two RTDs backfilled with braze. (left) Before Cu cover plate was attached. (right) After cover plate was attached.

The heater assembly was calibrated for heat loss by suspending it in vacuum ($<5 \times 10^{-5}$ torr) and measuring the steady state electrical power needed to keep it at temperatures up to 625°C (figure 4-7). The total electrical power dissipated by the heater IV_{Heater} , was measured by a 4-wire method at the ends of the platinum leads. The heat losses due thermocouple wire conduction losses $Q_{\text{loss},TC}$ and platinum lead losses $Q_{\text{loss},Pt}$ were calculated by a 1-D radiating fin model. The 1-D radiating fin model was written as a function in Matlab with help from a colleague Ken McEnaney*, uses temperature dependent material properties and finds a numerical solution for a general thermoelectric conductor. The inputs are temperature dependent material properties, boundary temperatures, electric current, and geometry; the outputs are heat transfer on each end, radiation loss and voltage across the conductor. The heat transfer components of $Q_{\text{loss},Pt}$, $Q_{\text{loss},TC}$ are plotted in figure 4-8, including the hot side heat transfer at the thermocouple, hot and cold side heat transfers in the heater leads, and joule heat and radiation loss at the heater

*The matlab function has the following file name: `thermoelectric_1D_radiation.m`

leads. The combined correction from these losses account for only 5% of the total heater losses at 600°C.

The total heat loss at the heater surface Q_{Heater} was modeled using a temperature dependent emissivity of the form $e = e_0 + e_T T_{heater}$ and a convection coefficient U by the following equation

$$Q_{Heater} = IV_{Heater} - Q_{loss, Pt} - Q_{loss, TC} = A_{Heater} (e_0 + e_T T_{heater}) (T_{heater}^4 - T_{\infty}^4) + A_{Heater} U (T_{heater} - T_{\infty}). \quad (4.1)$$

The three constants $e_0 = 0.1822$, $e_T = 7.9 \cdot 10^{-5}$, $U = -0.0033$ were solved for by least squares regression with the measured IV_{Heater} data. The magnitude of the convection term is plotted in figure 4-7 and is negligibly small, this is further evidence that the vacuum was effective in suppressing air conduction and that the wire losses were calculated accurately. The resulting average emissivity at low and high temperature are $e(65^\circ C) = 0.209$ and $e(625^\circ C) = 0.253$. Figure 4-7 plots the experimentally measured and calculated Q_{Heater} . The regression fit with the radiation term is an excellent fit.

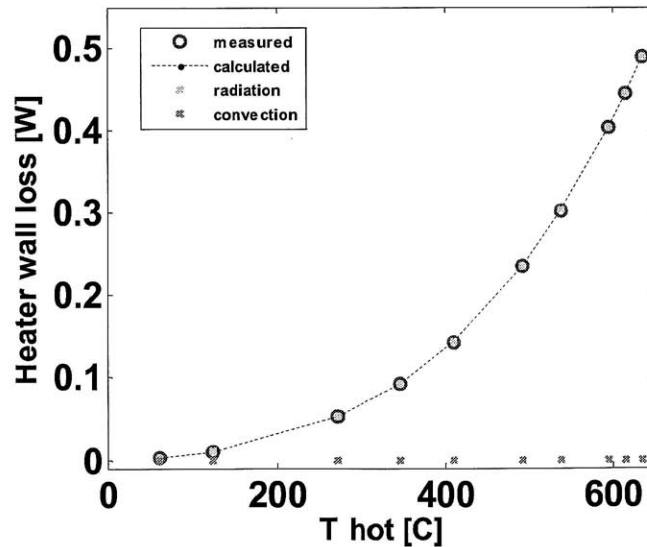


Figure 4-7: Heater calibration with measured and calculated values from Eq.(3.1).

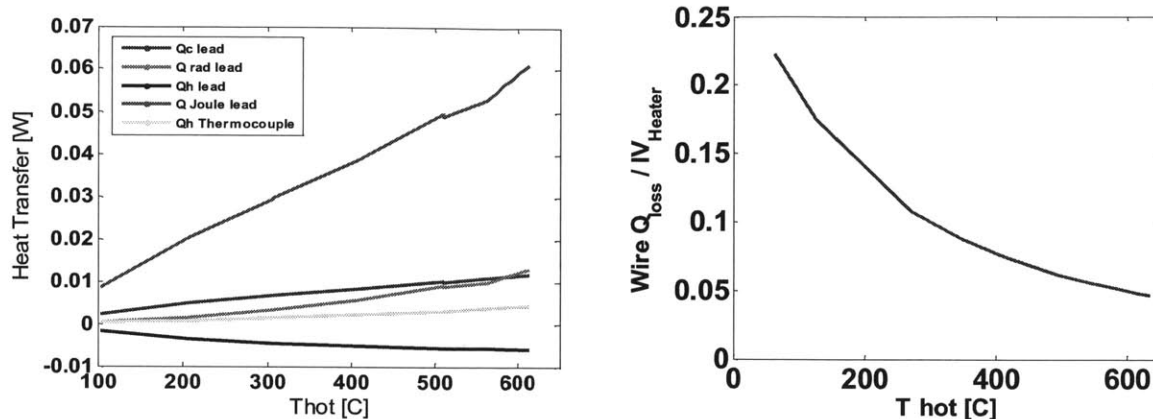


Figure 4-8: (left) Calculated heater loss from the connecting wires. (right) Proportion of the calculated wire heat loss to the total power dissipated at the heater.

4.3. Single Pair Fabrication

The legs were mounted in an inline configuration and held in compression. The surfaces were polished to reduce their emissivity. The thermocouples were 35 mm long and attached to the electrodes, ~0.35 mm from the interface with silver epoxy and cured at 120°C for 8 hrs (figure 4-9). Originally the device legs were bonded to the heater assembly by a layer of Ag epoxy between the hot side electrode and the Cu heater block. At high temperature the organics would bake off leaving a sintered Ag bond with relatively low electrical and thermal contact resistance. After long duration high temperature testing it was found that Cu would diffuse into the CoSi₂ electrode and cause it to crack. Thus a 12.5 μm layer of Ni foil was inserted in-between the hot electrode and Cu heater block and bonded with Ag epoxy (figure 4-9). This was effective in protecting the electrode from Cu diffusion, but at the expense of high electrical contact resistance. Once the legs and heater were loaded the thermocouple wires were wrapped around their respective terminals and the heater electrodes were soldered to their terminals (figure 4-11). Connecting the thermocouples and electrodes such that the wires did not short circuit or break was a painstaking process that required great hand-eye coordination with tweezers under a working microscope. However with practice this procedure could be executed with confidence. The electrical connections were then tested at room temperature before loading into the cryostat under vacuum. Before taking data the samples were tested above ~260°C and the signals were monitored for signs of short circuit. It was common for the thermocouples to

rotate during Ag sintering and short-out. At that point the sample would have to be taken out of the chamber so that small adjustments could be made to the thermocouple wire.

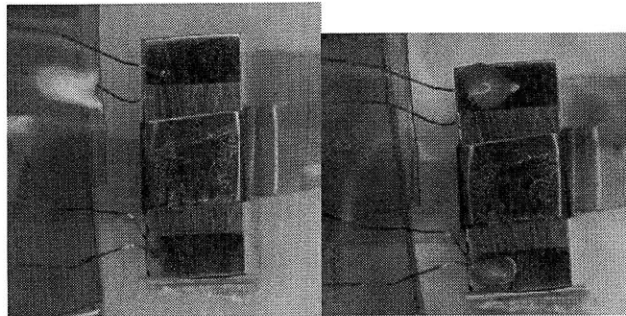


Figure 4-9: Thermocouple attachment method. (left) Bare thermocouple wires were positioned on the electrode, ~0.35 mm from the interface (right) and attached with Ag epoxy and subsequently cured at 120°C for 8 hrs.

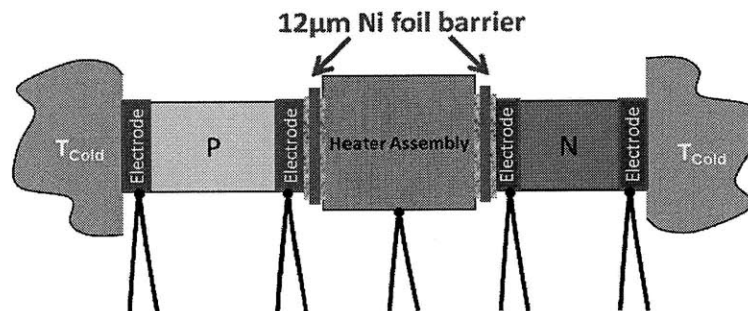


Figure 4-10: Ni foil (12.5 µm) was inserted in between the electrodes and heater assembly to function as a diffusion barrier.

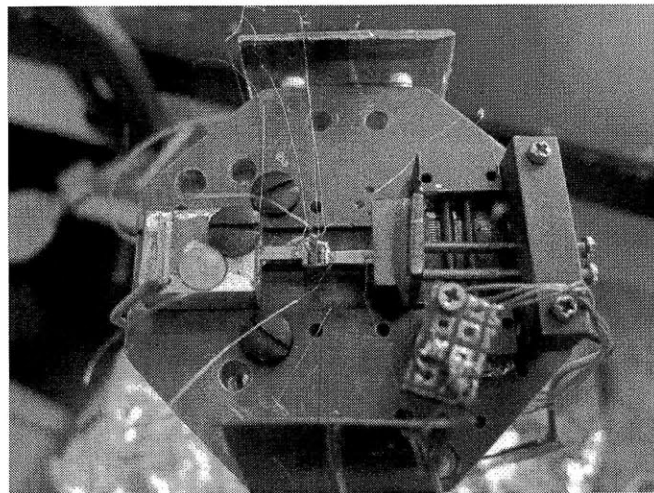


Figure 4-11: N-N device sample loaded into testing assembly, prior to connecting thermocouple wires and heater electrodes.

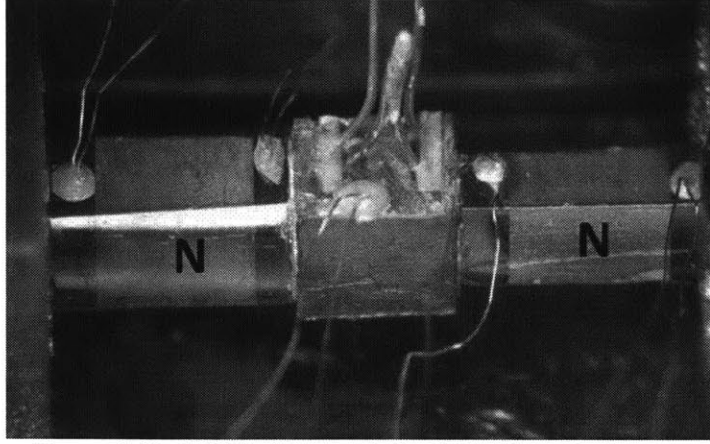


Figure 4-12: N-N device sample loaded and ready for test.

4.4. Data Analysis

The device properties V_S and R were measured by the methods described in Chapter Chapter 2. The hot side heat Q_{hot} entering the legs had the largest uncertainty of all three device properties. The thermal losses are illustrated in figure 4-13. The total hot side heat is found by

$$Q_{hot} = IV_{Heater} - Q_{loss,Pt} - Q_{loss,TC} - Q'_{Heater} - Q_{electrodes}, \quad (4.2)$$

where Q'_{Heater} is solved for by Eq.(3.1) and the exposed surface area of the heater has been reduced by the cross sectional area of the legs $A_{C,Legs}$, such that $A'_{Heater} = A_{Heater} - A_{C,Legs}$. The electrodes were modeled as isothermal with a constant emissivity at the temperature measured by each hot side thermocouple,

$$Q_{electrodes} = \varepsilon_1 \sigma_{sb} P_1 (L_{e1} - L_{TC-interface}) (T_{h1}^4 - T_{\infty}^4) + \varepsilon_2 \sigma_{sb} P_2 (L_{e2} - L_{TC-interface}) (T_{h2}^4 - T_{\infty}^4), \quad (4.3)$$

where P is the perimeter of each leg. We used an FTIR (Fourier Transform Infrared Spectroscopy) to measure the emissivity of the electrode and skutterudite surfaces after completing the ZT_{eff} testing. The surface properties visually change after exposed to high temperature testing due to Sb sublimation and oxidation so it was more appropriate to measure the surface properties after ZT_{eff} testing rather than before. Figure 4-14 plots the reflectance raw

data of the 4 surfaces, where emissivity=1-reflectance. Table 5 gives the emissivity values used in the calculation, including the upper and lower bound values used in the uncertainty analysis (Appendix B: Uncertainty Analysis).

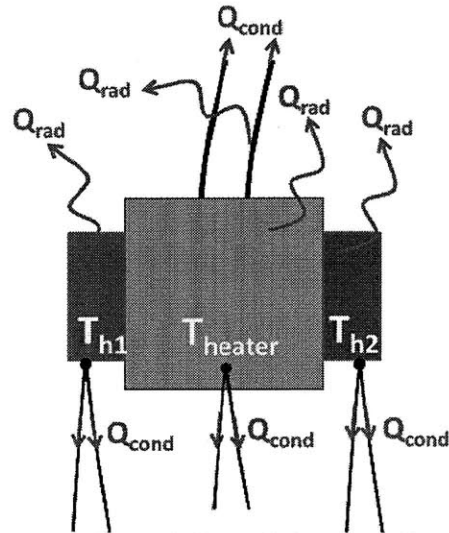


Figure 4-13: Schematic of heater assembly and electrode losses used to solve for Q_{hot} entering the legs.

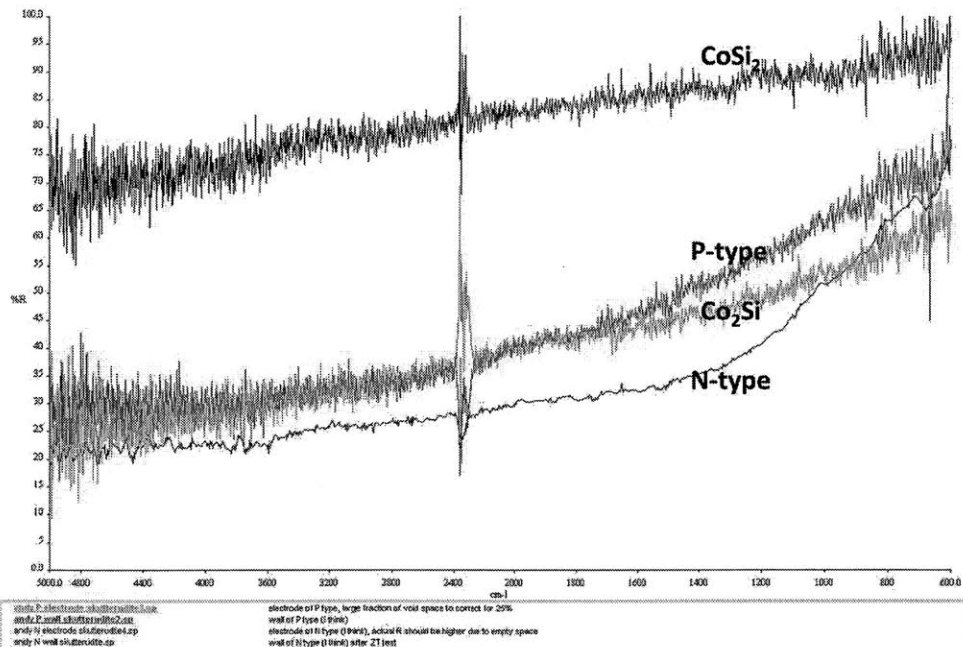


Figure 4-14: Reflectance versus wavenumber of the skutterudite wall and electrodes. This is the raw data taken from an FTIR (Fourier transform infrared spectroscopy) which was used to calculate the emissivity of each surface.

Table 5: Surface emissivity nominal values and upper and lower bounds. The N and P-type emissivity do not have upper and lower bounds because these values were only used in the model results.

surface	e	e+	e-
N-type	0.7		
P-type	0.6		
CoSi ₂	0.23	0.35	0.15
Co ₂ Si	0.5	0.7	0.40

The heater loss represents the largest thermal loss at about 7% of IV_{heater} at high temperature but contributes relatively little uncertainty to Q_{hot} (figure 4-15). The electrode loss is 4.4% of IV_{heater} at high temperature and is the major source of uncertainty in Q_{hot} . The maximum total correction factor of the N-N test is 12.4% and the P-P is 21% (figure 4-16). The P-P system has a larger thermal loss correction because the emissivity of Co₂Si is greater than CoSi₂ and the magnitude of IV_{heater} is smaller due to a smaller thermal conductivity. Figure 4-17 plots the total upper and lower bound uncertainty in Q_{hot} for the N-N and P-P measurements at each temperature.

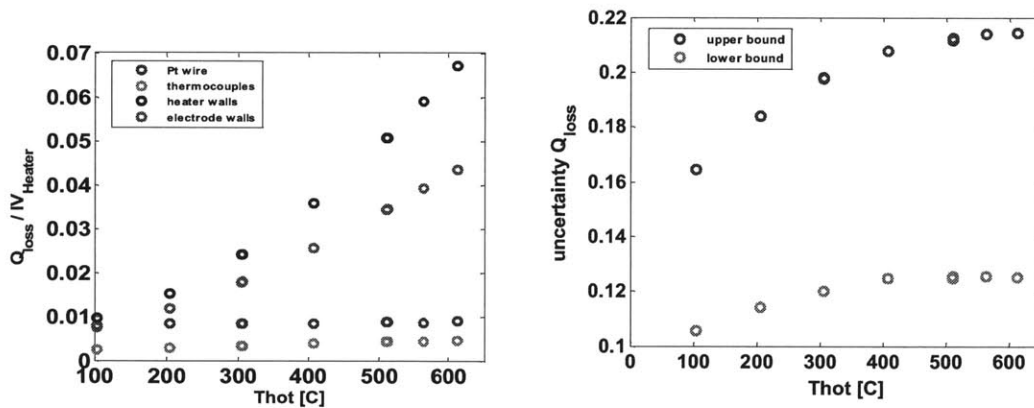


Figure 4-15: (left) Magnitude of the loss correction relative to the total dissipated power IV_{heater} (right) upper and lower uncertainty limits of the cumulative Q_{loss} corrections. Results are from the N-N test.

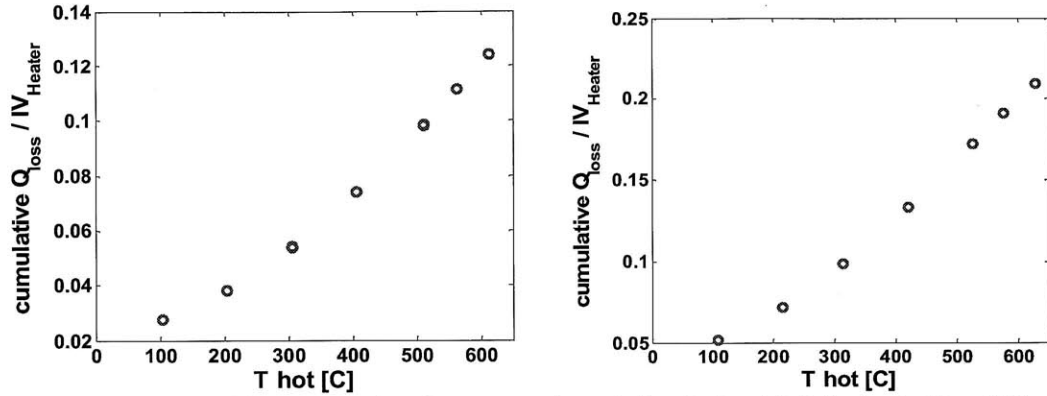


Figure 4-16: Magnitude of the cumulative Q_{loss} correction relative to the total dissipated heat IV_{heater} . (left) N-N test (right) P-P test.

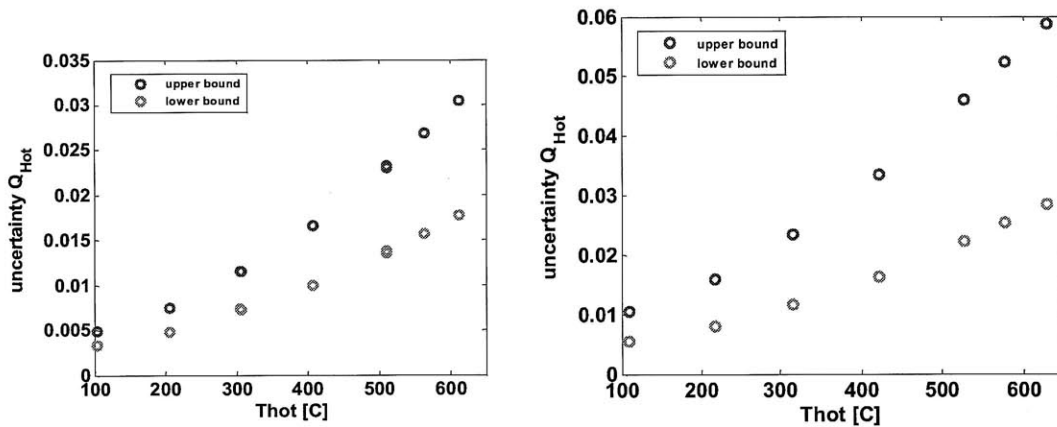


Figure 4-17: Total upper and lower bound uncertainty in Q_{Hot} for (left) N-N and (right) P-P test, units are in W.

4.5. Device Measurement Results

There are a several ways to analyze the device measurement data. In this section we compare the measured effective properties to the calculated values. The calculated values are based off the individual properties measurements in section 3.1.1 and the electrode properties in section 3.2.3. The effective resistivity and thermal conductivity have geometric parameters that introduce more uncertainty; while the effective ZT does not have any geometry parameters. The cross section of the device legs are not rectangular (figure 3-32), in order to reduce the total geometry uncertainty we used the measured cross section of one leg and used the following relation during the effective ZT measurement (N-N and P-P configuration) to calculate the cross section of the second leg,

$$A_{C,leg2} = \frac{R_1(T_\infty)}{R_2(T_\infty)} A_{C,leg1}. \quad (4.4)$$

The resistance measurement was taken at room temperature and assumes $L_1 = L_2$, and $\rho_1(T_\infty) = \rho_2(T_\infty)$. In this way we've minimized the uncertainty in $A_{C,leg2}/A_{C,leg1}$. The heat going through each leg cannot be measured individually. Thus, we assumed that $L_1 = L_2 = L$, and $k_{eff1}(T_{h1}, T_{c1}) = k_{eff2}(T_{h2}, T_{c2}) = k_{eff}(\bar{T}_h, \bar{T}_c)$, where $\bar{T}_h = (T_{h1} + T_{h2})/2$. We then solve for the mean effective thermal conductivity,

$$k_{eff}(\bar{T}_h, \bar{T}_c) = \frac{Q_{Hot}}{\frac{A_1 \Delta T_1}{L} + \frac{A_2 \Delta T_2}{L}} = \frac{Q_{Hot}}{\frac{A_1 \Delta T_1}{L} \left(1 + \frac{R_1(T_\infty) \Delta T_2}{R_2(T_\infty) \Delta T_1} \right)} \quad (4.5)$$

The measured room temperature electrical contact resistance was 1.5-2.9% the total resistance of the P-type leg, and 0.8-2.2% of the N-type (3.3.4 HHP Device Samples). We did not include electrical contact resistance in the modeled result. However, we could have included it by assuming that the contact resistance scales proportional to the bulk resistivity with temperature. The uncertainty of each measurement was individually calculated; the maximum values are given in Table 6. Details of the uncertainty analysis are given in Appendix B: Uncertainty Analysis.

Table 6: Maximum uncertainty in effective property measurements

	N-type upper bound	N-type lower bound	P-type upper bound	P-type lower bound
Seebeck	0.011	0.011	0.006	0.006
resistivity	0.067	0.067	0.062	0.062
thermal	0.069	0.065	0.086	0.069
ZT _{eff}	0.031	0.025	0.059	0.029
Efficiency	0.031	0.025	0.059	0.029

4.5.1 N-N results

Figure 4-18 plots the measured N-type effective properties and the effective power factor along with the calculated values. The “calc.” values were calculated with by using the corresponding geometry, temperature dependent thermoelectric properties, and emissive properties of the skutterudite and electrode, the “ideal” values only use the geometry and temperature dependent properties of the skutterudite. Error bars are included for each measurement point, the maximum values are given in Table 6. The thermal conductivity was assumed equal for the reason described above. The resistivity was assumed equal at room temperature, but remains nearly identical for all temperatures. The Seebeck is also nearly identical for all temperatures. Thus the near identical properties of each leg are evidence of good homogeneity in the device samples and high fidelity in the measurement system.

The magnitude of the effective Seebeck is much higher than expected and the resistivity is also much higher than expected. This is likely due to a different carrier concentration between the device samples and individual property measurements.* Notice that the measured power factor is similar to the calculated values. It is common for the Seebeck and resistivity to be different from batch to batch but produce similar power factors. The measured thermal conductivity exhibits a different trend than the calculated, the physical explanation is unclear. figure 4-19 plots $Z\bar{T}_{eff}$ and the corresponding maximum efficiency. The highest measured $Z\bar{T}_{eff}$ was 0.74 at 595°C on the hot side and 52°C on the cold side; this corresponds to a maximum conversion efficiency of 11.7%. The maximum calculated efficiency was 12.2% compared to an ideal efficiency of 13.1%. Thus the parasitic losses have degraded the efficiency by 0.9 efficiency points or reduced the power by 7%.

A previous N-N device test was conducted for 44 hours at ~590°C, the sample showed an annealing behavior where $Z\bar{T}_{eff}$ increased over time.† It was shown in section 3.3.1 that $Z\bar{T}$ of the N-type can easily vary by 15% based on pressing conditions and annealing. It should be

* Recall that the individual property measurements correspond to sample made by the original DHP process where the device samples were made using the HHP.

† The long duration N-N testing results are not given here, but were presented during several internal presentations.

possible to produce higher effective ZTs of the N-type device samples by further optimizing the pressing conditions of the HHP process and possibly introducing an anneal step.

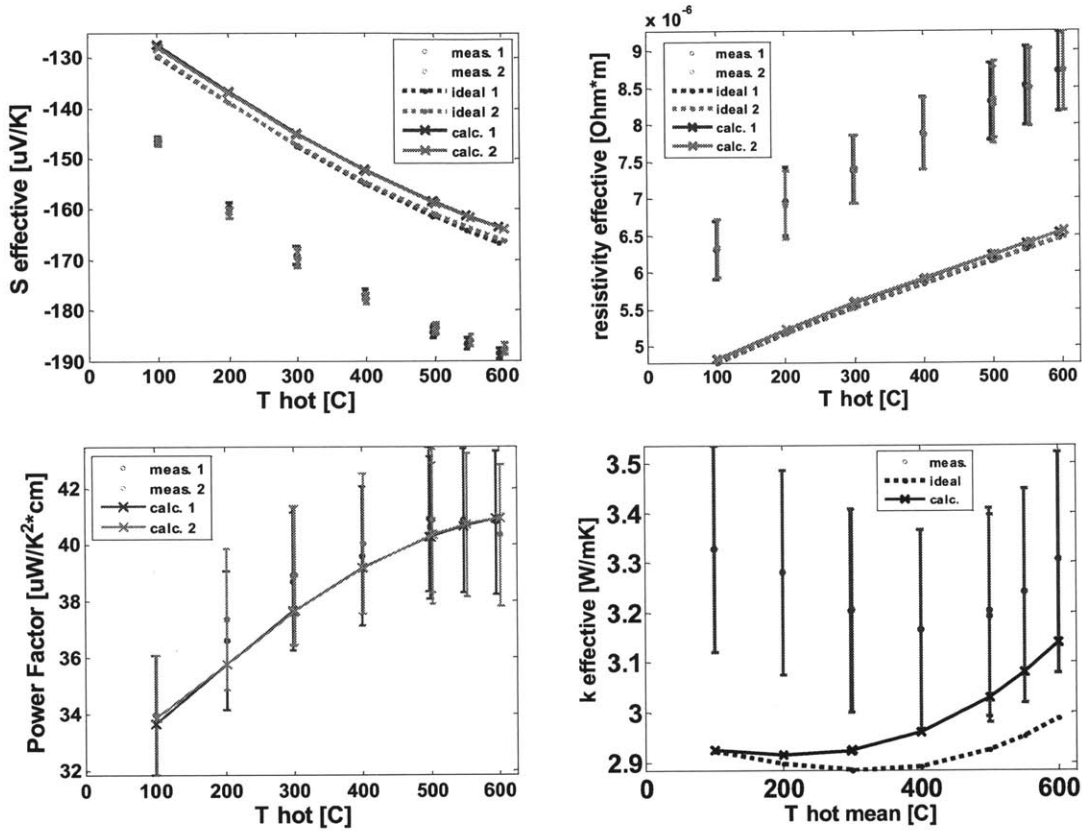


Figure 4-18: Effective properties of N-type device samples. The “calc.” values include the full thermoelectric properties (individual property measurements), surface emissivity and geometry of both the skutterudite and electrodes between the measured temperatures. The “ideal” values are calculated from the individually measured properties of the skutterudite only and measured temperatures assuming there are no electrodes and no sidewall radiation.

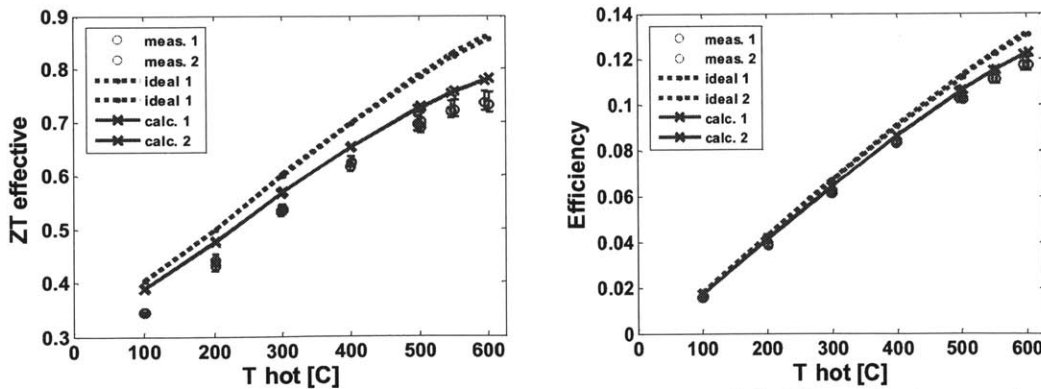


Figure 4-19: ZT_{eff} and corresponding maximum efficiency of the N-type device samples.

4.5.2 P-P results

Figure 4-20 plots the measured P-type effective properties and the effective power factor along with the calculated values. The measured property values of both leg are nearly identical and are in very good agreement with the calculated values. Figure 4-21 plots $Z\bar{T}_{eff}$ and the corresponding maximum efficiency. The highest measured $Z\bar{T}_{eff}$ was 0.51 at 600°C on the hot side and 77°C on the cold side; this corresponds to a maximum conversion efficiency of 8.5%. The maximum calculated efficiency was 8.2% compared to an ideal efficiency of 9.4%. Thus the parasitic losses have degraded the efficiency by 1.2 efficiency points or reduced the power by 13%.

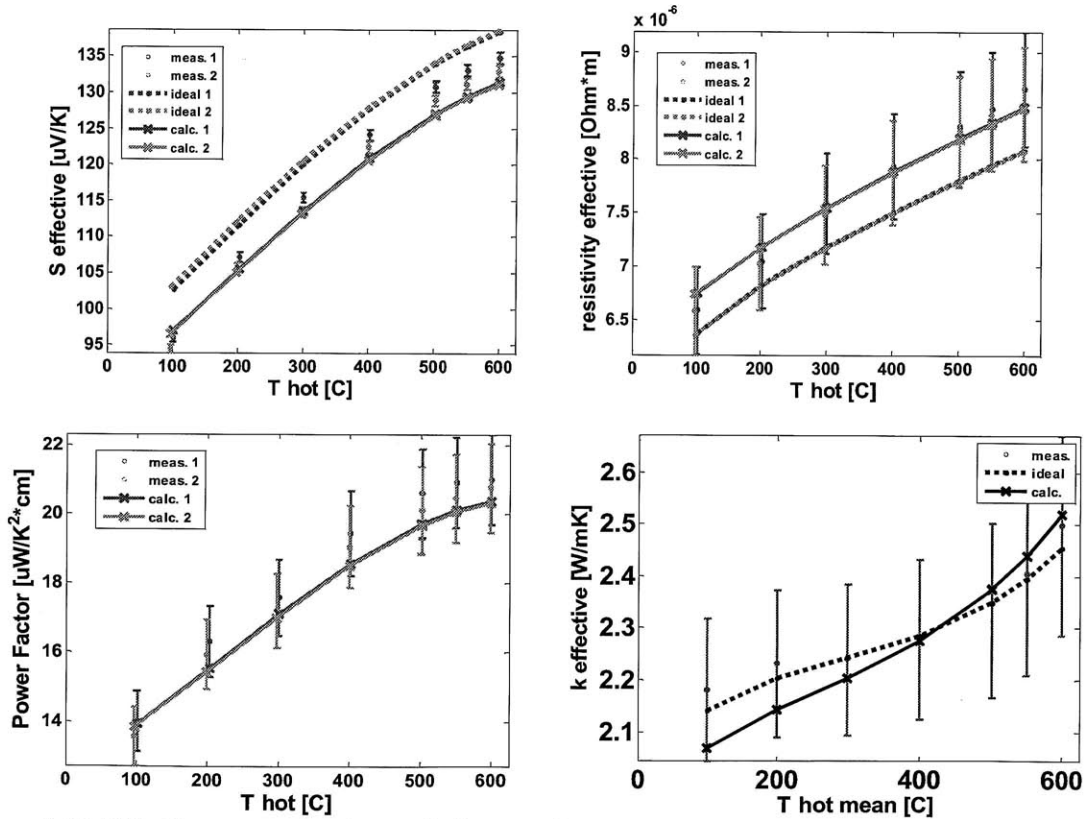


Figure 4-20: Effective properties P-type device samples. The “calc.” values include the full thermoelectric properties (individual property measurements), surface emissivity and geometry of both the skutterudite and electrodes between the measured temperatures. The “ideal” values are calculated from the individually measured properties of the skutterudite only and measured temperatures assuming there are no electrodes and no sidewall radiation.

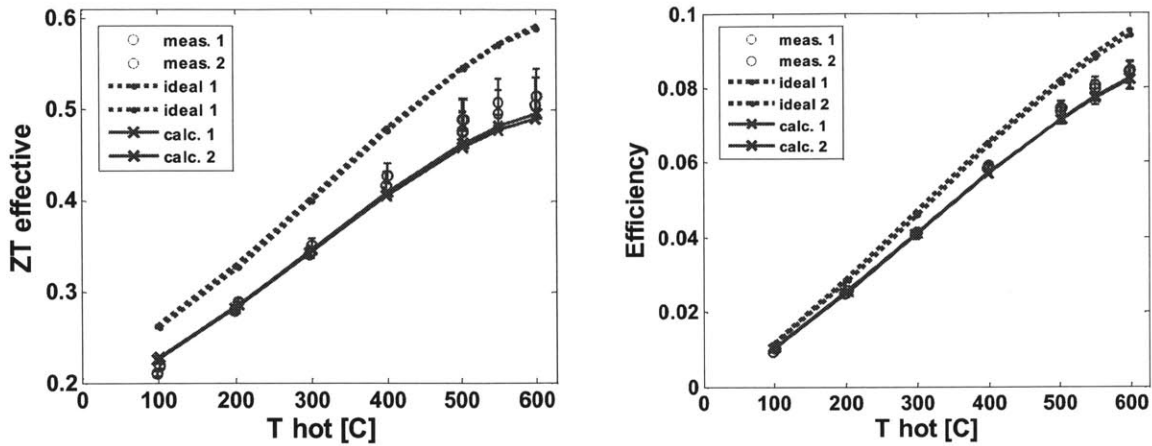


Figure 4-21: ZT_{eff} and corresponding maximum efficiency of the P-type device samples.

4.5.3 NP Efficiency

The power produced by each leg is equal to the voltage gain in the direction of current flow, times the current,

$$P_e = I \cdot V_{TE,N} + I \cdot V_{TE,P} \quad (4.6)$$

As previously mentioned, the thermoelectric voltage is measured between the thermocouples mounted on each electrode. The power is measured as if the electrodes were joined to each other with zero contact resistance and the parasitic electrical resistance at the heater assembly is separated from the measurement. The measured power and calculated power versus current are plotted in figure 4-23 for two different temperature ranges. In the higher temperature range the N and P-type legs operated between 558-559°C and 544-546°C, respectively, on the hot side and 58-63°C and 76-83°C on the cold side.* The maximum power produced was 0.445 W at 6 A. In the lower temperature range the N and P-type legs operated between 302-306°C and 295-298°C, respectively, on the hot side and 39-43°C and 48-54°C on the cold side. The maximum power produced was 0.114 W at 3.5 A. The power of the

* The thermal conductivity of Co_2Si (P-type electrode) is lower than CoSi_2 (N-type electrode) and thus the cold side temperature of the P-type was higher than the N-type.

individual legs peaked at very different current values, indicating that the geometry is not well matched to maximize the efficiency or power of the uncouple.

The heat entering the legs was measured in the same way as the effective properties with the addition of joule heating at the heater assembly,

$$Q_{Hot} = Q_{Hot,I=0} + I \cdot (V_{e1} + V_{e2}), \quad (4.7)$$

where V_{e1} , V_{e2} are the voltages between the electrodes and the heater. The measured efficiency is simply calculated as $\eta = P_e / Q_{Hot}$. The maximum measured efficiency in the lower and higher temperature range was 5.0% and 9.1% respectively. The thermal correction factor (Q_{loss} / IV_{heater}) was 12.5%, and the maximum uncertainty was 3.3%. The green triangles are for the case in which the heater was not thermally excluded from the measured result i.e. the thermal correction factor has not been applied. The purple stars are for the case that the heater assembly has not been excluded thermally or electrically. This is the efficiency if the voltage is measured between T_{c1} and T_{c2} and there is not correction for thermal losses.

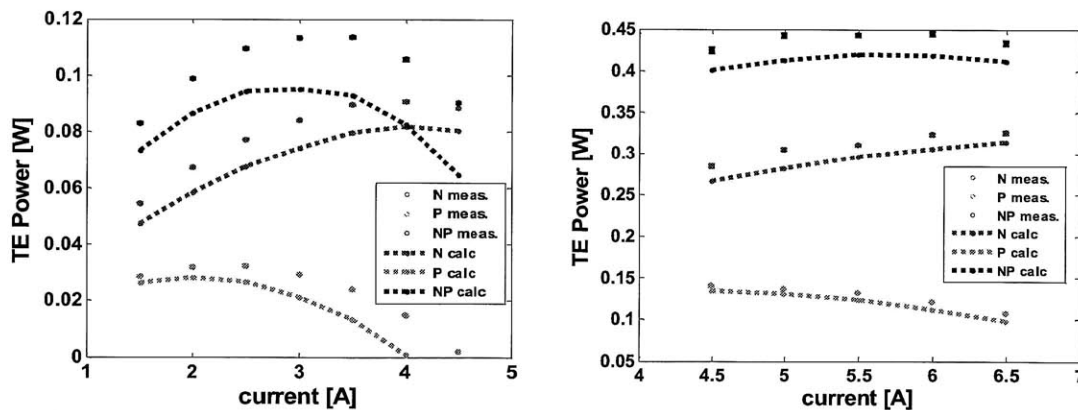


Figure 4-22: Thermoelectric power versus current for N-P couple. (left) The hot side temperature of the N and P legs were at 302-306°C and 295-298°C, respectively, and the cold side was at 39-43°C and 48-54°C. (right) The hot side temperature of the N and P legs were at 558-559°C and 544-546°C, respectively, and the cold side was at 58-63°C and 76-83°C.

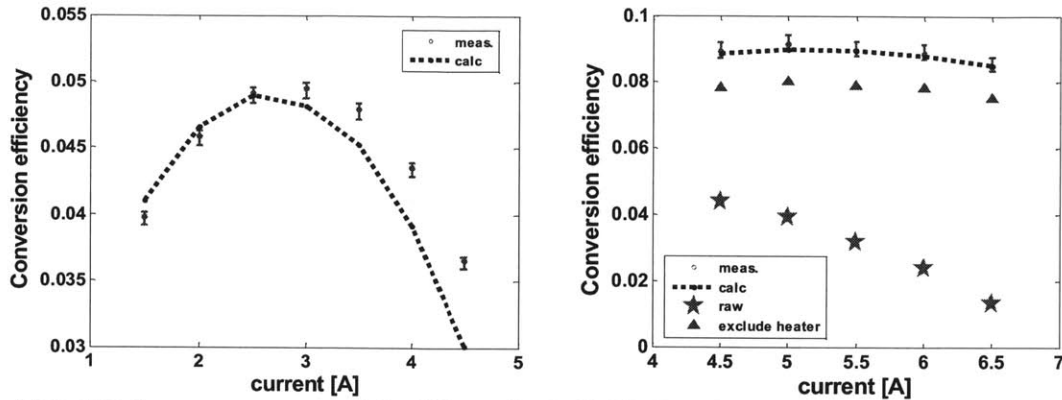


Figure 4-23: Efficiency versus current for NP couple. (left) The hot side temperature of the N and P legs were at 302-306°C and 295-298°C, respectively, and the cold side was at 39-43°C and 48-54°C. (right) The hot side temperature of the N and P legs were at 558-559°C and 544-546°C, respectively, and the cold side was at 58-63°C and 76-83°C. The “meas.” and “calc.” values are the final values after the heater section has been excluded thermally and electrically. The green triangles are the measured result if the heater assembly is not excluded thermally which is 12.5% lower. The purple stars are for the case that the heater assembly is not excluded thermally or electrically.

4.6. Accelerated Aging Tests

Thermoelectric generators are expected to operate for 10-20 years with little to no maintenance. We have already demonstrated a high ZT_{eff} with low contact resistance and short term stability in vacuum at 600°C for 44 hrs. The next characteristic to evaluate is the long term chemical stability of the legs.

There are several mechanisms of degradation/failure acting over long periods. Sb sublimation at high temperature is a well-studied problem in the literature. One solution is to coat the side walls of the legs with a dense metal film ($\sim\mu\text{m}$ thick) such as Ti, V, or to encapsulate the legs in Aerogel.^{24,26,48} The P-type contains Fe substituted for Co and as a result will oxidize rapidly in air at high temperature. Nanocomposites are in general an out-of-equilibrium material and there may be several mechanisms leading to degradation such as grain growth. These mechanisms are a well-known constraint for skutterudite material development and module design.

This section will characterize the chemical stability of our unique TE-electrode interface. A common mechanism of failure between two dissimilar metals is that the elements of each compound counter diffuse and an IMC (intermetallic compound) layer forms at the interface. Diffusing elements form unwanted phases, which have different thermal expansion coefficients and are brittle. Eventually as this layer grows in thickness the fractures can propagate long

distances and the whole contact fails. Zhao *et al.* joined Cu-Mo electrodes to skutterudites with a 100 μm thick bonding layer of Ti.^{*45-47,68} The samples were made by a direct bonding method using SPS. Accelerated aging experiments were performed by holding samples at 500, 525, 550, 575°C in an evacuated quartz tube for 0-30 days (figure 4-24). The IMC layer was composed of TiCoSb, TiSb₂ and TiSb. The thickness was measured in an SEM followed by an ultimate shear stress test. The IMC layer growth was modeled as a diffusion process with the thickness growing with the square root of time t , given by

$$Y = Y_0 + (Dt)^{0.5}, \quad (4.8)$$

where Y_0 is the initial thickness after press, and the diffusivity is modeled with an Arrhenius equation

$$D = D_0 + e^{(-Q/RT)}, \quad (4.9)$$

where Q is an energy barrier. After solving for the two constants with empirical data the thickness of the IMC layer could be solved for any arbitrary temperature-time history. They found that the ultimate shear stress decreased as the IMC layer grew, and at a thickness of 60 μm the electrode detached with no external force. Figure 4-25 shows an SEM micrograph of a failed IMC layer after 4 days at 600°C. However, because of the exponential relationship of the mass diffusion constant with temperature Zhao was able to show that at 500°C the joint will take more than 20 years to fail. Zhao's work was analyzed early in our project and we determined that the Ti bonding layer is too unstable and that we should search for a better solution.

* Ti is known to readily form diffusion bonds.

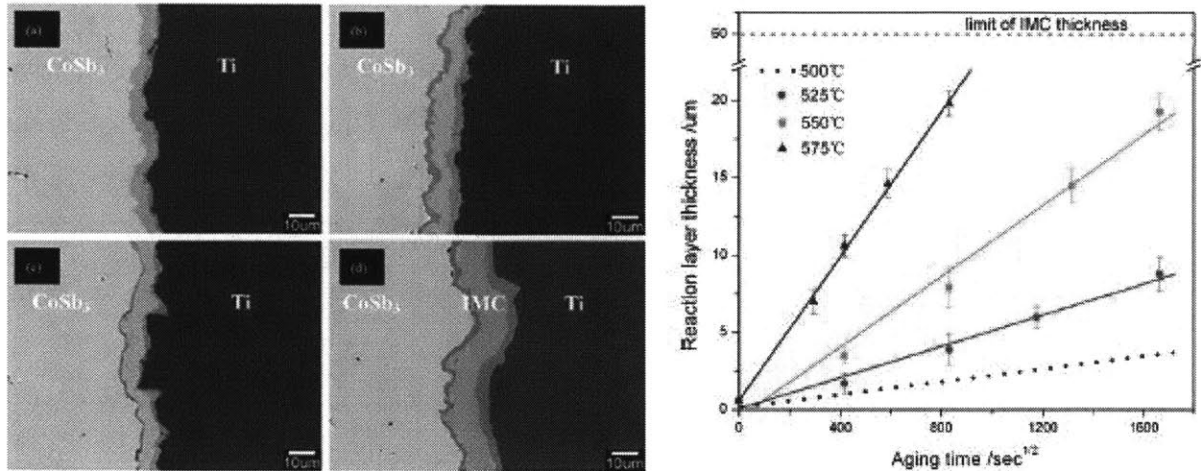


Figure 4-24: Results from accelerated aging studies in literature on a skutterudite-electrode system.⁴⁶ (left) SEM micrographs of IMC layer growth (right) Modeled as a diffusion process by an Arrhenius equation.

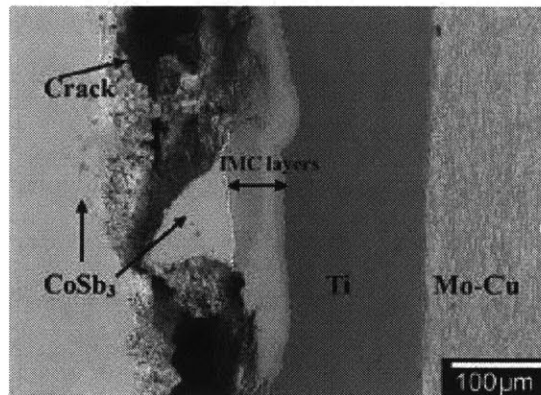


Figure 4-25: SEM micrograph of CoSb₃/Ti/Mo-Cu joint at 600°C for 4 days. This was done by Zhao.⁴⁶

We performed similar accelerated aging experiments followed by SEM microscopy and electrical contact resistance measurements. P-type device samples were held in a furnace at 605°C for 5 days and N-type BM device samples (made from BM powder not melt powder) were held at 605°C for 9 days in Ar95H₂5 (i.e. 95% Ar and 5% H₂) atmosphere. The size of the samples was on the scale of mm; the surfaces were cut and polished to remove surface oxides before inspection under SEM. Figure 4-26 and figure 4-27 show SEM images of the N and P accelerated aging samples compared to as-pressed samples from the same batch.

The original as-pressed N-type has a 3.5 μm thick layer of CoSi at the interface. There are many voids within the skutterudite and CoSi₂ indicating that full density has not been achieved in these samples. The measured contact resistivity was $<1 \times 10^{-10} \Omega \text{m}^2$. The aged N-type samples had virtually no void spaces in the skutterudites which is consistent with previous

observations of improved density and electrical conductivity after annealing. The CoSi layer at the interface was approximately the same thickness (5 μm) but with void spaces on either side. The void spaces gave rise to a large contact resistance of $3.5 \times 10^{-4} \Omega\text{m}^2$. Assuming the additional contact resistance was due only to void space we calculate that 0.9996 of the interface is now void space. However the bond was still mechanically strong enough to withstand polishing without detachment of the electrode. Our hypothesis is that voids spaces in the as-pressed skutterudite and electrode diffused to the interface. The driving force for diffusion would be that void spaces located at the relatively high energy interface lower the Gibbs free energy of the entire system. The void spaces at the interface must come either from the boundary of the sample or in the bulk. The fact that void spaces are longer seen in the bulk skutterudite is the main supporting evidence of this hypothesis. One concern is that SEM images were taken close to the boundary of the sample (at the polished surface) and may not be representative of the bulk, however the contact resistance measurement is a bulk average and confirms that there must be void space along the entire interface. Another sample measured for at 605°C for 5 days had a contact resistance of $2.6 \times 10^{-9} \Omega\text{m}^2$ and supports the diffusion mechanism of a contact resistance growing with time. If this hypothesis is true then the contact degradation can be slowed by producing a denser N-type, with less voids to begin with. Yet another hypothesis is that the void space may be caused by Sb evaporation which is known to be a common problem in skutterudites. For instance Co could diffuse to the CoSi_2 electrode creating the CoSi region and leaving behind an Sb rich region which evaporates and diffuses out through the boundary of the sample

The P-type samples exhibited a characteristically different degradation of the contact (figure 4-27). The as-pressed samples had a $35\mu\text{m}$ thick IMC layer containing undetermined compounds with the overall composition $\text{Co}_{61}\text{Si}_{27}\text{Sb}_{12}$. Diamond saw cutting striations are seen in the hard, dense, Co_2Si , and there are void spaces in the skutterudite. The aged sample has a larger IMC region of $137 \mu\text{m}$ with an overall composition of $\text{Co}_{61}\text{Si}_{29}\text{Sb}_{10}$.* There many chips due to polishing but no voids. Both the electrode and skutterudite appear fully dense.

* The IMC layer is big enough to see with the naked eye.

Figure 4-28 plots the electrical resistance versus length of the P-type as-pressed and aged samples. The contact resistance takes place over some length in the resistive IMC layer rather than at the interface as with the N-type. It is clearly seen by the shape of the resistance versus length across the IMC layer that it grows by a diffusion process. The initial P-type contact resistance did not fail catastrophically as in the case of the N-type forming voids, rather it degrades gradually over time. Evidence supports that both the N-type and P-type contact evolution can be modeled by an empirical fit to the diffusion equations given by eq.(3.3), (3.4). The P-type sample used in the device measurements previously described (figure 3-30) was pressed at a lower temperature and as a result has a thinner IMC layer.

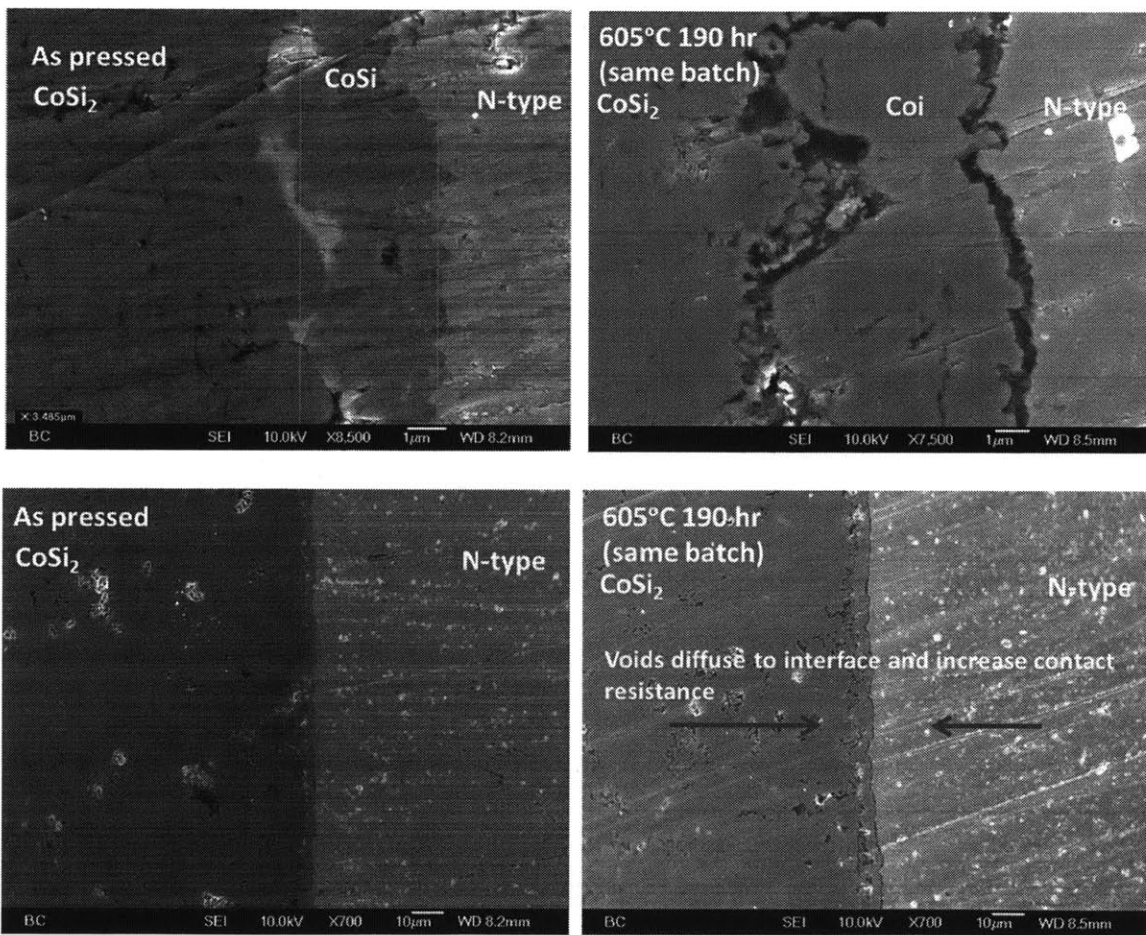


Figure 4-26: N-CoSi₂ before and after accelerated aging. (top left) High magnification as-pressed. (top right) Aged at 605°C for 190 hrs. (bottom left) Low magnification as-pressed. (bottom right) Low magnification aged at 605°C for 190 hrs. Dark spaces are void, light spaces are chip/particles at the surface.

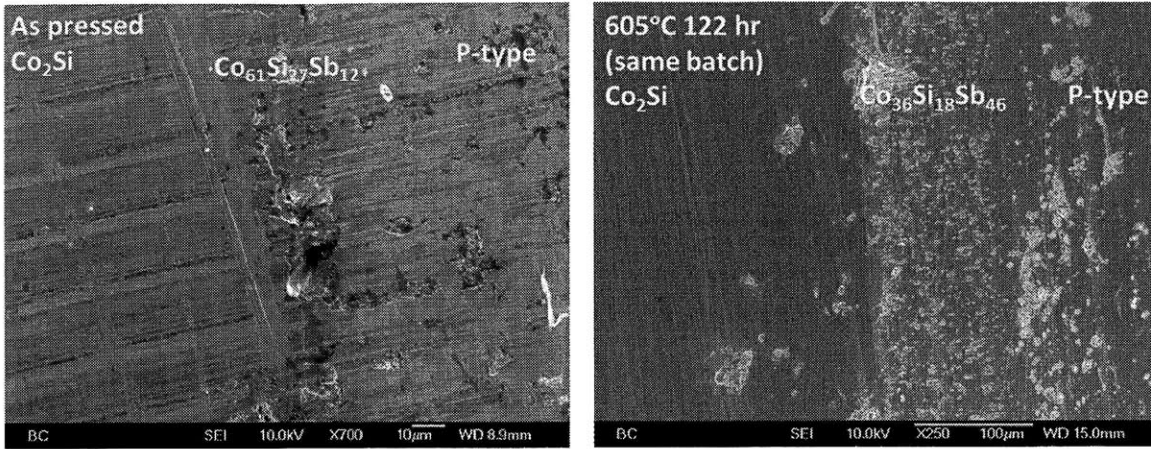


Figure 4-27: Co₂Si-P before and long duration high temperature exposure

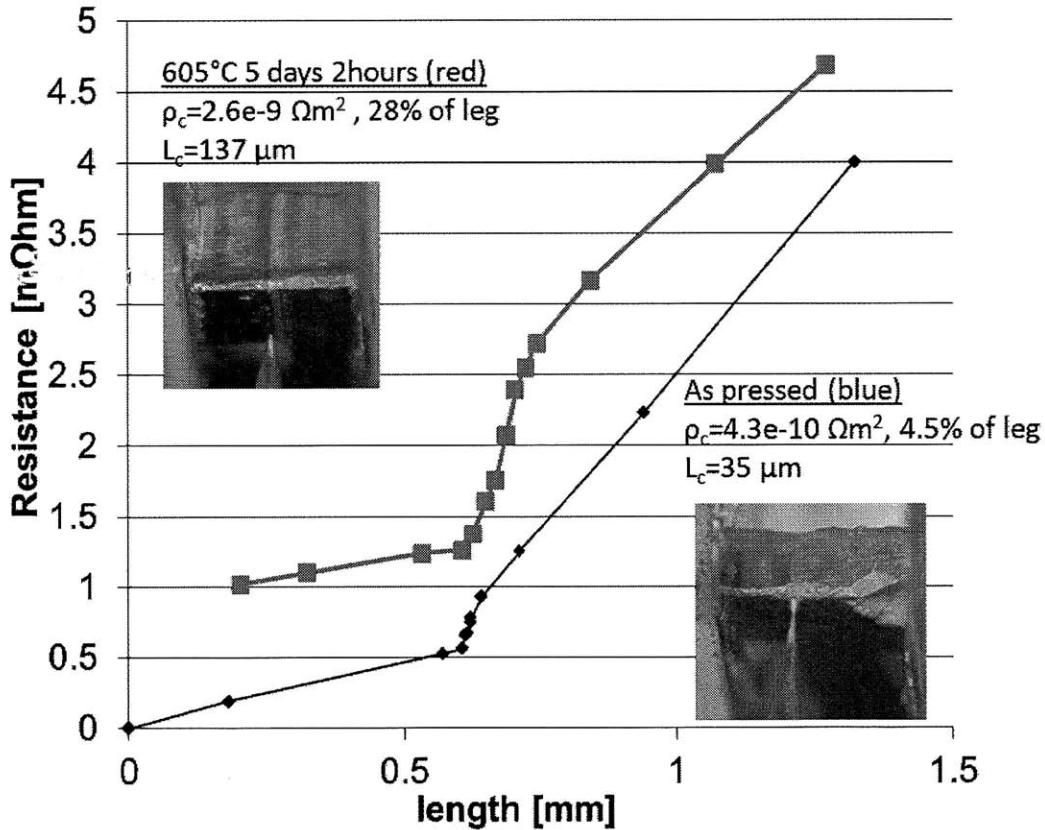


Figure 4-28: P-type electrical resistance versus length (blue line) as-pressed (red line) after accelerated aging at 605°C for 5 days.

Exposure to air at high temperature quickly degrades the bulk skutterudite and contact region, but not the bulk electrode. Figure 4-29 shows a photograph of an N-type device sample held at 605°C for 2 days in partial vacuum (10^{-1} Torr). The surface of the skutterudite is

discolored and flaking off, and the left contact has completely detached. This indicates that the air pressure was too high because this is not observed for device samples held in vacuum at 5×10^{-5} Torr. Hara *et al.* found that Sb reacts with oxygen to form multiple surface oxide layers (Sb_xO_y) that grow proportional to $time^{1/2}$.⁵² We hypothesize that the detachment of the electrode occurs because as oxygen fills the voids at the interface it forms Sb oxides which escalate deterioration of the contact. However this was not observed in the P-type device samples. Based on the known problems with oxidation and Sb sublimation in the bulk skutterudites and our observations of the contact, it is clear that a skutterudite module would have to be encapsulated slow these affects.

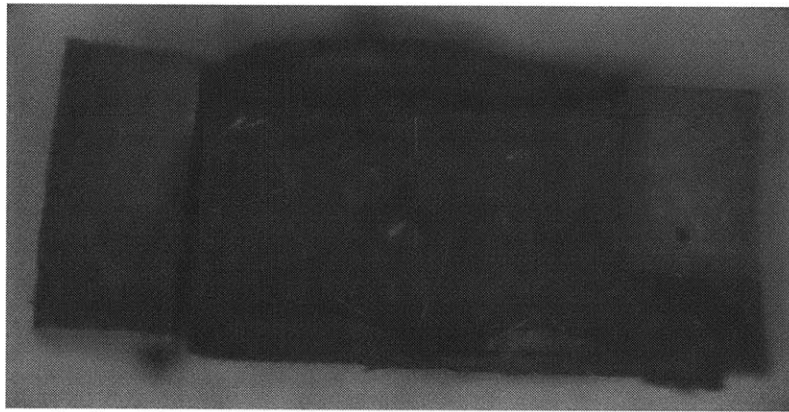


Figure 4-29: Photograph of an N-type device sample held at 605°C for 2 days in partial vacuum (10^{-1} Torr). The surface of the skutterudite is discolored and flaking off, and the left contact has completely detached.

4.7. Conclusions

In this work we developed a device testing system for a mid-temperature thermoelectric pair up to 600°C. There were a few challenges to developing the high temperature instrumentation. Small leg geometries were used in an inline configuration to reduce thermal stress and heat loss. A custom heater assembly was built and calibrated for heat losses. Thermocouples were attached each electrode with Ag epoxy which would become sintered Ag at high temperature. The accuracy of the measurement system was verified by measuring the absolute Seebeck of Pt wire over a 4.5 day period; the results showed excellent agreement with literature values. All measurements were taken between the hot can cold electrode of each leg such that the heater assembly was excluded both thermally and electrically. The testing method first measures the effective ZT of an N-N or P-P pair under open-circuit conditions. Then the efficiency of the N-P pair is measured directly as a function of current.

The ZT_{eff} and efficiency measurement was taken between the thermocouples and includes electrical contact resistance, and parasitic thermal/electrical resistance in the electrodes between the interface and thermocouples, and heat losses at the sides of the legs. Thus we have included all the parasitic loss effects that are present in a real unicouple. A module made from these device legs should be expected to perform nearly identical to what has been measured here. We demonstrated $Z\bar{T}_{\text{eff}} = 0.74$ for the N-type at 595°C corresponding to 11.7% conversion efficiency and $Z\bar{T}_{\text{eff}} = 0.51$ for the P-type at 600°C corresponding to 8.5% efficiency. The maximum efficiency of the NP sample was measured to be 9.1% at ~550°C and could be higher with the correct geometry of the legs. The efficiency values measured in this work are among the highest recorded for a skutterudite unicouple. Recall that Saber measured an efficiency of 10.35% for a skutterudite unicouple operating between 619°C and 43°C.²⁹ However this value assumes zero side heat losses and the authors do not give a good description of how the heater power was measured and corrected. We have progressed our skutterudites from a high ZT material into manufacturable legs ready for device prototyping.

Chapter 5. Solar Thermoelectric System Modeling

Solar thermal power generation is quickly becoming cost competitive for utility scale electricity with 380 MW electric currently installed.⁶⁹ Parabolic trough concentrators have proven economical and reliable but their efficiency is limited by the maximum temperature of the heated fluid. This work explores a solar thermoelectric topping cycle (STET) in which a thermoelectric generator (TEG) is added at high temperature to increase the overall efficiency of the system. In this design the perimeter of the receiver tube is covered with thermoelectrics so that the absorber temperature is raised and the energy rejected from the TEG is used to heat the fluid at its originally specified temperature. A heat transfer analysis was carried out to determine the overall system efficiency. A parametric study is performed to identify design constraints and put bounds on the total system efficiency.

The chapter begins with a background on the major components of state of the solar thermal system. We will introduce the STET concept and what changes would be made to the receiver in a parabolic trough system. The system was modeled using a one-dimensional heat transfer model that includes wavelength dependent radiation. The idealized receiver properties used in the simulation represent a practical limit of what could be achieved by a future receiver. The system performance was simulated for all conceivable concentrations and fluid temperatures of a solar thermal trough. As the absorber temperature increases more power is generated by the TEG but is offset by a rapidly decreasing absorber efficiency which results in only a marginal increase in net power. It is concluded that for the proposed STET to increase the system efficiency of a state of the art trough system by 10% requires a $Z\bar{T}_{eff}=3$ TEG, which is well beyond the state of the art in the field of thermoelectrics.

5.1. Introduction

Solar thermal plants consist of large arrays of collectors which concentrate solar radiation onto a receiver. Fluid flows through the receiver and is heated to a temperature high enough to generate steam that is then used in a Rankine cycle to generate electricity. Solar thermal is attractive for utilities because it uses conventional Rankine cycle turbo machinery, and offers the possibility of 6-15 hours thermal storage so that steam can be generated even during the night.⁷⁰⁻

⁷² The majority of existing solar thermal installations employ parabolic collectors because they are usually economically favorable over other collector types. Parabolic collectors can have an aperture width >5 m which focuses light onto to a tubular receiver (figure 5-1). The receiver consists of an outer glass tube and an inner metal tube carrying the heat transfer fluid, with diameters of 12 cm and 7 cm respectively. The inner tube is coated with a selective absorber surface, meaning that the surface has a high absorptivity α in the visible spectrum and a low emissivity ε in the IR spectrum. The annulus of the receiver is evacuated to eliminate air conduction and convection losses from the selective surface.



Figure 5-1: (left) Cartoon of a solar parabolic trough collector array. (middle) Photograph of a receiver tube. (right) Schematic, cross sectional view of the proposed receiver tube of the solar thermoelectric topping cycle.⁶⁹

A major factor limiting trough power plant efficiency is the maximum temperature of the heat transfer fluid which in most cases is oil and is stable up to 400°C^* . This work will explore the possibility of adding a STET within the receiver to increase the overall efficiency. In this design the perimeter of the receiver tube is covered by TE elements thus raising the absorber temperature (figure 5-1). The TEG converts heat to electricity at higher temperature before the heat is rejected to the fluid where it enters the Rankine cycle. In this way the fluid still reaches the same specified temperature and the operation of the solar Rankine cycle is left nearly unchanged. Thermoelectrics can uniquely accomplish this task because they are the only heat engine that can fit within the receiver tube geometry and are expected to last the lifetime of the receiver tube (10-20 years) with no maintenance. Thermoelectric generators can operate at temperatures up to 1000°C , however as the temperature of the absorber is raised the radiation

* The fluid is at a pressure of 10atm. The oil decomposed at t temperatures greater than 400°C .

losses increase as T^4 .^{*} In this analysis we'll solve for the optimal operating temperature to maximize the system efficiency.

5.1.1 Solar Flux and Receiver Geometry

The AM 1.5 direct solar spectrum (figure 5-2) is the appropriate spectrum to use for any solar thermal system with 1-D or 2-D tracking, and was used for all calculations in this chapter. Every solar thermal system consists of a collector and receiver. The collector is the optical system which concentrates the light and focuses it on the receiver, where the light is absorbed as heat. The theoretical maximum concentration of a 2-D line concentrating system is 215 suns.⁷³ However, the receiver in a real trough collector is round, so the maximum average concentration will be divided by π , yielding 68 suns. The concentrations quoted by collector systems can easily be misinterpreted, the following explains how to calculate the flux incident on the receiver. The geometric concentration C_{geo} , is the ratio of the aperture of the collector to the aperture of the receiver. The optical efficiency η_{opt} , is the ratio of the light incident on the receiver, to the light incident on the collector. The source of the losses include imperfect reflectance of the mirror, and geometric imperfections of the mirror and receiver due to mechanical deformation by static loads and wind loads. A trough concentrator may have $C_{geo} = 80$, and $\eta_{opt} = 0.8$ but since the receiver is round it should be divided by π to yield the actual concentration incident on the receiver,

$$C = \eta_{opt} C_{geo} / \pi = 20.4 \quad (5.1)$$

^{*} T^4 temperature dependence assumes a black body spectrum. Actually emission of the selective absorber is more complicated and is simulated in the following sections.

ASTM G173-03 Reference Spectra

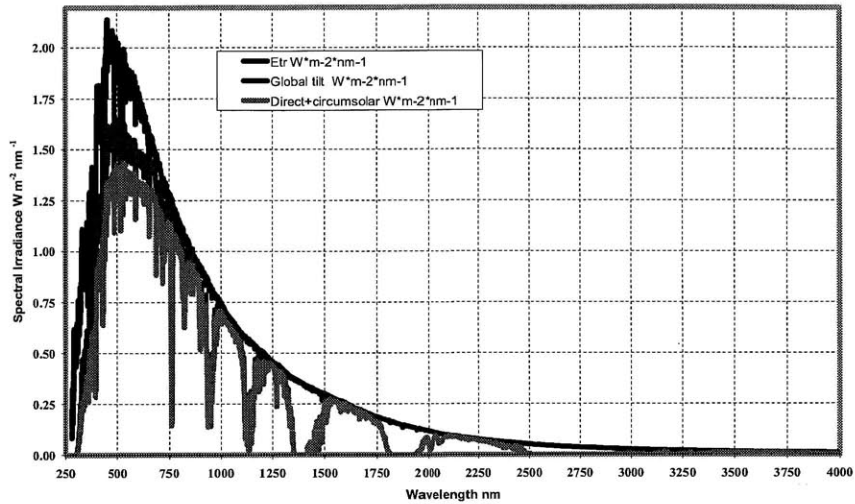


Figure 5-2: Solar spectra. The AM 1.5 direct spectrum (red) should be used for any solar thermal system with tracking and was used for all calculations in this chapter.

Figure 5-3 shows the flux distribution on a receiver tube in a state of the art parabolic trough collector. The experiment results show that the actual flux distribution is 3-D, non-uniform, with substantial reflections at the glass.⁷⁴ The calculated flux distributing along the perimeter of the tube is approximately Gaussian with a dip in concentration in the middle due to shadowing of the receiver tube.⁷⁴ Figure 5-3 shows that approximately 90% of the energy is located at an angle of 100-260 degrees from the vertical. In the proposed STET the TEG would be located along the bottom where the flux distribution is highest. The rest of the area would be covered by the original low temperature absorber at T_{fluid} which receives 10% of the energy. In this section we propose using a low temperature selective absorber, rather than a polished low emissivity metal because there is still significant solar flux to be absorbed.

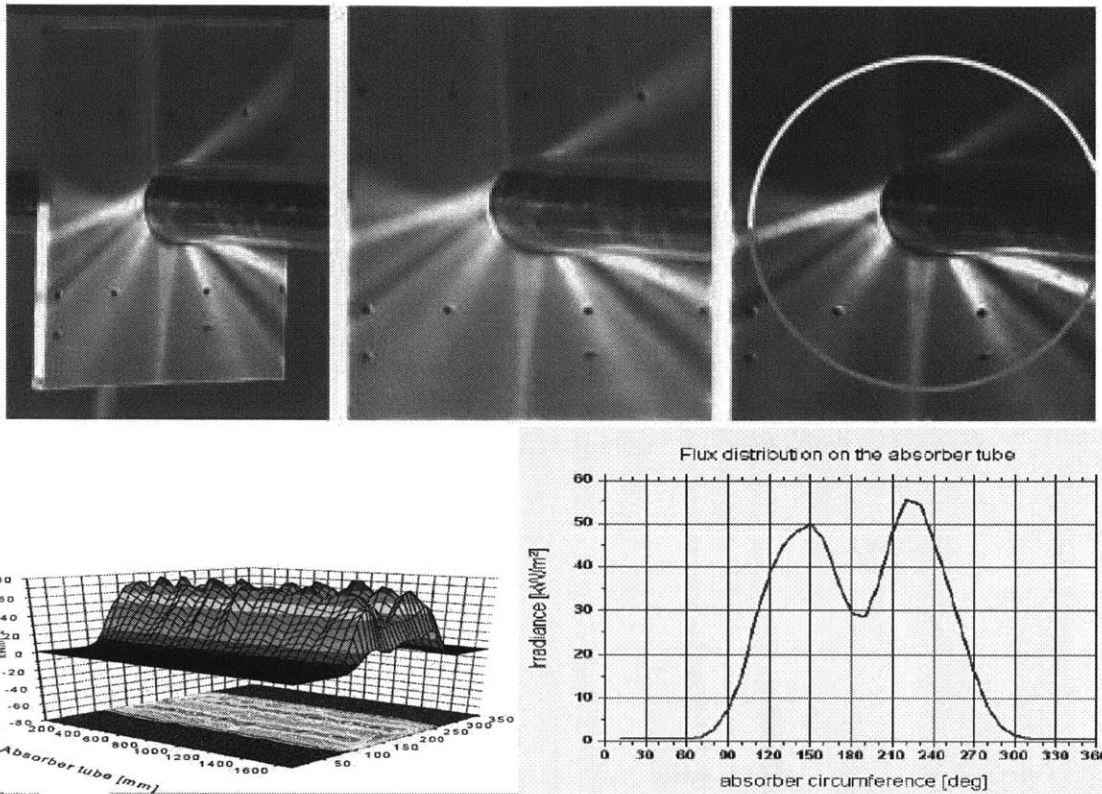


Figure 5-3: Concentrated solar flux distribution along a state of the art receiver tube. (right) Experimental results showing non uniform flux distribution and reflections at the glass.⁷⁴ (left) Calculated flux distribution from ray tracing using real geometry of the collector.⁷⁴

The emissive properties of the evacuated receiver are critical because thermal losses are dominated by radiative heat transfer. Figure 5-4 plots the solar spectrum, black body spectrum at 400°C, selective absorber properties, and glass properties of a state of the art receiver.⁷⁵ These values were the basis of the idealized receiver properties used in the rest of this work.

Figure 5-5 shows a schematic of an entire solar thermal trough system with thermal storage.⁶⁹ The proposed STET would only change the receivers in the solar field, the rest of the plant would remain the same. The inlet temperature of 248-293°C and outlet temperature of 307-393°C would also remain the same, although the flow rate of oil may change.

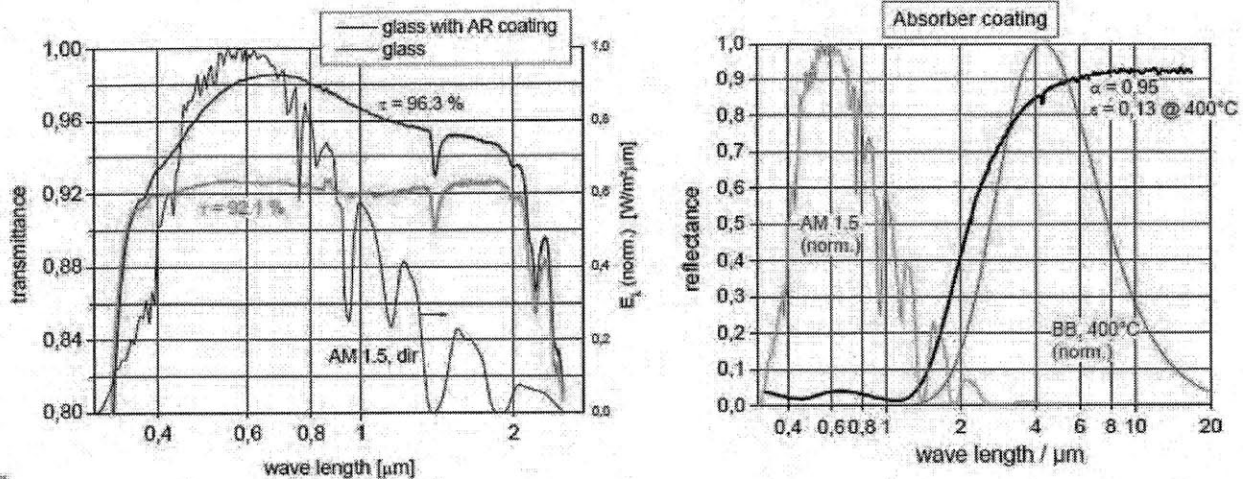


Figure 5-4: (left) Glass transmittance. (right) Selective absorber properties.⁷⁵

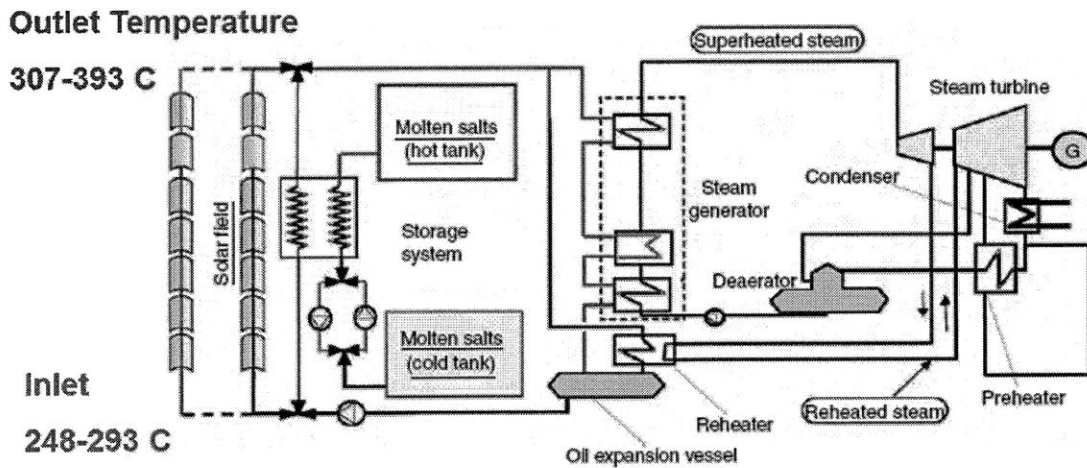


FIGURE 21.29 Scheme of a parabolic trough power plant with molten salt storage system.

Figure 5-5: Schematic of a solar thermal power plant with operating temperature range of the fluid.⁶⁹

5.2. 1-D Heat Transfer Model

In a real STET system the thermoelectric generator would only cover the bottom of the receiver tube where the concentrated solar flux is highest located (figure 5-6). However in this model we will assume the high temperature absorber and TEG surround the entire perimeter. These results can be extended to the case of partial coverage of the absorber tube but are not given here. In this work we consider a 1-D steady state model, solar radiation flux J_{solar} incident

on the collector is concentrated by a factor C , and focused onto the receiver tube. Light transmits through the glass and is absorbed as heat flux

$$q_{Abs} = \tau_{eff} \alpha_{eff} C J_{Solar}, \quad (5.2)$$

where τ_{eff} is the effective transmissivity of the glass receiver tube, and α_{eff} is the effective absorptivity of the selective surface. The selective surface is held at temperature T_{Abs} , and radiates heat flux q_{loss} to the environment. The annulus of the receiver tube is evacuated so we can neglect convection and air conduction. The heat fluxes q_{Abs} , q_{loss} are dependent on the emissive properties of the selective surface and will be calculated in the next section. The absorber efficiency is defined as

$$\eta_{Abs} = \frac{q_{Abs} - q_{loss}}{C J_{Solar}} = \tau_{eff} \alpha_{eff} - \frac{q_{loss}}{C J_{Solar}}, \quad (5.3)$$

and can also be interpreted as the thermal efficiency of the receiver. Obviously the absorber efficiency can be increased by decreasing the heat loss or increasing the collector concentration factor. The upper limit of efficiency is determined by the product of the effective transmissivity and the temperature-dependent effective absorptivity.

The net absorbed heat flux at the selective surface is conducted into the TEG where some of the energy is converted to work W_{TE} . At the cold side of the module heat flux q_{fluid} , is rejected to the fluid at temperature T_f , through a conduction and convection resistance. The Rankine cycle converts a fraction of q_{fluid} into work $W_{Rankine}$. The rest of the energy is rejected to the atmosphere at the condenser as $q_{condenser}$, at approximately ambient temperature, T_∞ .

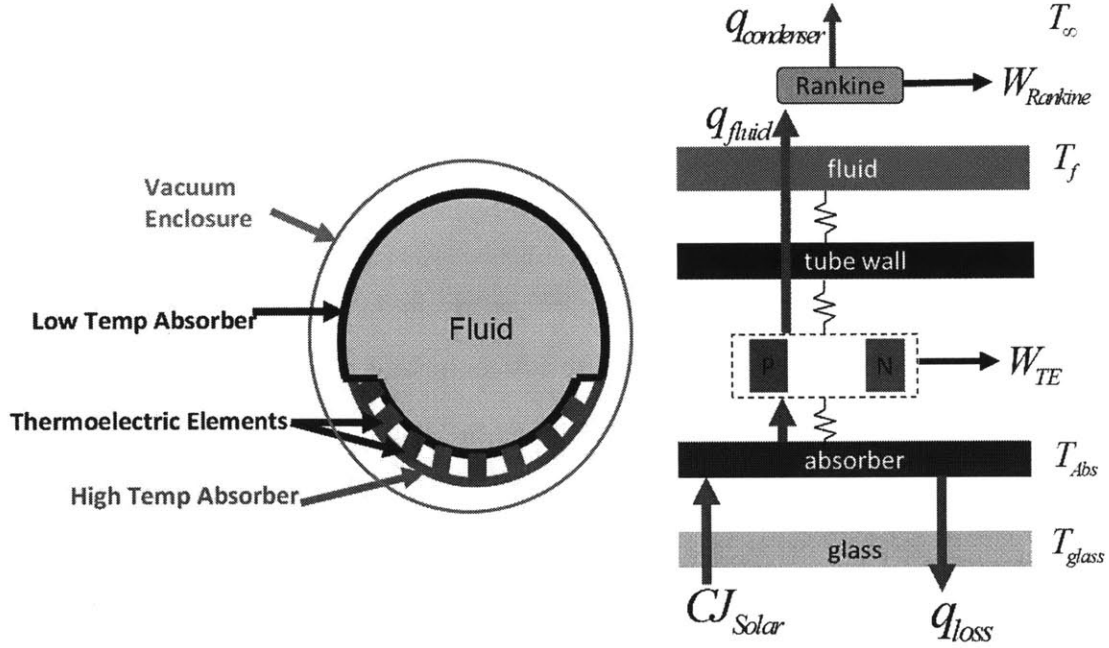


Figure 5-6: (left) A schematic of the STET receiver with thermoelectric elements lining the bottom perimeter where the highest intensity concentrated radiation is located. (right) A one-dimensional steady state model of the work and heat transfers of the STET. All thermal resistances are lumped into $Z\bar{T}_{eff}$.

The thermoelectric generator is modeled as a constant property material, for simplicity we will neglect all thermal resistances and assume they have been lumped appropriately into $Z\bar{T}_{eff}$. Therefore the TEG operates between T_{Abs} on the hot side and T_f on the cold side. We model the TE efficiency analytically using the well-known formula for maximum conversion efficiency⁴

$$\eta_{TE} = \frac{W_{TE}}{CJ_{solar}} = \eta_{Abs} \eta_{C,TE} \eta_{II,TE} = \eta_{Abs} \eta_{C,TE} \frac{\sqrt{Z\bar{T}_{eff} + 1} - 1}{\sqrt{Z\bar{T}_{eff} + 1} + T_f / T_{Abs}}, \quad (5.4)$$

where $\eta_{C,TE}$ is the Carnot efficiency and $\eta_{II,TE}$ is the second law efficiency, or fraction of Carnot. The second law efficiency is approximately constant with temperature, such that $Z\bar{T}_{eff} = 1, 2, 3$ corresponds to $\eta_{II,TE} \approx 0.20, 0.30, 0.37$ respectively, where $T_f = 300^\circ\text{C}$ and $T_{Abs} = 550^\circ\text{C}$. It is important to realize that this formula gives an upper limit estimate on the efficiency and it is not a function of the material geometry. The conversion efficiency of the Rankine cycle is written as

$$\eta_{Rankine} = \frac{W_{Rankine}}{CJ_{solar}} = \eta_{C,Rankine} \eta_{II,Rankine} (\eta_{Abs} - \eta_{TE}), \quad (5.5)$$

where $\eta_{C,Rankine}$ is the Carnot efficiency of the Rankine cycle operating between T_f and T_∞ . The second law efficiency of the Rankine cycle $\eta_{II,Rankine} = 0.65$, was computed from literature values of efficiency and operating temperatures of existing solar thermal power plants.⁶⁹ The high second law efficiency of the Rankine cycle is what makes this cycle dominant at large scales. This would be equivalent to a $Z\bar{T}_{eff} = 15.5$ material, therefore thermoelectrics are never expected to replace Rankine cycles as the primary heat engine. Finally we solve for the total efficiency

$$\eta_{sys} = \frac{W_{Rankine} + W_{TE}}{CJ_{solar}} = \eta_{TE} + \eta_{Rankine} \quad (5.6)$$

Given the fluid temperature, concentration level, and selective surface properties we then solve for the optimal absorber temperature which maximizes the system efficiency. When deciding whether to use a STET we must compare the system efficiency using a conventional receiver to a receiver with a thermoelectric generator installed. In both cases the concentration level and fluid temperatures are the same. We compare the original system efficiency without a STET, $\eta_{without}$, where $T_{Abs} = T_{fluid}$ to the system efficiency with a STET $\eta_{with TE}$, where $T_{Abs} > T_{fluid}$. There are two relevant figures of merit, the first is the relative increase in power or power ratio

$$P_{ratio} = \frac{\eta_{with TE}}{\eta_{without}} = \frac{\eta_{Abs}}{\eta_{Abs,Tf}} \left(1 + \eta_{C,TE} \eta_{II,TE} \left(\frac{1}{\eta_{C,Rankine} \eta_{II,Rankine}} - 1 \right) \right) = A_{ratio} HE_{ratio} \quad (5.7)$$

The first term is called the absorber ratio A_{ratio} , it represents the loss in efficiency from increasing the absorber temperature. It is always less than unity and will be calculated in the next section. The second term in brackets is called the heat engine ratio HE_{ratio} , it represents the relative

increase in power from adding a lossless TEG as a topping cycle to a Rankine cycle. The second figure of merit is the overall increase in efficiency or efficiency gain

$$\eta_{gain} = \eta_{with\ TE} - \eta_{without} = \eta_{without} (P_{ratio} - 1) \quad (5.8)$$

As T_{Abs} increases, HE_{ratio} increases, and A_{ratio} decreases, thus there will be an optimal T_{Abs} to simultaneously maximize both the power ratio and efficiency gain. Figure 5-7 plots η_{gain} and HE_{ratio} versus T_{Abs} and T_f for a $Z\bar{T}_{eff} = 1$ TEG paired with a perfect receiver with no thermal losses.

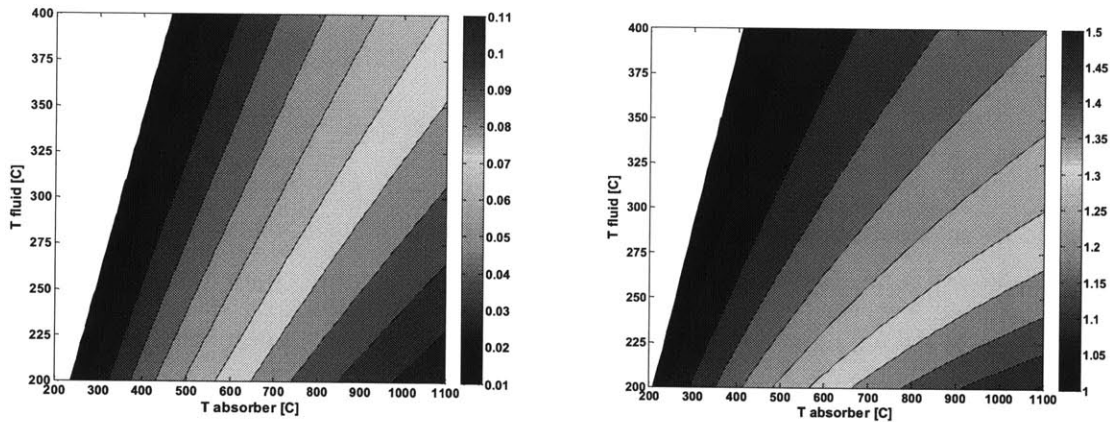


Figure 5-7: Thermoelectric topping cycle performance of a $Z\bar{T}_{eff}=1$ material, neglecting all thermal losses from the receiver. (left) Efficiency gain vs. fluid temperature, and absorber temperature. (right) Heat engine ratio vs. fluid temperature and absorber temperature. Contour increments are 0.05.

5.3. Selective Absorbing Surface

The selective surface is a critical component to the STET because this is where the most important model assumptions are made. A selective absorber is designed to have a high emissivity at short wavelengths to strongly absorb the solar spectrum and a low emissivity at longer wavelengths to reduce blackbody emission. The emissivity should transition sharply at a wavelength appropriate for the operating temperature. High temperature selective absorbers are made from layers of ceramics filled with metal particles called cermets.⁷⁶ These materials must be stable at high temperature in vacuum or air and are expected to operate for ~20 years.

Selective surfaces are an important enabling technology for the solar thermal industry and are an active area of research.

Figure 5-8 plots the solar intensity versus wavelength at 40x concentration and black body emission at temperatures of 400-700°C by increments of 50°C. The properties of the selective surface are modeled by having a high absorptivity of $\alpha=0.96$ at short wavelengths and transitions sharply to a low emissivity of $\varepsilon=0.05$ at long wavelengths (figure 5-8). We assume that this idealized surface can be engineering for any transition wavelength λ_T , to optimize the total system efficiency. The optimal transition wavelength is a function of the absorber temperature and concentration and is located approximately where the solar spectrum and the blackbody emission intersect. The absorptivity was based on a practical engineering limit of what has been achieved by selective surfaces in literature (figure 5-4). The emissivity is based on the practical lower limit of a polished metal surface. The step-function transition at any transition wavelength is the theoretical best transition. The glass tube is modeled as having a high transmissivity of $\tau=0.963$ for short wavelengths and then transitions to completely opaque at 2700 nm with an emissivity of $\varepsilon_{glass} = 0.89$ at long wavelengths. The glass properties were based off the properties given in figure 5-4.⁷⁵ The intensity of the solar spectrum beyond 2500nm is negligible therefore the glass is highly transparent to the solar spectrum and we approximate $\tau_{eff} \approx \tau$. These selective surface properties represent the practical engineering limit of a high performance material that is not available today but may be feasible in the future. The idealized receiver is a favorable assumption for the STET and also simplifies calculations.

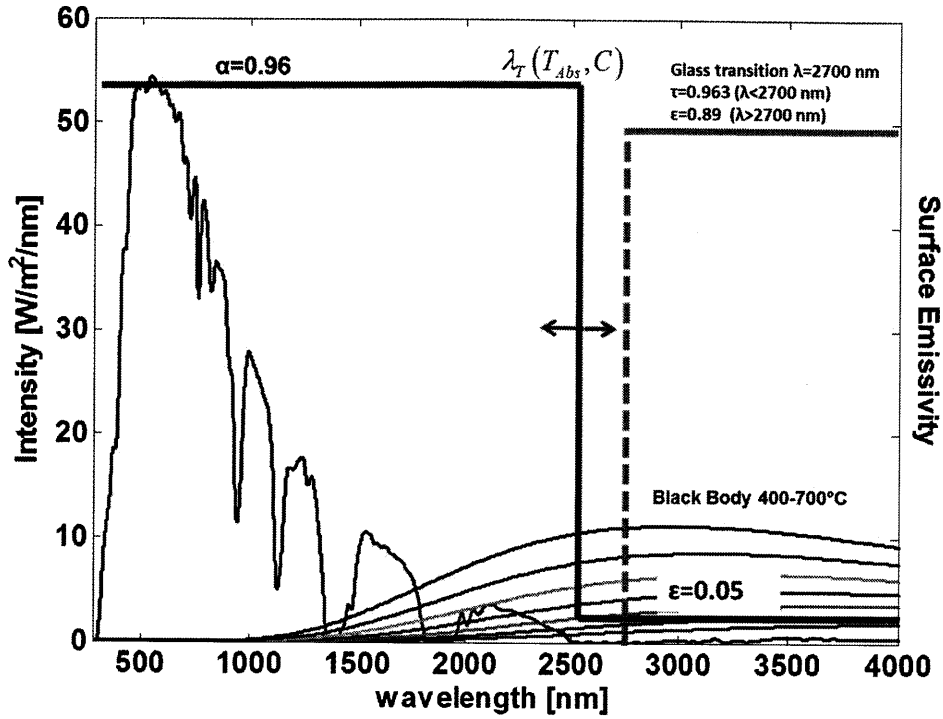


Figure 5-8: Solar spectrum at 40x concentration (blue). Schematic representation of the selective surface properties (red) and glass tube properties (grey).

In general the emissivity ε'_λ , is a function of wavelength and angle. In this analysis we assume Lambertian emission and ignore the angular dependence. The subscript “eff”, represents an effective emissive property that is a function of temperature. The following conventions are used for the radiative heat flux calculations. It is convenient to define the integrated solar heat flux over a given bandwidth

$$S_1(\lambda) = \int_0^\lambda d\lambda' I_{Solar, \lambda'} , \quad (5.9)$$

$$S_2(\lambda) = \int_\lambda^\infty d\lambda' I_{Solar, \lambda'} , \quad (5.10)$$

$$J_{Solar} = \int_0^\infty d\lambda' I_{Solar, \lambda'} = S_1(\lambda) + S_2(\lambda) , \quad (5.11)$$

the units are in W/m^2 . Figure 5-9 plots $S_1(\lambda)$ and $S_2(\lambda)$. The total hemispherical black body thermal emission at a given temperature is represented by $I_{b,\lambda}(T)$, in units of $\text{W}/\text{m}^2\text{nm}$. Integrating over a given bandwidth we define

$$B_1(\lambda, T) = \int_0^\lambda d\lambda' I_{b,\lambda'}(T), \quad (5.12)$$

$$B_2(\lambda, T) = \int_\lambda^\infty d\lambda' I_{b,\lambda'}(T), \quad (5.13)$$

$$J_b(T) = \int_0^\infty d\lambda' I_{b,\lambda'}(T) = B_1(T) + B_2(T) = \sigma_{sb} T^4, \quad (5.14)$$

where σ_{sb} is the Stephen-Boltzmann constant. For convenience we use the dimensionless black body spectral distribution function

$$F(\lambda T) = \frac{\int_0^\lambda d\lambda' I_{b,\lambda'}(T)}{\int_0^\infty d\lambda' I_{b,\lambda'}(T)} = \frac{B_1(\lambda, T)}{J_b(T)}. \quad (5.15)$$

The tabulated values are commonly found in radiation texts.⁷⁷ Once $\lambda_T(C, T_{Abs})$ is specified, then the effective emissive properties can be found. The thermal emission and effective emissivity of the selective surface are given as

$$q_{emitted} = (\alpha F(\lambda_T T_{Abs}) + \varepsilon (1 - F(\lambda_T T_{Abs}))) J_b(T_{Abs}), \quad (5.16)$$

$$\varepsilon_{eff} = \frac{q_{emitted}}{J_b} = \alpha F(\lambda_T T_{Abs}) + \varepsilon (1 - F(\lambda_T T_{Abs})) = (\alpha - \varepsilon) F(\lambda_T T_{Abs}) + \varepsilon. \quad (5.17)$$

Similarly the effective absorptivity is written

$$\alpha_{eff} = \frac{\alpha S_1(\lambda_T) + \varepsilon S_2(\lambda_T)}{J_{Solar}} . \quad (5.18)$$

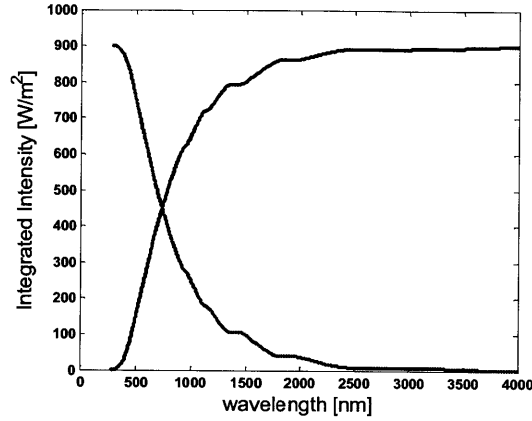


Figure 5-9: Integrated solar intensity versus wavelength, $S_1(\lambda)$ in blue, $S_2(\lambda)$ in green.

5.4. Thermal Losses

The thermal losses of the receiver were calculated by a 1-D steady state heat transfer model with radiation and convection. The system is represented schematically in figure 5-10 as a radiative network between the absorber surface, glass, and ambient. Note that the radiative network also has a convection term between the glass tube and ambient. The total receiver heat flux loss contains four terms and is an implicit equation that is solved numerically,

$$q_{loss} = q_{transmit} + q_{Abs \rightarrow glass} = q_{transmit} + q_{glass \rightarrow \infty} + q_{convection} . \quad (5.19)$$

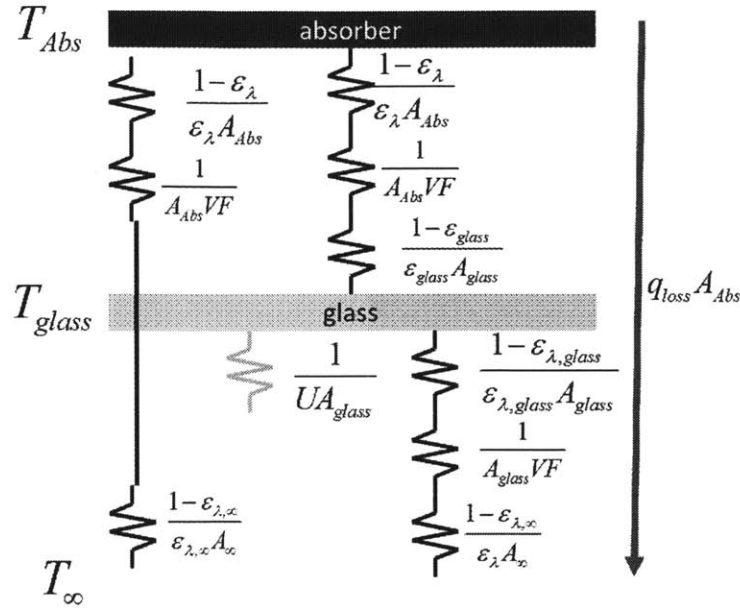


Figure 5-10: 1-D Radiative heat transfer network of the receiver, used to calculate the thermal loss. The thermal emission spectra is split into two regimes. The resistance in yellow is a convection resistance.

The radiative spectrum is split into two wavelength ranges. In the first regime $\lambda < \lambda_{glass}$ and the glass is highly transparent so most of the radiation transmits straight through to the environment. The transmitted radiation is calculated by the following integral

$$q_{transmit} = \int_0^{\lambda_{glass}} d\lambda \epsilon_{\lambda} \tau_{eff} (I_{b,\lambda}(T_H) - I_{b,\lambda}(T_{\infty})) \left[\alpha F(\lambda_T T_{Abs}) + \epsilon (F(\lambda_{glass} T_{Abs}) - F(\lambda_T T_{Abs})) \right] \tau_{eff} J_b(T_{Abs}) \quad (5.20)$$

where we have made the approximation that $I_{b,\lambda}(T_{\infty}) \ll I_{b,\lambda}(T_H)$. The factor of τ_{eff} accounts for a single reflection, additional reflections were neglected. The glass has been approximated as a non-absorbing medium, which is not valid if IR reflective coatings are used. In the second wavelength range for $\lambda > \lambda_{glass}$ the glass is opaque. The heat flux from the selective absorber to the glass is given by

$$q_{Abs \rightarrow glass} = \int_{\lambda_{glass}}^{\infty} d\lambda \frac{I_{b,\lambda}(T_{Abs}) - I_{b,\lambda}(T_{glass})}{\frac{1-\epsilon_{\lambda}}{\epsilon_{\lambda}} + 1 + \frac{1-\epsilon_{\lambda,glass}}{\epsilon_{\lambda,glass}} \frac{A_{Abs}}{A_{glass}}} = \frac{(1-F(T_{Abs}, \lambda_{glass})) J_B(T_{Abs}) - (1-F(T_{glass}, \lambda_{glass})) J_B(T_{glass})}{\frac{1-\epsilon}{\epsilon} + 1 + \frac{1-\epsilon_{glass}}{\epsilon_{glass}} \frac{A_{Abs}}{A_{glass}}}, \quad (5.21)$$

where $\varepsilon_{glass} = 0.89$ is the emissivity of the glass receiver tube for wavelengths greater than λ_{glass} . The heat flux has been normalized to the area of the absorber for convenience; since the coordinate system is cylindrical the term A_{Abs}/A_{glass} shows up to correct for the different radii. The radiative flux in the long wavelength range from the glass to the environment is given by

$$q_{glass \rightarrow \infty} = \varepsilon_{glass} \frac{A_{glass}}{A_{Abs}} \int_{\lambda_{glass}}^{\infty} d\lambda (I_{b,\lambda}(T_{glass}) - I_{b,\lambda}(T_{\infty})) = \varepsilon_{glass} \frac{A_{glass}}{A_{Abs}} \left((1 - F(\lambda_{glass}, T_{glass})) J_b(T_{glass}) - (1 - F(\lambda_{glass}, T_{\infty})) J_b(T_{\infty}) \right). \quad (5.22)$$

A correlation was used to solve for the heat transfer coefficient by natural convection at the outside of the glass tube,

$$Nu_D = .36 + \frac{.518 Ra_D^{1/4}}{\left(1 + (.559 / Pr)^{9/16}\right)^{4/9}}, \quad (5.23)$$

where Pr is the Prantl number and Ra_D is the Rayleigh number. The convected heat flux is given by

$$q_{convection} = U(T_m) \frac{A_{glass}}{A_{Abs}} (T_{glass} - T_{\infty}). \quad (5.24)$$

With each term defined in the q_{loss} balance, the equation was solved iteratively to find T_{glass} for a given T_{Abs} and λ_T .

5.5. Transition Wavelength and Solar Spectrum AM 1.5 direct

The transition wavelength λ_T , should be chosen at the value that maximizes the absorber efficiency (Eq.(4.3)) for a specified concentration and temperature. The optimal λ_T was

approximated by the solution for a receiver that is perfectly transparent in the range $\lambda > \lambda_T$. This approximation is very close to the actual solution, and simplifies computations. The following equation was maximized to find the corresponding optimal transition wavelength

$$\eta'_{Abs} = \frac{q_{Abs} - q'_{loss}}{q_{sun}} = \frac{\tau\alpha CS_1(\lambda_T) - \tau\alpha B_1(\lambda_T, T_{Abs}) - \varepsilon B_2(\lambda_T, T_{Abs})}{CJ_{solar}} \quad (5.25)$$

Figure 5-11 plots the optimal transition wavelength for a solar thermal system with a defined concentration and absorber temperature. Under practical limits of concentration and temperature the solution converges to 2 choices: 2500nm or 1800nm. Due to large absorption bands in the solar spectrum, the intersection with the black body spectrum tends to happen near two wavelengths. For example, we can see that the optimal transition wavelength at 400°C is about 2500 nm but when we increase the temperature to 700°C there is significant overlap between the two spectra and the transition is now at 1800nm. This means that the last hump of the solar spectrum, which contains 3.5% of the total power, cannot be absorbed by the STET.

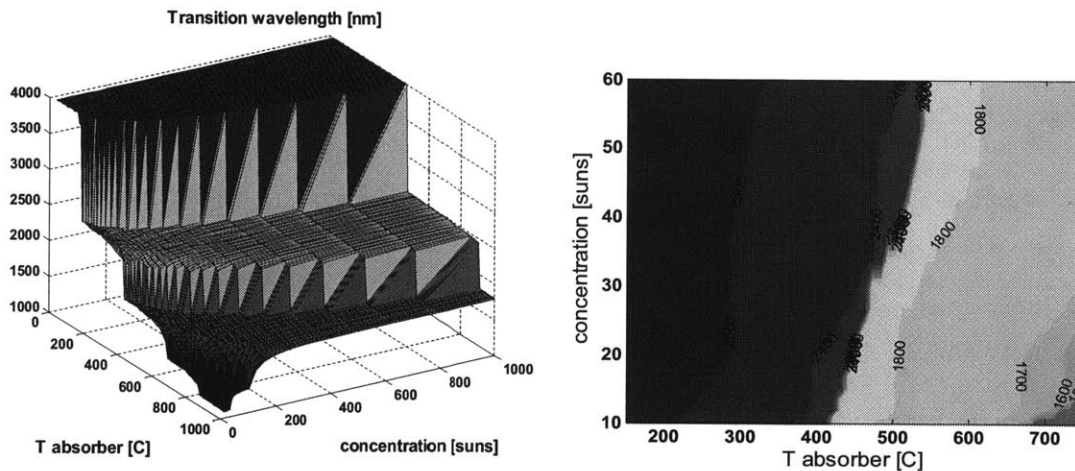


Figure 5-11: Transition wavelength versus absorber temperature and concentration. (left) A broad view of solar thermal operating space with absorber temperatures ranging from 50-1000°C and concentrations from 1-1000. (right) The operating concentrations and temperatures of a conceivable line concentrator. For all practical solar thermal trough operating conditions the solution converges to two transition wavelengths: 1800nm and 2500nm.

5.6. Results and Discussion

The receiver heat losses were calculated as a function of temperature and transition wavelength $q_{loss}(T_{Abs}, \lambda_T)$. Since $\lambda_T(T_{Abs}, C)$ then we can also plot the optimal $q_{loss}(T_{Abs}, C)$, which corresponds to the maximum absorber efficiency (figure 5-12). As T_{Abs} increases from 400°C to 750°C the absorber efficiency decreases at a faster rate due to increased radiation losses (figure 5-12). Since $\lambda_T < \lambda_{glass}$ then the glass temperature is only a function of T_{Abs} . Figure 5-13 plots T_{glass} versus T_{Abs} corresponding to the maximum absorber efficiency. Radiation losses were the dominant mode of heat transfer, convection at the glass surface accounted for 16-22% of q_{loss} .

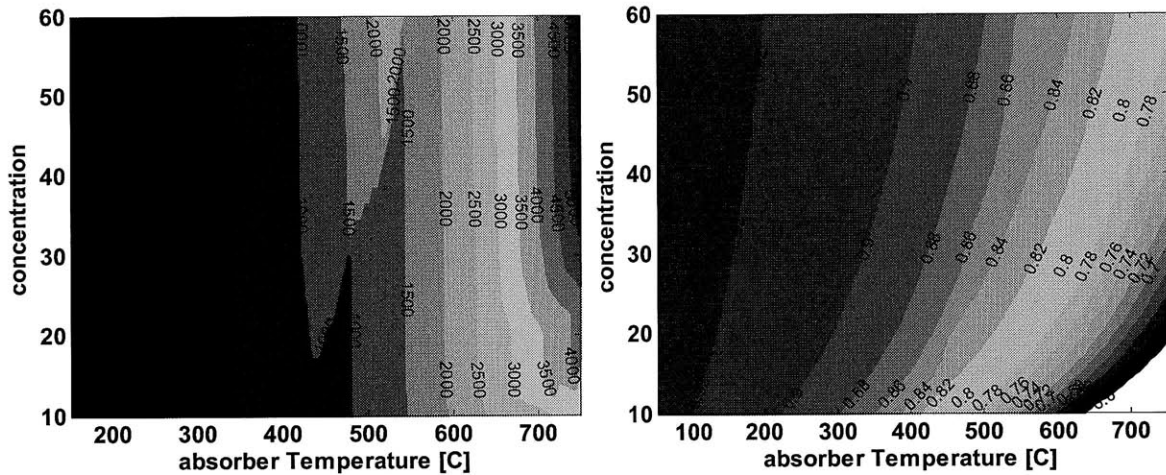


Figure 5-12: (left) Receiver heat flux loss at optimal transition wavelength (right) Maximum absorber efficiency.

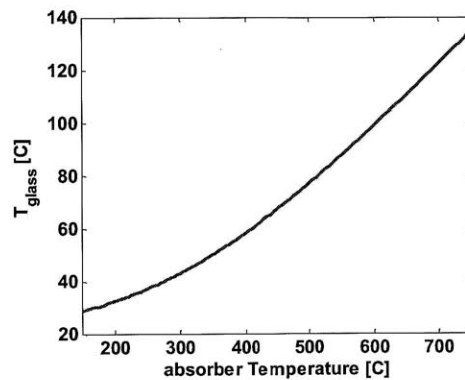


Figure 5-13: Glass temperature versus absorber temperature.

The theoretical maximum average concentration of a two-dimensional line concentrating system with a tubular receiver is 68 suns.⁷³ The contour plots in this section all have concentrations from 10-60 suns on the vertical axis and fluid temperature from 150-500°C on the horizontal axis. Any conceivable solar thermal trough system should operate within the region defined by these axes. The current state of the art trough systems have concentrations of 20-25 suns and fluid temperatures of 300-400°C, this region is outlined by the black box in each of the figures. We assert that the STET should offer at least 10% greater power in order to justify the engineering costs of adding a TEG to the receiver. Therefore systems with $P_{ratio} \geq 1.1$ are good candidates for a STET, while systems with $P_{ratio} \leq 1.1$ are not justified. Figure 5-14a shows that the power ratio for a state of the art trough with a $Z\bar{T}_{eff}=1$ thermoelectric material is less than 5%. Therefore currently available thermoelectric materials with $Z\bar{T}_{eff} \approx 1$ should not be applied. Figure 5-14b shows that the power ratio for a state of the art trough with a $Z\bar{T}_{eff}=3$ material is >1.1 for $T_f \approx 300^\circ\text{C}$. This means that for a system with fluid entering the solar array at $T_f = 300^\circ\text{C}$ and exiting at $T_f = 400^\circ\text{C}$ the receivers near the inlet should be outfitted with the STET while the receivers near the exit should not. Figure 5-14c and figure 5-14b show that we should expect $\eta_{gain} \approx 3$ percentage points and $T_{Abs} \approx 550^\circ\text{C}$ for a STET with a $Z\bar{T}_{eff}=3$ module. STET systems at $T_f = 300\text{-}400^\circ\text{C}$ require a high $Z\bar{T}_{eff}$ material for two reasons: 1) The steam Rankine cycle is already very efficient. 2) For $T_{Abs} > 400^\circ\text{C}$ the black body spectrum begins to significantly overlap with the solar spectrum (figure 5-8), λ_T moves from 2500 nm to 1800 nm and 3.5% of the solar spectrum is lost. One can simply evaluate the case of using a partial coverage high temperature by looking at the higher concentration results. For example, instead of an average 20-25x concentration as defined by the dotted black box in figure 5-14, the high temperature absorber may have an effective 40x concentration in which the results are slightly better. The situation improves for systems with lower fluid temperatures such as for the organic Rankine cycle solar thermal trough proposed by Hassani and Price⁷⁸ which would operate between $T_f = 173\text{-}304^\circ\text{C}$. However, to the authors' knowledge, no utility scale solar thermal troughs have yet been built in this temperature range.

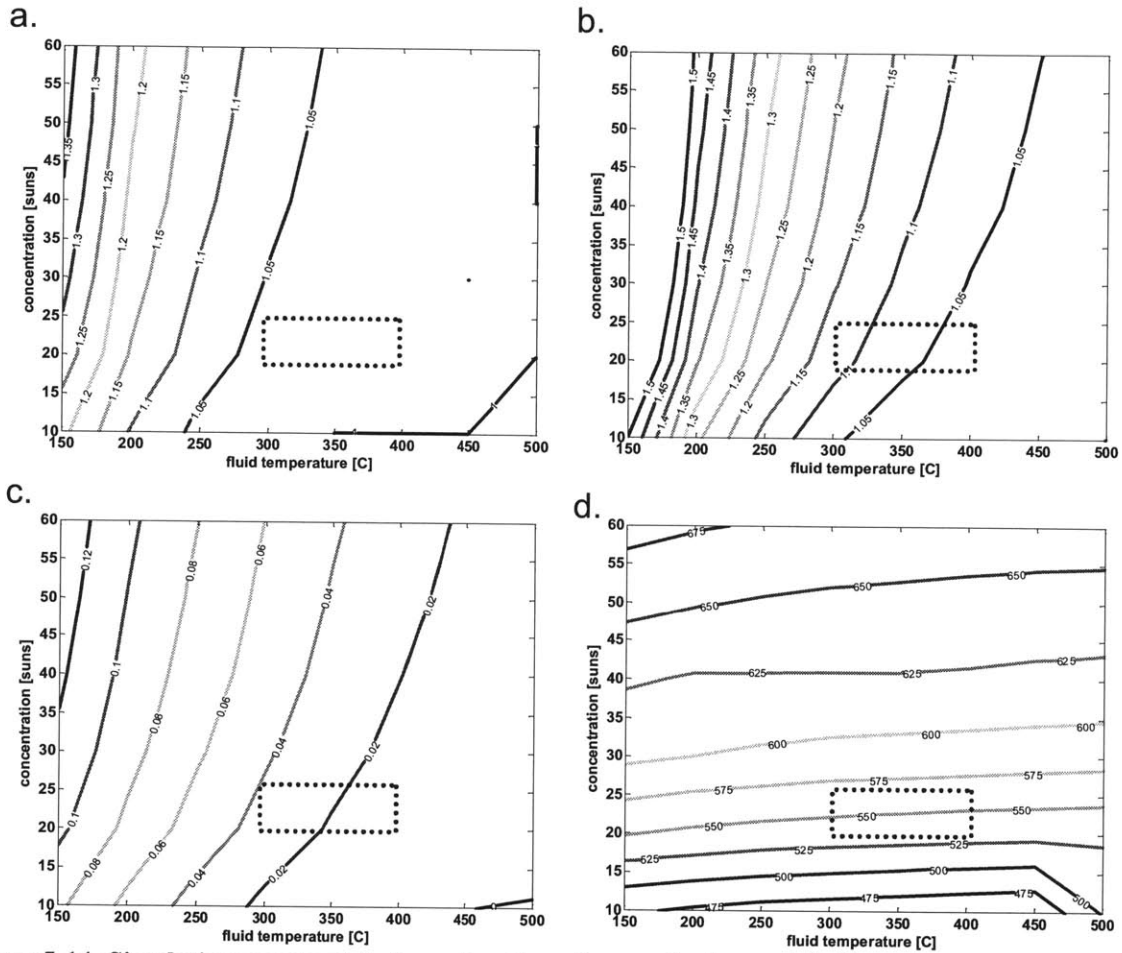


Figure 5-14: Simulation results plotted as a function of concentration and fluid temperature the black box represents the current state of the art solar troughs a) power ratio, $ZT_{\text{eff}}=1$ b) power ratio, $ZT_{\text{eff}}=3$ c) efficiency gain, $ZT_{\text{eff}}=3$ d) optimal absorber temperature, $ZT_{\text{eff}}=3$.

5.7. Conclusions

The authors have proposed a solar thermoelectric topping cycle (STET) to increase the efficiency of solar thermal parabolic trough power plants. The system was modeled using a one-dimensional heat transfer model that includes wavelength dependent radiation. The idealized selective absorber surface is modeled as having $\alpha=0.96$ for $\lambda < \lambda_T$ and $\varepsilon=0.05$ for $\lambda > \lambda_T$. The idealized receiver properties represent a practical limit of what could be achieved by a future receiver, and is a favorable assumption for the STET. The system performance was simulated for all conceivable concentrations and fluid temperatures of a solar thermal trough. As the absorber temperature increases more power is generated by the TEG but is offset by a rapidly decreasing absorber efficiency which results in only a marginal increase in net power. It was

concluded that for the proposed STET to increase the system efficiency of a state of the art trough system by 10% requires a $Z\bar{T}_{eff}=3$ TEG, which is well beyond the state of the art in the field of thermoelectrics. The current trend of utility scale parabolic troughs is to increase fluid temperatures which is even less favorable for the STET. However solar thermal power is a rapidly developing field, and in the future there may be other opportunities for the STET within solar thermal trough collectors at lower fluid temperatures using organic Rankine cycles.

In a real STET system the high temperature absorber would cover about 44% of the perimeter of the absorber tube and still receive 90% of the power (figure 5-3) and the average concentration of the high temperature absorber would be higher. A more complete description of the heat transfer at the receiver would require a 2D or 3D model with diffuse and specular reflection. The performance should also be simulated on a daily or yearly time scale instead of solar noon. Also a current dependent thermoelectrics model with real material properties and geometry could be implemented. Each of these features had been incorporated into the model to some extent but in the end they resulted in a less favorable outcome for the STET. The 1-D model presented here was enough to support the conclusion that the utility scale parabolic trough is not a good near term application for thermoelectrics.

There may be other systems within solar thermal that TEGs can play a role. A cogeneration system that produces heat and electricity for district heating in buildings or industrial heat applications may be promising. A potential favorable scenario for STEGs would be if it became economical and popular to have 3-D concentrators capable of 100's of suns, on roof tops of buildings for cogeneration. This scenario would provide high absorber efficiency from high concentrations and TEs could offer a good option as a low maintenance, primary heat engine.

Chapter 6. Summary and Recommendations for Future Work

It is convenient to conceptually break up thermoelectrics research into three domains: materials research, device testing, and applications. Over the years research in the materials stage has produced a new materials and processing techniques to increase ZT. However progress is slow and the community has been hurt from false claims of high ZT material systems. The field needs more robust experimental techniques that firmly establish where the state of the art truly is. This thesis focused on the last two thermoelectric research stages: device testing and applications. Chapter 2 describes the development of a novel device testing method to be used in the room temperature range, up to 230°C. A mathematical method was derived to extract the intrinsic properties from the device properties. The technique measures all three TE properties of a single leg, in the same direction, with significantly less uncertainty than other methods. The measurements include the effects of temperature dependent properties, side wall radiation, and contact resistance. The power and efficiency were directly measured and are within 0.4 % and 2 % of the values calculated based on the property measurements. This work was the foundation for the following chapters.

Chapters 3 and 4 were the main contributions to this thesis. Skutterudite device samples were fabricated by a direct bonding method in which a rigid electrode is sintered directly to the TE powder during press. Compatible electrode materials were identified and evaluated based on thermal stress, parasitic electrical/thermal resistance, chemical stability and ease of prototype fabrication. The final electrodes solutions were Co_2Si with the P-type and CoSi_2 with the N-type. The direct hot press process was modified into what we call a hybrid hot press to produce device samples with strong bonds and no cracks. Preliminary accelerated aging tests were conducted to evaluate the long term chemical stability of the TE-electrode contacts. The TE-electrode combinations meet all the criteria for device testing and offer a practical, manufacturable solution for module construction.

The ZT_{eff} and efficiency measurement was taken between the thermocouples and includes electrical contact resistance, and parasitic thermal/electrical resistance in the electrodes between the interface and thermocouples, and heat losses at the sides of the legs. Thus we have included all the parasitic loss effects that are present in a real uncouple. A module made from these

device legs should be expected to perform nearly identical to what has been measured here. We demonstrated $Z\bar{T}_{eff} = 0.74$ for the N-type at 595°C corresponding to 11.7% conversion efficiency and $Z\bar{T}_{eff} = 0.51$ for the P-type at 600°C corresponding to 8.5% efficiency. The maximum efficiency of the NP sample was measured to be 9.1% at ~550°C and could be higher with the correct geometry of the legs. The efficiency values measured in this work are among the highest recorded for a skutterudite unicouple.

Figure 6-1 describes the overall plan for bringing skutterudites from a high ZT material through the device testing stage in which a module is built and tested. The sections in yellow have been accomplished in Chapters 3 and 4 while the other sections should be regarded as future work. The skutterudites device legs developed here offer a viable solution for small scale production in the near term. The HHP process is reliable and it is possible to make high performance device legs by this recipe that can be used for device prototyping. A brazing technique should be developed to join the high temperature electrodes to enable unicouple devices and modules. Finite element modeling should be used to guide the design of unicouple/module fabrication. Material development should proceed concurrently with device prototyping. The mechanical properties of each sample should be measured along with the thermoelectric properties to gain fundamental understanding. Currently there is large uncertainty in the CTE measurements which must be explained. Accelerated aging studies on the TE-electrode electrical contact resistance should continue to fully characterize the degradation mechanisms. There are several methods to reduce Sb sublimation (side wall metallization, aerogel encapsulation, etc.) that must be investigated.

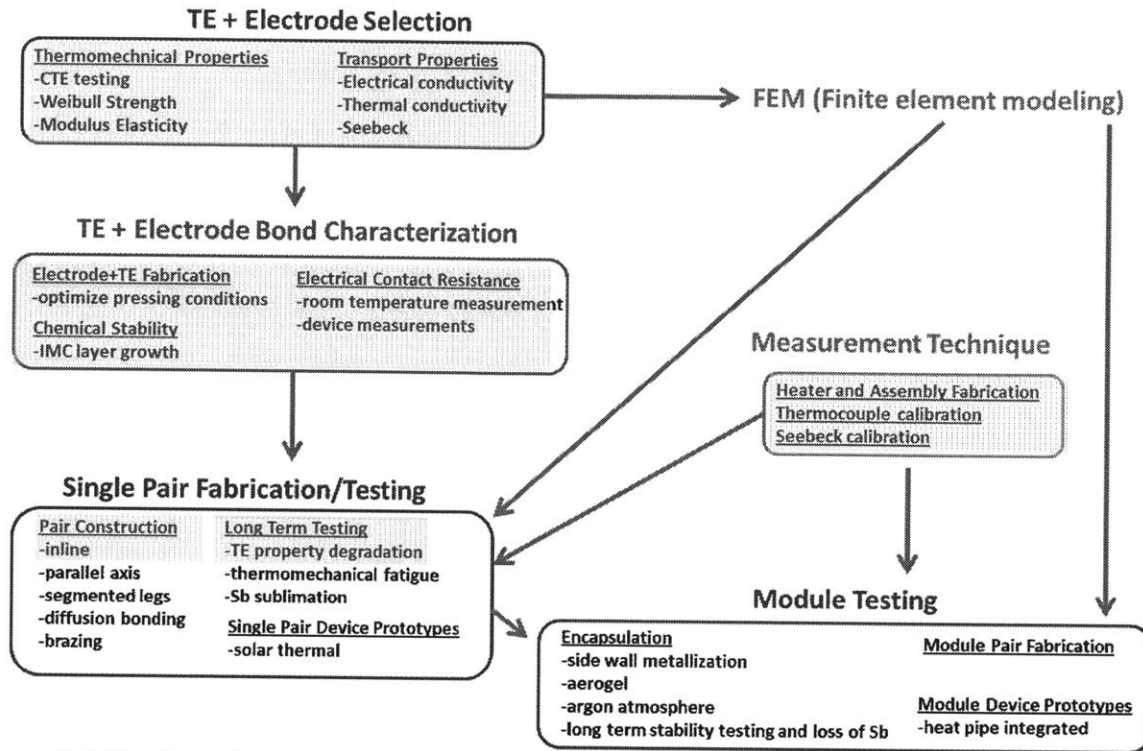


Figure 6-1: Roadmap from skutterudite material characterization to electrode selection device testing and module testing. The bullets highlights in yellow have been accomplished in this thesis while the others are future work that should be performed in the future.

In Chapter 5 we proposed a solar thermoelectric topping cycle (STET) to increase the efficiency of solar thermal parabolic trough power plants. A parametric study was performed to analyze the efficiency of the new proposed system. The system was modeled using a one-dimensional heat transfer model that includes wavelength dependent radiation. The idealized receiver properties represent a practical limit of what could be achieved by a future receiver, and is a favorable assumption for the STET. The effective ZT formulation that was applied successfully in Chapter 2 on an experimental basis was now used to model thermoelectric performance within the STET system. The system performance was simulated for all conceivable concentrations and fluid temperatures of a solar thermal trough. As the absorber temperature increases more power is generated by the TEG but is offset by a rapidly decreasing absorber efficiency which results in only a marginal increase in net power. It was concluded that for the proposed STET to increase the system efficiency of a state of the art trough system by 10% requires a $Z\bar{T}_{eff} = 3$ TEG, which is well beyond the state of the art in the field of thermoelectrics. The corresponding hot side temperature for this hypothetical high ZT material

is $\sim 550^{\circ}\text{C}$ which corresponds to the temperature range of skutterudites. The solar industry is rapidly changing, and there may be other systems within solar thermal that TEGs can play a role. A cogeneration system that produces heat and electricity for district heating in buildings or industrial heat applications may be promising. A potential favorable scenario for STEGs would be if it became economical and popular to have 3-D concentrators capable of 100's of suns, on roof tops of buildings for cogeneration. This scenario would provide high absorber efficiency from high concentrations and TEs could offer a good option as a low maintenance, primary heat engine.

The field of thermoelectrics has continued to grow over the period of this thesis work. Researchers from other fields have become more aware of the progress in thermoelectrics and more companies have engaged in thermoelectrics R&D. The increased popularity is despite thermoelectrics having any well established power generation applications. Researchers are now not only hunting for high ZT materials but they are also carefully studying their thermomechanical properties. This indicates that researchers are closer to implementing these systems. People often ask "how high must ZT be for thermoelectrics to take off?" At $Z\bar{T}_{eff} = 3$ thermoelectrics can compete with vapor compression cycles on efficiency alone, which obviously represents a huge market. In the authors opinion, a low cost, $Z\bar{T}_{eff} = 2$ device would enable wide spread implementation of thermoelectrics in many systems.

Appendix

A: Radiation Correction

The following will derive the radiation correction terms used in Chapter 2. Integrating Eq.(2.4) once with respect to x gives

$$kA \frac{dT}{dx} + \frac{I^2}{A} \int_0^x \rho dx' - I \int_{T_H}^T \tau dT' - \varepsilon \sigma_{sb} P \int_0^x (T^4 - T_\infty^4) dx' + C_1 = 0 \quad (A. 1)$$

where $\tau = T \frac{d\alpha}{dT}$ is the Thompson coefficient and C_1 is a constant of integration. We integrate a second time with respect to x and apply the boundary conditions $T|_{x=0} = T_H$ and $T|_{x=L} = T_C$ to solve for the integration constants

$$-kA \frac{dT}{dx} = \frac{I^2}{A} \int_0^x \rho dx' - I \int_{T_H}^T \tau dT' - \varepsilon \sigma_{sb} P \int_0^x (T^4 - T_\infty^4) dx' - \frac{A}{L} \int_{T_H}^{T_C} k dT + \frac{\varepsilon \sigma_{sb} P}{L} \int_0^L \int_0^x (T^4 - T_\infty^4) dx' dx - \frac{I^2}{LA} \int_0^L \int_0^x \rho dx' dx + \frac{I}{L} \int_{T_H}^{T_C} \int_{T_H}^T \tau dT' dT \quad (A. 2)$$

After rearranging terms we solve for the temperature gradient at the hot side

$$-kA \frac{dT}{dx} \Big|_{T_H} = \frac{A}{L} \int_{T_C}^{T_H} k dT + \frac{\varepsilon \sigma_{sb} P}{L} \int_0^L \int_0^x (T^4 - T_\infty^4) dx' dx - I^2 R \left(\frac{\int_0^L \int_0^x \rho dx' dx}{L \int_0^L \rho dx} \right) - I \beta \left(\frac{\int_{T_H}^{T_C} \int_{T_H}^T \tau dT' dT}{L \int_{T_H}^{T_C} \tau dT} \right) \quad (A. 3)$$

where $\tau = T \frac{d\alpha}{dT}$ is the Thompson coefficient. If we assume that the quantities in the parenthesis are approximately equal to $1/2$, then we can apply this result to Eq.(2.2) to derive Eq.(2.12).

Applying $I=0$ results in Eq.(2.6) which is composed of a heat conduction term and a radiation term given by

$$Q_{rad} = \frac{\varepsilon\sigma_{sb}P}{L} \int_{T_c}^{T_H} \int_T^{T_H} \frac{(T'^4 - T_\infty^4)}{\frac{dT'}{dx} \frac{dT}{dx}} dT' dT \approx \frac{\varepsilon\sigma_{sb}PL}{\Delta T^2} \int_{T_c}^{T_H} \int_T^{T_H} (T'^4 - T_\infty^4) dT' dT \quad (A. 4)$$

This is the additional hot side heat transfer at $x=0$ due to side wall radiation. We integrate the radiation along the length of the leg to solve for the total side wall radiation loss

$$Q_{rad,side} = \varepsilon\sigma_{sb}P \int_{T_H}^{T_c} \frac{(T^4 - T_\infty^4)}{\frac{dT}{dx}} dT \approx \frac{\varepsilon\sigma_{sb}PL}{\Delta T} \int_{T_c}^{T_H} (T^4 - T_\infty^4) dT \quad (A.5)$$

Both radiation quantities have been approximated by assuming a linear temperature gradient.

B: Uncertainty Analysis

The following uncertainty analysis applies for the device measurements of Chapter 2 and Chapter 4. The total uncertainty in an arbitrary P has contributions from the following sources:

- DAQ(Data Acquisition): Offset, Gain, Noise, Tempdrift
- Model: from assumptions made by the mathematical model such as geometry
- Environment: noise, non-equilibrium/non-steady state

In our experiments the $\text{Offset}_{\text{DAQ}}$, $\text{Tempdrift}_{\text{DAQ}}$, non-equilibrium/non-steady state errors are negligible. Many of the uncertainties The measured quantities ΔT , V_{TE} , and R are have the same uncertainty for both chapter 2 and 3.

$$\text{-----}\Delta T\text{-----}$$

$$\frac{\delta\Delta T}{\Delta T} = \sqrt{\left(\frac{\delta\Delta T_{\text{Noise,system}}}{\Delta T}\right)^2 + \left(\frac{\delta\Delta T_{\text{gain}}}{\Delta T}\right)^2 + \left(\frac{\delta\Delta T_{\text{TCwire}}}{\Delta T}\right)^2 + \left(\frac{\delta\Delta T_{\text{TCconstruction}}}{\Delta T}\right)^2}$$

$$\frac{\delta\Delta T_{\text{Noise,system}}}{\Delta T} \quad \text{two times the measured standard deviation from 3 data points}$$

$$\frac{\delta\Delta T_{\text{gain}}}{\Delta T} = 0.003\sqrt{2} \quad \text{from gain error of DAQ for 2 channels}$$

$$\frac{\delta\Delta T_{\text{TCwire}}}{\Delta T} = .9/300 \quad \text{from the manufactured type-K thermocouple}$$

$$\frac{\delta\Delta T_{\text{TCconstruction}}}{\Delta T} \quad \text{this accounts for systematic error in the thermocouple attachment method. We}$$

used a value of zero but left this term in the equation as a reminder.

$$\text{-----}V_{\text{TE}}\text{-----}$$

$$\frac{\delta V_{\text{TE}}}{\Delta V_{\text{TE}}} = \sqrt{\left(\frac{\delta V_{\text{gain}}}{V_{\text{TE}}}\right)^2 + \left(2 \frac{\delta V_{\text{TE,Noise,system}}}{V_{\text{TE}}}\right)^2 + \left(\frac{V_{\text{alumel}}}{V_{\text{TE}}} \frac{\delta V_{\text{TCwire}}}{V_{\text{alumel}}}\right)^2}$$

$$\frac{V_{\text{alumel}}}{V_{\text{TE}}} \frac{\delta V_{\text{TCwire}}}{V_{\text{alumel}}} = 0.1 \frac{\delta\Delta T_{\text{TCwire}}}{\Delta T} = .1 * .9 / 300 = .00037 \quad \text{the uncertainty in the alumel compensation is}$$

negligible

$$\frac{\delta V_{TE, Noise, system}}{V_{TE}} = \text{two times the measured standard deviation from 3 data points}$$

$$\frac{\delta V_{gain}}{V_{TE}} = .003 \text{ gain error from the DAQ}$$

-----R-----

$$\frac{\delta R}{\Delta R} = \sqrt{\left(\frac{\delta R_{Noise, system}}{R}\right)^2 + \left(\frac{\delta V_{gain}}{V_{TE}}\right)^2}$$

$$\frac{\delta R_{Noise, system}}{R} = \text{two times the measured standard deviation from 3 data points}$$

-----Q_{Hot}-----

The hot side heat transfer is given by

$$Q_{Hot} = IV - \sum Q_{Loss}$$

There the uncertainty is written as

$$\frac{\delta Q_{Hot}}{Q_{Hot}} = \frac{\sqrt{\delta IV^2 - \sum \delta Q_{loss}^2}}{Q_{Hot}}$$

The absolute uncertainty in the total dissipated power is given by

$$\delta IV = IV \sqrt{\left(\frac{\delta I_{Heater}}{I_{Heater}}\right)^2 + \left(\frac{\delta V_{Heater}}{V_{Heater}}\right)^2 + \left(\frac{\delta IV_{Noise}}{IV}\right)^2}$$

$$\frac{\delta I_{Heater}}{I_{Heater}} = .001 \text{ from uncertainty in precision resistor (checked with Keithley current source)}$$

$$\frac{\delta V_{Heater}}{V_{Heater}} \text{ this value is from the Keithley and is negligible}$$

$$\frac{\delta IV_{Noise}}{IV} \text{ two times the measured standard deviation from 3 data points}$$

-----Chapter 2-----

The absolute uncertainty in the losses from chapter two are given by

$$\frac{\delta R_{Pt,wire}}{R_{Heater}} = \frac{.25}{200}$$

$$\frac{\delta Q_{Radiation}}{Q_{Loss}} = \frac{Q_{Radiation}}{Q_{Loss}} \frac{\delta A_{solder}}{A_{Heater}} = \frac{Q_{Radiation}}{Q_{Loss}} \cdot 1/6 \cdot 1/2 \approx 0.04-.05$$

this error develops from the change in area of the heater before and after soldering to the legs. This is the dominant contributor to uncertainty in Q_{Hot}

$$\frac{\delta Q_{loss,model fit}}{Q_{Loss}} = 0.055(T_H - T_\infty)^{-1.2} + 0.003$$

-----Chapter 4-----

The largest absolute uncertainty of the losses in chapter three are from the emissivity of the electrodes (Table 5). The second largest source of uncertainty is from the excess Ag epoxy that spreads around the heater. The Ag epoxy is modeled as having an emissivity of 0.8 and covers 1/12 the heater surface. Therefore the heater surface losses have an upper emissivity of +0.05 which adds about 20% upper uncertainty to the heater losses. Finally there is a small contribution from the platinum heater electrodes.

$$\frac{\delta Q_{loss,Pt}}{Q_{loss,Pt}} = .15$$

-----Geometry-----

The geometry uncertainty of rectangular legs is in general given as

$$\frac{\delta Geometry}{Geometry} = \sqrt{\frac{\delta W^2}{W} + \frac{\delta L^2}{L} + \frac{\delta H^2}{H}}$$

In Chapter two the leg geometry is 2 mm plus/minus .004 mm on each side therefore the total geometry uncertainty is

$$\frac{\delta Geometry}{Geometry_{Ch.2}} = .0035$$

The geometry of the legs in Chapter three were roughly trapezoidal in cross section, which produced a much larger uncertainty of

$$\frac{\delta Geometry}{Geometry_{Ch.3}} = .062$$

$$\frac{\delta S_{eff}}{S_{eff}} = \sqrt{\left(\frac{\delta V_{TE}}{V_{TE}}\right)^2 + \left(\frac{\delta \Delta T}{\Delta T}\right)^2}$$

$$\frac{\delta \rho_{eff}}{\rho_{eff}} = \sqrt{\left(\frac{\delta R}{R}\right)^2 + \left(\frac{\delta Geometry}{Geometry}\right)^2}$$

$$\frac{\delta k_{eff}}{k_{eff}} = \sqrt{\left(\frac{\delta Q_{Hot}}{Q_{Hot}}\right)^2 + \left(\frac{\delta \Delta T}{\Delta T}\right)^2 + \left(\frac{\delta Geometry}{Geometry}\right)^2}$$

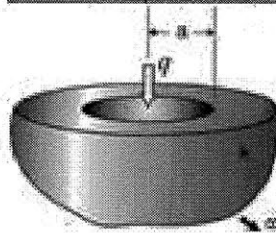
It should be noted that in Chapter 4 the effective thermal conductivity includes sidewall radiation from the leg therefore we don't have to add an uncertainty term from this radiation.

C: Thermocouple Wire Heat Loss

One concern with the thermocouple attachment was whether we would be reading the correct substrate temperature or not. We performed a back of the envelope calculation and modeled the wire attached to the substrate as a circle with a constant heat flux into a semi-infinite body (figure c 1). The estimated conduction loss from a 2 mil type K thermocouple at 600°C is 0.01 W. The thermocouple would be attached by *sintered* silver epoxy with an unknown thermal conductivity, expected to be somewhere between room temperature silver epoxy at $k=0.55$ producing $\Delta T=133^\circ\text{C}$ and pure silver with $k=400$ and $\Delta T=0.1^\circ\text{C}$. The tests performed in Chapter 4 confirmed that attachment method is robust and ΔT is negligible.

$T_{hot}=600\text{C}$, 2mil type K TC wire. $Q_{wire}=0.01$ [W]

k substrate	Material	DeltaT
0.55	Ag epoxy	132.7
3	TE / Alumina	24.33
60	Co812 electrode	1.48
400	Silver/copper	0.132



$$R_{spread} = \frac{\Psi}{\sqrt{\pi k a}}$$

$$\Psi = 465$$

Figure C 1: The thermocouple connection was modeled as heat spreading in a semi-infinite body. The calculated delta T is given for different substrates.

The second concern was the chemical stability of the 2 mil, type K thermocouple wire at high temperature in vacuum. If we extrapolate the recommended temperature for bare, 2 mil, type K wire we get a value of 550°C (figure c 2). Fortunately, the test results in Chapter 4 show no signs of temperature drift or voltage drift on the time scales used in the measurement. Thus all concerns of the thermocouple attachment were answered and the accuracy of the method was verified.

Thermocouple Stability

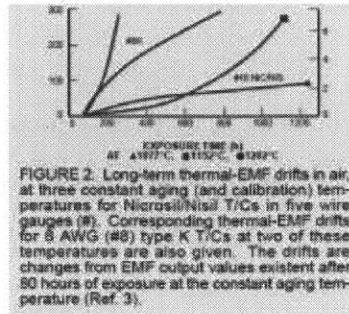
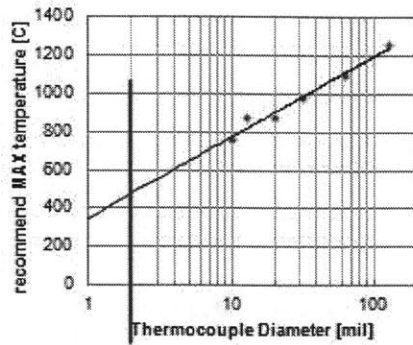


FIGURE 2: Long-term thermal-EMF drifts in air, at three constant aging (and calibration) temperatures for Microsil/Nisil T/Cs in five wire gauges (#6). Corresponding thermal-EMF drifts for 8 AWG (#6) type K T/Cs at two of these temperatures are also given. The drifts are changes from EMF output values existent after 80 hours of exposure at the constant aging temperature (Ref. 3).

2 mil (50um) wire is used

Thermocouple Type	Temperature Range		Tolerances-Reference Junction 0°C (32°F)			
	°C	°F	Standard Tolerances		Special Tolerances	
			°C (whichever is greater)	°F	°C (whichever is greater)	°F
T	0 to 370	32 to 700	±1 or ±0.75 %	Note 2	±0.5 or 0.4 %	Note 2
J	0 to 760	32 to 1400	±2.2 or ±0.75 %		±1.1 or 0.4 %	
E	0 to 970	32 to 1600	±1.3 or ±0.5 %		±1 or ±0.4 %	
K or N	0 to 1200	32 to 2300	±2.2 or ±0.75 %		±1.1 or ±0.4 %	

Type K recommended "limited use in vacuum"

Figure C 2: Type K thermocouple wire limitations. (top left) recommended maximum operating temperature versus thermocouple diameter, extrapolated to the 2 mil diameter. (top right) Long term EMF drifts in air for of 8 AWG thermocouple wire exposed to temperatures above 1000°C. (bottom) Nominal uncertainty of thermocouple wire of different types.⁷⁹

D: Contact Resistance

The electrical contact resistance was measured on a homemade moving probe system. The sample was loaded in a miniature vice, and wetted with In-Ga eutectic (liquid metal) to make good electrical contact (figure d 1). Current was injected on each end of the sample and a 4-wire measurement was made. One sense probe was located near the flat Cu electrode on the miniature vice. The second probe was made from a sharpened*, spring-loaded probe attached to a moveable 2-D optical stage. The tip diameter of the probe was $\sim 25\ \mu\text{m}$, and stage could be moved in increments as small as $1\ \mu\text{m}$, the measurements were repeatable in increments of $2\ \mu\text{m}$. The procedure was to gently contact the surface of the sample—being careful not to use so much force that the tip deforms—and then make the measurement, then back out the tip and move to another position. Note that the tip was not *dragged* across the surface. The electrical resistance was measured with the same instrumentation and Labview software as used in Chapter 2 and Chapter 4.

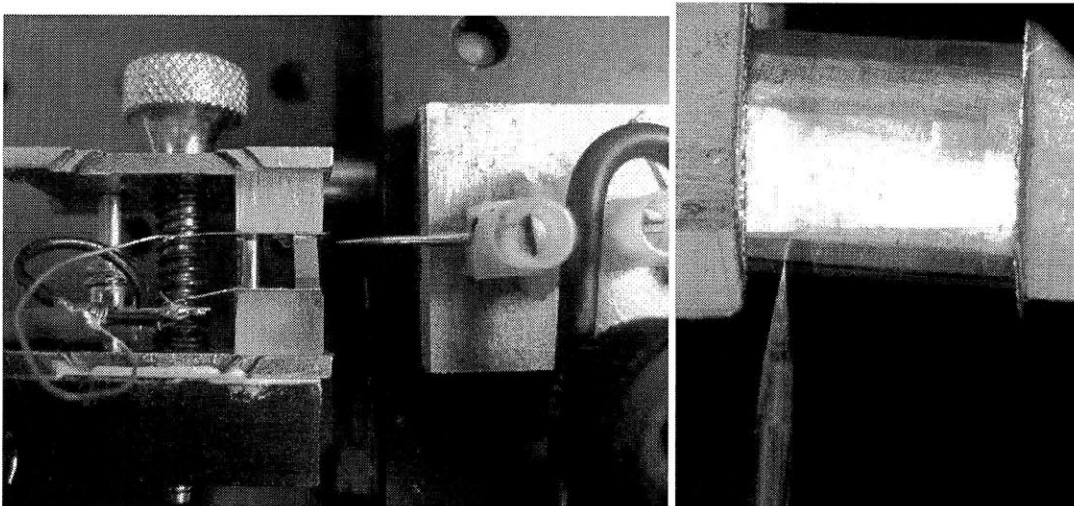
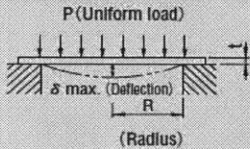


Figure D 1: Electrical resistance versus length measurement assembly. (left) Sample holder and and sharpened, spring-loaded probe a moveable 2-D optical stage. (right) Zoomed up view of a sample under test.

* The probe was sharpened by hand with progressively finer sandpaper.

E: Mechanical Loading on Electrode During Press

The electrode would often crack from bending stress due to uneven loading during press. Below are simple equations to calculate the maximum bending stress in the disk.

Load bending moment diagram	Maximum stress, Maximum deflection
<p>1. Disk receiving uniform load and having supported the perimeter</p> 	<p>The circumferential stress σ_t and radial σ_r can be expressed as follows at the center.</p> $(\sigma_t)_{\max.} = (\sigma_r)_{\max.} = \pm \frac{3P(3m+1)R^2}{8mt^2}$ <p>Also, the central deflection $\delta_{\max.}$ can be expressed as follows :</p> $\delta_{\max.} = \frac{3(m-1)(5m+1)}{16Em^2 t^3} PR^4$ <p>Wherein, P...Load, R...Radius of plate, t...Plate thickness, E...Young's modulus, $\frac{1}{m}$...Poisson's ratio</p>

The resulting maximum stress on the original 1/2" diameter sample with an electrode thickness of 2 mm is 860 MPa. This is obviously an enormous stress which indicates that the load must be applied as uniformly as possible to distribute the load. Since the maximum stress scales with $\frac{R^2}{t^2}$ then scaling down the diameter from 1/2" to 1/4" means that the thickness can be reduced from 2 mm to 1 mm and still withstand the same pressure.

Bibliography

1. Hendricks, T. *Engineering Scoping Study of Thermoelectric Generator Systems for Industrial Waste Heat Recovery*. (US Department of Energy: 2006).at
<http://www1.eere.energy.gov/industry/imf/pdfs/teg_final_report_13.pdf>
2. Rowe, D.M. *Thermoelectric Handbook Macro to Nano*. (CRC Press: Boca Raton, 2006).
3. Hicks, L.D. & Dresselhaus, M.S. Effect of quantum-well structures on the thermoelectric figure of merit. *Phys. Rev. B* 47, 12727 (1993).
4. Goldsmid, H.J. *Electronic Refrigeration*. (Pion Limited: London, 1986).
5. Ashcroft & Mermin *Solid State Physics*. (Thompson Learning Inc.: 1976).
6. Onsager, L. Reciprocal Relations in Irreversible Processes. I. *Phys. Rev.* 37, 405 (1931).
7. Chen, G. & (PhD.), G.C. *Nanoscale energy transport and conversion: a parallel treatment of electrons, molecules, phonons, and photons*. (Oxford University Press US: 2005).
8. Muto, A. (Andrew J. Device testing and characterization of thermoelectric nanocomposites. at
<<http://dspace.mit.edu/handle/1721.1/44915>>
9. Rowe, D.M. *Thermoelectrics*. (CRC Press: Boca Ranton, 1995).
10. Rowe, D.M. *Thermoelectric Handbook Macro to Nano*. (CRC Press: Boca Raton, 2006).
11. Vining, C. The Limited Role for Thermoelectrics in the Climate Crisis. (2008).
12. Vining, C.B. An inconvenient truth about thermoelectrics. *Nat Mater* 8, 83-85 (2009).
13. Poudel, B. et al. High-thermoelectric performance of nanostructured bismuth antimony telluride bulk alloys. *Science* 320, 634-638 (2008).
14. Minnich, A.J. et al. Modeling study of thermoelectric SiGe nanocomposites. *Phys. Rev. B* 80, 155327 (2009).
15. Wang, X.W. et al. Enhanced thermoelectric figure of merit in nanostructured n-type silicon germanium bulk alloy. *Applied Physics Letters* 93, 3 (2008).
16. Dresselhaus, M.S. et al. New Directions for Low-Dimensional Thermoelectric Materials. *Advanced Materials* 19, 1043-1053 (2007).
17. Yang, J. Thermoelectric Properties of CoSb₃-Based Skutterudites. (2010).at
<<http://hdl.handle.net/2345/1418>>
18. Parker, W.J., Jenkins, R.J., Butler, C.P. & Abbott, G.L. Flash Method of Determining Thermal Diffusivity, Heat Capacity, and Thermal Conductivity. *Journal of Applied Physics* 32, 1679-1684 (1961).
19. F. Righini & A. Cezairliyan Pulse method of thermal diffusivity measurements. *High Temp. High Press.* 5, 481 (1973).
20. Cezairliyan, A., Maglic, K.D. & Peletsky, V.E. *Compendium of Thermophysical Property Measurement Methods*. (Springer: 1992).
21. Yang, J. & Caillat, T. Thermoelectric Materials for Space and Automotive Power Generation. *MRS Bulletin* 31, 224-229 (2006).
22. Ravi, V. et al. Thermal Expansion Studies of Selected High-Temperature Thermoelectric Materials. *Journal of Elec Materi* 38, 1433-1442 (2009).

23. Kambe, M., Jinushi, T. & Ishijima, Z. Encapsulated Thermoelectric Modules and Compliant Pads for Advanced Thermoelectric Systems. *Journal of Elec Materi* 39, 1418-1421 (2010).
24. El-Genk, M.S., Saber, H.H., Caillat, T. & Sakamoto, J. Tests results and performance comparisons of coated and un-coated skutterudite based segmented unicouples. *Energy Conversion and Management* 47, 174-200 (2006).
25. El-Genk, M.S., Saber, H.H. & Caillat, T. Performance Tests of Skutterudites and Segmented Thermoelectric Converters. *AIP Conf. Proc.* 699, 541-552 (2004).
26. Saber, H.H. & El-Genk, M.S. Effects of metallic coatings on the performance of skutterudite-based segmented unicouples. *Energy Conversion and Management* 48, 1383-1400 (2007).
27. Salzgeber, K., Prenninger, P., Grytsiv, A., Rogl, P. & Bauer, E. Skutterudites: Thermoelectric Materials for Automotive Applications? *Journal of Elec Materi* 39, 2074-2078 (2009).
28. Rogl, G. et al. Multifilled nanocrystalline p-type didymium - Skutterudites with $ZT > 1.2$. *Intermetallics* 18, 2435-2444 (2010).
29. Saber, H.H., El-Genk, M.S. & Caillat, T. Performance Test Results of a Skutterudite-Based Unicouple with a Metallic Coating. *AIP Conf. Proc.* 746, 584-592 (2005).
30. Muto, A., Kraemer, D., Hao, Q., Ren, Z.F. & Chen, G. Thermoelectric properties and efficiency measurements under large temperature differences. *Review of Scientific Instruments* 80, 7 (2009).
31. Harman, T.C., Cahn, J.H. & Logan, M.J. Measurement of Thermal Conductivity by Utilization of the Peltier Effect. *Journal of Applied Physics* 30, 1351-1359 (1959).
32. Iwasaki, H., Koyano, M. & Hori, H. Evaluation of the Figure of Merit on Thermoelectric Materials by Harman Method. *Jpn. J. Appl. Phys.* 41, (2002).
33. Satake, A., Tanaka, H., Ohkawa, T., Fujii, T. & Terasaki, I. Thermal conductivity of the thermoelectric layered cobalt oxides measured by the Harman method. *Journal of Applied Physics* 96, 931-933 (2004).
34. Venkatasubramanian, R., Siivola, E., Colpitts, T. & O'Quinn, B. Thin-film thermoelectric devices with high room-temperature figures of merit. *Nature* 413, 597-602 (2001).
35. Iwasaki, H. & Hori, H. Thermoelectric property measurements by the improved Harman method. *Thermoelectrics, 2005. ICT 2005. 24th International Conference on* 513-516 (2005).
36. Pauw, L.J. van der A Method of Measuring Specific Resistivity and Hall Effect of Discs of Arbitrary Shapes. *Philips Res. Repts.* 13, 1-9 (1958).
37. Cape, J.A. & Lehman, G.W. Temperature and Finite Pulse-Time Effects in the Flash Method for Measuring Thermal Diffusivity. *Journal of Applied Physics* 34, 1909-1913 (1963).
38. Gao, M. & Rowe, D.M. A novel principle allowing rapid and accurate measurement of a dimensionless thermoelectric figure of merit. *Measurement Science and Technology* 1261 (2001).
39. Sherman, B., Heikes, R.R. & R. W. Ure, J. Calculation of Efficiency of Thermoelectric Devices. *Journal of Applied Physics* 31, 1-16 (1960).
40. Caillat, T. et al. Development of a high efficiency thermoelectric unicouple for power generation applications. *Thermoelectrics, 1999. Eighteenth International Conference on* 473-476 (1999).at <http://ieeexplore.ieee.org/xpls/abs_all.jsp?arnumber=843433>
41. Caillat, T., Fleurial, J.P., Snyder, G.J. & Borshchevsky, A. Development of high efficiency segmented thermoelectric unicouples. *Thermoelectrics, 2001. Proceedings ICT 2001. XX International Conference on* 282-285 (2001).
42. Diller, R.W. & Bell, L.E. Experimental results confirming improved efficiency of thermoelectric power generation systems with alternate thermodynamic cycles. *Thermoelectrics, 2003 Twenty-Second International Conference on - ICT* 571-573 (2003).
43. Mayer, P.M. High-density thermoelectric power generation and nanoscale thermal metrology. (2007).

44. Gao, M., Rowe, D.M. & Kontostavakis, K. Thermoelectric figure-of-merit under large temperature differences. *Journal of Physics D: Applied Physics* 1301 (2004).
45. Fabrication and evaluation of CoSb₃/electrode thermoelectric joints. at <<http://cat.inist.fr/?aModele=afficheN&cpsid=22608861>>
46. Zhao, D., Li, X., He, L., Jiang, W. & Chen, L. Interfacial evolution behavior and reliability evaluation of CoSb₃/Ti/Mo-Cu thermoelectric joints during accelerated thermal aging. *Journal of Alloys and Compounds* 477, 425-431 (2009).
47. Fan, J., Chen, L., Bai, S. & Shi, X. Joining of Mo to CoSb₃ by spark plasma sintering by inserting a Ti interlayer. *Materials Letters* 58, 3876-3878 (2004).
48. Ei-Genk, M.S., Saber, H.H., Sakamoto, J. & Caillat, T. Life tests of a skutterudites thermoelectric unicouple (MAR-03). *Thermoelectrics, 2003 Twenty-Second International Conference on - ICT* 417- 420 (2003).doi:10.1109/ICT.2003.1287537
49. Ravi, V. et al. Mechanical Properties of Thermoelectric Skutterudites. *AIP Conference Proceedings* 656-662 (2008).doi:10.1063/1.2845027
50. Salzgeber, K., Prenninger, P., Grytsiv, A., Rogl, P. & Bauer, E. Skutterudites: Thermoelectric Materials for Automotive Applications? *Journal of Elec Materi* 39, 2074-2078 (2009).
51. Hattori, T., Iwadate, Y., Tatsumoto, H. & Mochizuki, T. Thermal characteristics and pressure sintering of Co₂Si. *J Mater Sci Lett* 7, 481-483 (1988).
52. Yaws, C.L. *Thermophysical Properties of Chemicals and Hydrocarbons*. (William Andrew: 2008).
53. Westbrook, J.H. & Fleischer, R.L. *Intermetallic Compounds, Volume 3 - Structural Applications of Intermetallic Compounds*.
54. Recknagel, C. et al. Application of spark plasma sintering to the fabrication of binary and ternary skutterudites. *Sci. Technol. Adv. Mater.* 8, 357-363 (2007).
55. Alboni, P.N. et al. Synthesis and Thermoelectric Properties of "Nano-Engineered" CoSb₃ Skutterudite Materials. *Journal of Elec Materi* 36, 711-715 (2007).
56. Liu, L.-S., Zhai, P.-C., Wen, P.-F., Zhang, Q.-J. & Ruan, Z.-W. Low-Cycle Fatigue Properties of CoSb₃-Based Skutterudite Compounds. *Journal of Electronic Materials* 39, 2029-2033
57. Salvador, J.R. et al. Transport and mechanical properties of Yb-filled skutterudites. *Philosophical Magazine* 89, 1517 (2009).
58. Rogl, G. et al. Thermal expansion of skutterudites. *J. Appl. Phys.* 107, 043507 (2010).
59. TPMD Demo: CINDAS, LLC - Materials Properties Data on the Web. at <<https://cindasdata.com/Applications/TPMDDEMO/splashScreen>>
60. Hanninger, G., Ipser, H., Terzieff, P. & L. Komarek, K. The Co-Sb phase diagram and some properties OF NiAs-type Co_{1 ± x}Sb. *Journal of the Less Common Metals* 166, 103-114 (1990).
61. Zhang, J. Numerical simulation of thermoelectric phenomena in field activated sintering. (2005).at <<http://hdl.handle.net/1860/407>>
62. Conrad, H. Thermally activated plastic flow of metals and ceramics with an electric field or current. *Materials Science and Engineering A* 322, 100-107 (2002).
63. Langer, J., Hoffmann, M.J. & Guillon, O. Direct comparison between hot pressing and electric field-assisted sintering of submicron alumina. *Acta Materialia* 57, 5454-5465 (2009).
64. M. Tokita Mechanism of Spark Plasma Sintering. at <<http://xa.yimg.com/kq/groups/3862917/2054596553/name/SUMITOMO+REVIEW-Spark-Plasma-Sintering.pdf>>
65. Roberts, R.B., Righini, F. & Compton, R.C. Absolute scale of thermoelectricity III - PB - Taylor & Francis. *Philosophical Magazine Part B* 52, 1147 (1985).
66. Cusack, N. & Kendall, P. The Absolute Scale of Thermoelectric Power at High Temperature. *Proc. Phys. Soc.* 72, 898-901 (1958).

67. Xiaoya Li, Lidong Chen, Junfeng Fan & Shengqiang Bai Mo/Ti/CoSb₃ joining technology for CoSb₃ based materials. *24th International Conference on Thermoelectrics, 2005. ICT 2005* 540- 542 (2005).doi:10.1109/ICT.2005.1520002
68. Hara, R., Inoue, S., Kaibe, H.T. & Sano, S. Aging effects of large-size n-type CoSb₃ prepared by spark plasma sintering. *Journal of Alloys and Compounds* 349, 297-301 (2003).
69. Price, H. et al. Advances in Parabolic Trough Solar Power Technology. *J. Sol. Energy Eng.* 124, 109-125 (2002).
70. Kreith, F. & Goswami, D.Y. *Handbook of Energy Efficiency and Renewable Energy*. (CRC Press: 2007).
71. Kaltschmitt, M., Streicher, W. & Wiese, A. *Renewable Energy: Technology, Economics and Environment*. (Springer: 2007).
72. Price, H. *Assessment of Parabolic Trough and Power Tower Solar Technology Cost and Performance Forecasts*. (NREL: 2003).at <<http://www.nrel.gov/docs/fy04osti/34440.pdf>>
73. O'Gallagher, J.J. *Nonimaging Optics in Solar Energy*. (Morgan and Claypool Publishers: 2008).
74. Thomas, A. & Guven, H.M. Effect of optical errors on flux distribution around the absorber tube of a parabolic trough concentrator. *Energy Conversion and Management* 35, 575-582 (1994).
75. Next Generation Receivers. (2007).at <http://www.nrel.gov/csp/troughnet/pdfs/2007/benz_next_generation_receivers.pdf>
76. Zhang, Q.-C. Metal-AlN cermet solar selective coatings deposited by direct current magnetron sputtering technology. *J. Phys. D: Appl. Phys.* 31, 355-362 (1998).
77. appl.pdf. at <<http://www.personal.utulsa.edu/~kenneth-weston/appl.pdf>>
78. Hassani, V. & Price, H. MODULAR TROUGH POWER PLANTS. *Proceedings of Solar Forum 2001* (2001).at <<http://www.p2pays.org/ref/46/45445.pdf>>
79. thermocouples and thermocouple probes. at <<http://www.omega.com/thermocouples.html>>